UNIVERSITÀ DEGLI STUDI DI MILANO
Facoltà di Scienze Matematiche, Fisiche e Naturali
Corso di Laurea in Fisica

Setup of a narrow linewidth UV/VIS laser system for high-resolution spectroscopy of cold large molecules

Giorgio Bardizza
Matr. 577440

Promotor:
Prof. P.Milani
Univesrità statale degli studi di Milano,
Dipartimento di Fisica

Co-promotors:
Prof. S.Iannotta
Institute for photonics and
nanotechnologies (IFN) - Trento

Dr. J.Küpper
Fritz-Haber-Institut
der Max-Plank-Gesellschaft - Berlin

Prof. G.Meijer
Fritz-Haber-Institut
der Max-Plank-Gesellschaft - Berlin

Anno Accademico 2003/04

Contents

Introduction **11**

1 Theory **13**
1.1 Interferometer . . . 13
1.1.1 Fabry-Perot interferometer . . . 13
1.1.2 Confocal interferometer . . . 16
1.1.3 Quasi-confocal interferometer . . . 19
1.1.4 Simulation of interference patterns . . . 21
1.2 Iodine absorption spectroscopy . . . 26

2 Experimental Setup **31**
2.1 Lasers and second harmonic generation . . . 31
2.2 Calibration Devices . . . 34
2.2.1 Confocal Fabry-Perot interferometer . . . 34
2.2.2 Quasi-confocal Fabry-Perot interferometer . . . 37
2.2.3 Iodine cell . . . 40

3 Results **43**
3.1 Interferometers . . . 43
3.1.1 Confocal interferometer results . . . 45
3.1.2 Quasi-confocal interferometer results . . . 47
3.2 Iodine absorption spectroscopy . . . 50
3.3 OH molecular beam detection . . . 52
3.3.1 Deceleration of molecular beams . . . 52
3.3.2 Experimental setup and results . . . 54

4 Sintesi in italiano **59**
4.1 Introduzione . . . 59
4.2 Teoria: Interferometria e interferenza . . . 59
4.2.1 Interferometro Fabry-Perot . . . 61
4.2.2 Interferometro Fabry-Perot a specchi concavi . . . 62
4.2.3 Simulazioni delle figure di interferenza . . . 65
4.3 Apparato sperimentale . . . 67
4.3.1 Laser e generatore di seconda armonica . . . 67
4.3.2 Componenti per la calibrazione . . . 67
4.4 Risultati . . . 71
4.5 Conclusioni . . . 74

Conclusion **76**

A Confocal interferometer FSR measurement data **81**

Bibliography **85**

List of Tables

3.1 Mean confocal interferometer FSR values calculated for each single measurement separately in three different ways. 46
3.2 Order of assignment and relative peak-numbers N calculated utilizing integer numbers. 47
3.3 Check of the predicted N values. 48
3.4 Mean FSR values of the quasi-confocal interferometer calculated for each single measurement separately in three different ways. 48

List of Figures

1.1 Superposition of two coherent waves with the same frequency and different phases. . . . 14
1.2 Interference in parallel plate. . . . 15
1.3 Transmitted intensity of an interference pattern from a Fabry-Perot interferometer for different values of the reflectivity of the mirrors. . . . 16
1.4 Plot of the intensity I_{00} of the fundamental mode TEM_{00}. . . . 17
1.5 Beam waist in a resonator along the longitudinal axis. . . . 17
1.6 Front view intensity profiles of the fundamental mode TEM_{00} at several location z in a confocal resonator. . . . 18
1.7 Maximum of the intensity along the z axis for TEM_{00} and TEM_{10}. . . . 18
1.8 Spatial intensity profile for TEM_{00} and TEM_{10}. . . . 19
1.9 Intensity and amplitude profiles for different cavity modes 19
1.10 Geometry of a symmetric nonconfocal cavity. . . . 20
1.11 Simulation of axial and transverse mode frequencies for a near planar, confocal and a near concentric resonator. . . . 23
1.12 Distribution of axial and transverse modes (m,n) 23
1.13 Build up scheme of simulations 24
1.14 Simulation of the eigenfrequencies for different radii of curvature. . . . 25
1.15 Absorption spectrum of iodine 26
1.16 Absorbtion and emission of light of a molecular gas on and off resonance . . 27
1.17 Experimental setup of a Doppler-free absorption spectroscopy. . . . 28

2.1 Schematic of the laser system. . . . 31
2.2 Schematic of the Ring Dye Laser cavity and active frequency controller . . . 32
2.3 Selection of the laser mode through the different optical elements 33
2.4 Second harmonic generation cavity 34
2.5 Explosion drawing of the confocal Fabry-Perot interferometer. . . . 35
2.6 Technical drawing of the assembled confocal Fabry-Perot interferometer. The caps where the mirrors lye are of stainless steel. Two springs are used to push the mirrors against the faces of the tube in order to compensate possible stretches of the caps due to temperature variations. . . . 35
2.7 Peak shifts in the confocal interferometer interference pattern for different values of L/R. . . . 36
2.8 Comparison of the interference pattern for the exact confocal configuration and accounting for experimental construction imperfections. . . . 36
2.9 Picture of the confocal interferometer 37
2.10 Picture of the confocal interferometer inside the plexiglass evacuated cover . 38
2.11 Explosion drawing of the higher order Fabry-Perot interferometer. . . . 38

2.12 Technical drawing of the higher order Fabry-Perot interferometer. 39
2.13 Picture of the quasi-confocal interferometer 39
2.14 Simulation of an interference pattern for an interferometer with approximately 50 MHz FSR 40
2.15 Technical drawing of the iodine cell. 41
2.16 Picture of the quasi-confocal interferometer inside the plexiglass evacuated cover 41
2.17 Picture of the calibration devices 42

3.1 Measured signal traces. 44
3.2 Zoom of measured signal traces. 44
3.3 Plot of the peak-numbers for the markers of iodine lines as a function of the frequency (single measurement). 45
3.4 Plot of the peak-numbers q for the markers of the measured iodine lines reported in Appendix A as a function of the frequency. 49
3.5 Iodine absorption spectrum (lines 1088-1096) 50
3.6 Display of the wavemeter. 51
3.7 Iodine absorption spectrum from the iodine atlas. 51
3.8 Schematic of a supersonic expansion. 52
3.9 The Stark shift of OH ($X^2\Pi_{3/2}, J = 3/2$) radicals. 53
3.10 A polar molecule in an electric field. 54
3.11 Switching of the electric field in a Stark decelerator. 55
3.12 Picture of the machine used to produce and decelerate the OH-radicals . . . 56
3.13 Schematic of the experimental setup in continuous wave time of flight measurements of OH-radicals. 56
3.14 LIF intensity signal for continuous wave time of flight measurements for fast and decelerated OH radicals. 57

4.1 Interferenza in fase e fuori fase di due onde coerenti 60
4.2 Interferenza di riflessioni tra superfici piane parallele. 61
4.3 Figura di interferenza di un interferometro Fabry-Perot 62
4.4 Distribuzione dell'intensità I_{00} del modo fondamentale TEM_{00} nelle direzioni (x,y) perpendicolari a quella di propagazione. 63
4.5 Grafico di w(z) lungo l'asse di propagazione z 64
4.6 Distribuzione spaziale dell'intensità all'interno di una cavità risonante simmetrica confocale per TEM_{00} e TEM_{10}. 64
4.7 Geometria di una cavità simmetrica a specchi concavi non confocale 65
4.8 Simulazione dei picchi d'interfernza per un interferometro simmetrico piano, confocale e concentrico in cui sono considerati i modi trasversali superiori . 66
4.9 Distribuzione dei modi superiori (m,n) in una figura di interferenza 66
4.10 Schema del sistema laser 67
4.11 Schema dell'interferometro Fabry-Perot confocale 68
4.12 Disegno tecnico dell'interferometro Fabry-Perot confocale 69
4.13 Comparazione tra figura di interferenza del caso confocale perfetto (grigio) e caso confocale considerate le tolleranze su L e R 69
4.14 Schema dell'interferometro Fabry-Perot quasi-confocale. 70
4.15 Disegno tecnico dell'interferometro Fabry-Perot quasi-confocale. 70
4.16 Simulazione della figura di interferenza dell'interferomtero quasi-confocale risultante in una FSR di circa 50 MHz 71

4.17 Disegno tecnico della cella iodica 72
4.18 Tracce dei segnali misurati 73
4.19 Ingrandimento di figura 4.18 attorno a due linee spettrali 73

Introduction

Over the last decades there has been vast progress in controlling the motion of particles ranging from ions to atoms and molecules. This control has lead to many important new ideas in atomic and molecular physics, including the realization of Bose-Einstein condensation and atom lasers. The study of ultracold molecules promises further important insight into physics and chemistry. High resolution spectroscopy is a useful tool to investigate the properties of ultracold molecular samples [7].

Important improvements have been made over the last years in decelerating and trapping molecular beams [4], allowing to store molecules in traps [1] or to increase the interaction time with the measuring device [15]. Since the spectral resolution of every measuring device is limited by the time Δt a molecule spends inside, the increase of the interaction time allows for higher resolution measurements.

A common technique for studying molecules in the gas-phase is laser-induced fluorescence (LIF). Molecules are excited by ultraviolet or visible radiation and the emitted fluorescence is detected as a function of excitation frequency. The amount of obtainable information in vibrationally or rotationally resolved spectroscopy depends on the available resolution.

The aim of the work presented here is to setup a high resolution laser spectrometer with a 1 MHz resolution for the detection and spectroscopy of decelerated large molecules. Special emphasis is put on the design and setup of the necessary calibration devices, thought to create a fine scale of equally spaced markers for the frequency determination of cold molecules spectral lines.

Two Fabry-Perot interferometers and a cell containing gaseous iodine are build and characterized. These devices work over the whole operation range of the available laser system (500–700 nm). It is important that the devices have a good long-term and temperature stability. The accurate measurement of the free spectral range for the two interferometers and the calculation of the accuracies are crucial parts of the work. The more precise these values are measured, the more accurate the frequency determination will be.

In the first section of this thesis theoretical descriptions and computational simulations of interference in a Fabry-Perot interferometer are presented. An explanation of iodine absorption spectroscopy for frequency calibration is given in section 1.2. In section 2 the setup of the laser system and the calibration devices are described and in section 3 the obtained results are presented: iodine absorption spectra are measured and the frequency calibration factors of the interferometers are given. The system is applied to obtain first continuous wave (cw) time-of-flight (TOF) measurements of slow OH-radicals, as described in section 3.3.

Chapter 1

Theory

1.1 Interferometer

An instrument designed to exploit the interference of light and the fringe patterns that result from optical path differences is called an *optical interferometer*. These instruments are commonly used with lasers and are standard parts found on optical tables.

The concept they exploit is the interference of coherent lightwaves. Such coherent lightwaves, originating from a single source, make different round-trips in an interferometer. The intensities are summed in an interference pattern. A plane light wave can be written as:

$$E(x,t) = E_0 \sin[\omega t - (kx + \varepsilon)] \qquad \alpha(x,\varepsilon) = -(kx + \varepsilon)$$

$$E(x,t) = E_0 \sin[\omega t + \alpha(x,\varepsilon)]$$

where the dependence of the phase on the optical path x is evident. Considering two waves of frequency ω interfering with each other, their sum results in a *sumwave* of the same frequency ω with an intensity that depends on the relative phase shift they have: it has a maximum if they are exactly in phase, and a minimum (zero if their intensities are the same) if the phases are opposite:

$$E_1 = E_{01} \sin(\omega t + \alpha_1) \qquad E_2 = E_{02} \sin(\omega t + \alpha_2)$$

$$\Longrightarrow E_{tot} = E_1 + E_2 = E_0 \sin(\omega t + \alpha)$$

where:

$$E_0^2 = E_{01}^2 + E_{02}^2 + 2E_{01}E_{02}\cos(\alpha_2 - \alpha_1)$$

$$\tan\alpha = \frac{\left(E_{01}\sin\alpha_1 + E_{02}\sin\alpha_2\right)}{\left(E_{01}\cos\alpha_1 + E_{02}\cos\alpha_2\right)}$$

When $\alpha_1 = \alpha_2$ (waves in-phase) there is a maximum of the interference intensity, and when $\alpha_2 - \alpha_1 = \pi$ (waves out-of-phase) there is a minimum, and so forth with a period of 2π. In the particular case of $E_{01} = E_{02}$ the total intensity is exactly zero when the waves are out-of-phase and $2E_0$ when they are in phase (see Figure 1.1).

1.1.1 Fabry-Perot interferometer

Many interferometers exploit multiple-beam interference (see [7, Chapter 4]). Conceptually these multiple-beam interferometers work analogously to two-beam interferometers.

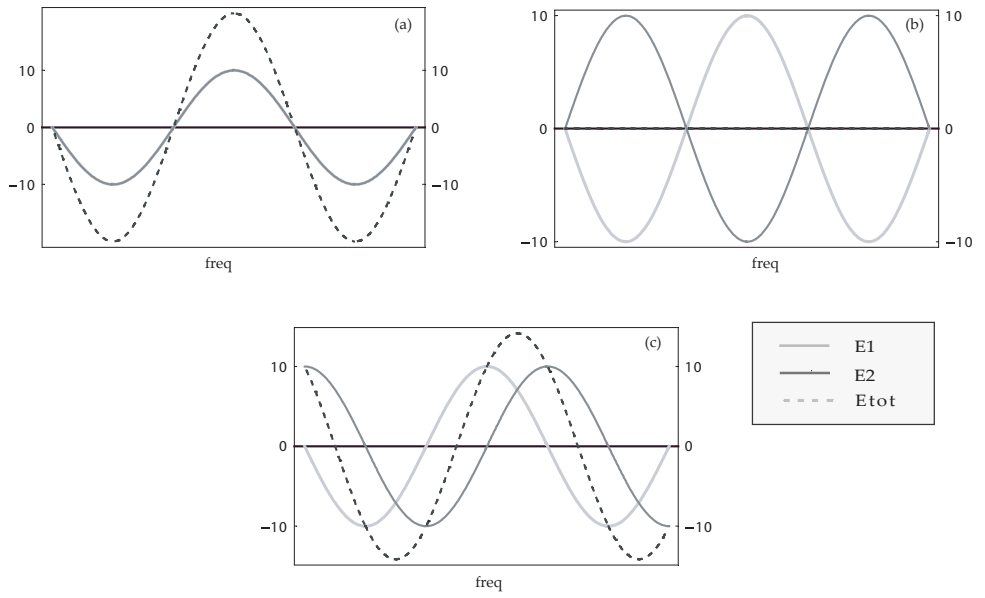

Figure 1.1: Superposition of two coherent waves with the same frequency (a)in-phase, (b)out-of-phase and (c)with a phase-shift of $\frac{\pi}{2}$.

The Fabry-Perot Interferometer is the simplest case of such interferometers. It consists of two plane parallel highly reflecting surfaces. The light-beam performs many round-trips between these surfaces. Every time the beam travels from one surface to the other and back, its phase changes due to the optical path Δs travelled and a phase jump $\Delta\Phi = \pi$ at every surface. The resulting phase difference can be written as:

$$\phi = 2\pi\Delta s/\lambda + \Delta\Phi \tag{1.1}$$

where $\Delta s = 2nd\cos\beta$, n is the refractive index and d the distance between the two surfaces (remember $\sin\alpha = n\sin\beta$, see figure 1.2). If, for instance, the amplitude of the incident wave is A_0, the amplitude after one round trip is

$$A_1 = \sqrt{R_{ef}}A_0\exp(i\pi) = -\sqrt{R_{ef}}A_0$$

where R_{ef} is the reflectivity of the surfaces. The amplitude A of the reflected wave is the sum over all partial amplitudes A_i with their respective phase shifts:

$$\begin{aligned} A &= \sum_{m=1}^{p} A_m\, e^{i(m-1)\phi} = -\sqrt{R_{ef}}\, A_0 + \sqrt{R_{ef}}\, A_0\,(1-R_{ef})\, e^{i\phi} + \sum_{m=3}^{p} A_m\, e^{i(m-1)\phi} = \\ &= -\sqrt{R_{ef}}A_0\left[1-(1-R_{ef})\, e^{i\phi}\sum_{m=0}^{p-2} R_{ef}^{m} e^{im\phi}\right] \end{aligned} \tag{1.2}$$

For vertical incidence ($\alpha = 0$) or infinitely extended surfaces, there is an infinite number of reflections and the geometrical series in (1.2) corresponds to $(1 - R_{ef}e^{i\phi})^{-1}$. In this case the total amplitude A has the simpler form:

$$A = -\sqrt{R_{ef}}\, A_0\,\frac{1-e^{i\phi}}{1-R_{ef}e^{i\phi}} \tag{1.3}$$

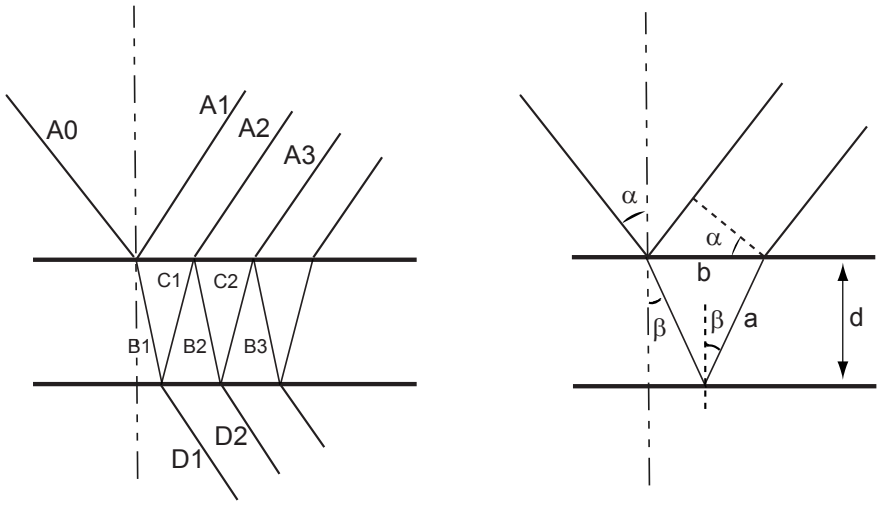

Figure 1.2: Interference in plane parallel plate ($\Delta s = 2na - b\sin\alpha$).

The product of A with its complex conjugate A^* gives the intensity of the reflected wave as a function of the phase shift ϕ:

$$I_{R_{ef}} = I_0 R_{ef} \frac{4\sin^2(\phi/2)}{(1-R_{ef})^2 + 4R_{ef}\sin^2(\phi/2)} \tag{1.4}$$

From the same calculation we can also determine the transmitted intensity as a function of the pase shift:

$$I_T = I_0 \frac{(1-R_{ef})^2}{(1-R_{ef})^2 + 4R_{ef}\sin^2(\phi/2)} \tag{1.5}$$

These two equations (1.4,1.5) are called *Airy formulas* and it is important to verify that $I_{R_{ef}} + I_T = I_0$. A typical interference pattern of a Fabry-Perot Interferometer is shown in figure 1.3 as a function of the frequency ν. The following parameters are used to characterize a FPI:

$$\text{Finesse} \quad \rightarrow \quad F^* := \frac{\pi\sqrt{R_{ef}}}{1-R_{ef}} \tag{1.6}$$

$$\text{Free Spectral Range} \quad \rightarrow \quad FSR = \delta\nu := \frac{c}{\Delta s} \tag{1.7}$$

$$\text{Full Width at Half Maximum} \quad \rightarrow \quad FWHM = \Delta\nu := \delta\nu/F^* \tag{1.8}$$

The FSR is defined as the frequency difference between two successive maxima and the $FWHM$ is the width of a single transmission peak. *Finesse* is a measure of the quality of the interferometer and is directly related to the reflectivity R_{ef} of the mirrors.
Using $\Delta s = 2nd\cos\beta$, the free spectral range is:

$$\delta\nu = \frac{c}{\Delta s} = \frac{c}{2nd\cos\beta} = \frac{c}{2nd\sqrt{1-\sin^2\beta}} = \frac{c}{2d\sqrt{n^2-\sin^2\alpha}}$$

and for vertical incidence ($\alpha = 0$) we obtain:

$$|\delta\nu|_{\alpha=0} = \frac{c}{2nd} \tag{1.9}$$

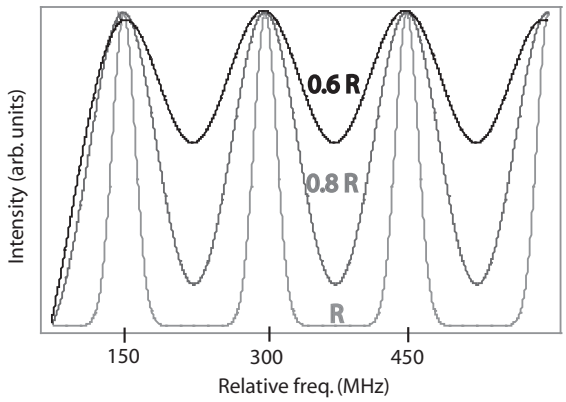

Figure 1.3: Transmitted intensity from a Fabry-Perot interferometer plotted as a function of the frequency ν for different values of the reflectivity R_{ef}: R_{ef}, $0.6R_{ef}$, $0.8R_{ef}$. From the simulation program (FSR=150 MHz and R_{ef}=0.80)

Similarly the phase difference is

$$\phi = 2\pi\Delta s\nu/c = 2\pi\nu/\delta\nu = \frac{4\pi nd}{c}\,\nu$$

using the expression of Δs written before. Fixing the distance between the mirrors (and the index of refraction inside the interferometer) and testing the interferometer with a coherent light source, whose frequency is scanned, the same dependence of the transmitted intensity as a function of the frequency ν is obtained. This is exactly the application of the Fabry-Perot interferometer we exploit in our experiment. It is important to observe that for a real Fabry-Perot interferometer with a plane parallel plate, as described here, the *parallelism* and *alignment* of the plate with the source beam is of fundamental importance, otherwise equation (1.9) is not valid.

1.1.2 Confocal interferometer

A multiple-beam interferometer can also be obtained using concave mirrors instead of plane ones. A particular case of those interferometers with concave mirrors is the confocal Fabry-Perot, where the separation distance between the mirrors d has exactly the same value as the radius of curvature R[1].

The stationary amplitude distribution of a standing wave in a cavity resonator with confocally-spaced concave mirrors of radius R, depending on the coordinate x,y of a plane perpendicular to the z longitudinal axis has the expression (from [7, Chapter 4]):

$$A_{mn}(x,y,z) = C^* H_m(x^*)H_n(y^*)\exp(-r^2/w^2)\exp[-i\phi(z,r,R)] \tag{1.10}$$

where C^* is a normalization factor and H_m is the Hermitian polynomial of m^{th} order. The first exponential is a Gaussian function and the second one a phase factor in which $\phi(z_0,r)$ is the phase in the $z=z_0$ plane at a distance $r=(x^2+y^2)^{1/2}$ from the resonator axis; x^* and y^* depend on the mirror separation d: $x^*=\sqrt{2}x/w$ and $y^*=\sqrt{2}y/w$; w is a measure for the radial amplitude distribution:

$$w^2(z) = \frac{\lambda d}{2\pi}[1+(2z/d)^2] \tag{1.11}$$

[1]not to be confused with the reflectivity R_{ef}

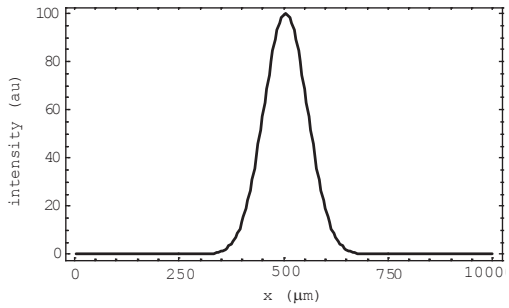

Figure 1.4: Axial/front view: plot of I_{00} with $\lambda = 500\,\text{nm}$, $R = 500\,\text{mm}$ at z=0.

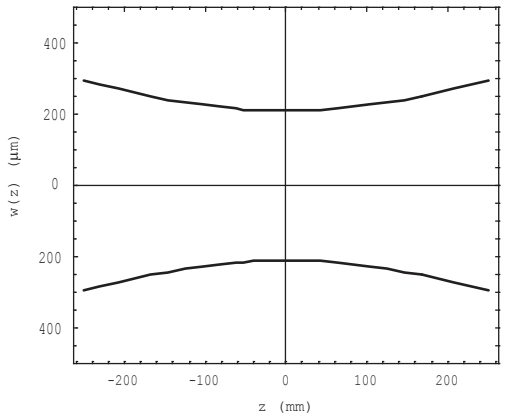

Figure 1.5: Longitudinal/top view: plot of $w(z)$ with $\lambda = 500\,\text{nm}$, $R = 500\,\text{mm}$. The beam waist is $200\,\mu$m and the radius at the mirrors is $300\,\mu$ m.

These two expressions obtained for the special case of a symmetric confocal cavity are very important for a complete description of the electromagnetic field variations inside the cavity perpendicular to the direction of travel of the wave, also called *transverse electromagnetic modes (TEM)*. Plotting them we get the intensity profile of the fundamental transverse mode TEM_{00}, for example, at different points along the longitudinal axis, analogously for the higher order modes. Multiplying A_{mn} with its complex conjugate A^*_{mn} and integrating this product over an appropriately chosen subspace of $\mathbf{R}^3$, we obtain the intensity profile of the corresponding TEM_{mn}. In the first simple case of the fundamental mode TEM_{00} (zero-order transverse mode), (1.10) gives:

$$I_{00}(x, y, z) \propto A_{00}A^*_{00} = I_0 e^{-\frac{2(x^2+y^2)}{w^2}} \tag{1.12}$$

We can look at this formula in three interesting ways:

- **axial/front view**: fixing z, i.e. $z = 0$ in figure 1.4, w is fixed and plotting in function of x or y the gaussian profile along the two directions is distinguishable. The maximum I_0 is reached at $x = 0$ (or $y = 0$). The value of r where the intensity is reduced of $1/e^2$ its maximum value I_0, is defined as *radius of the beam* (see figure 1.4).

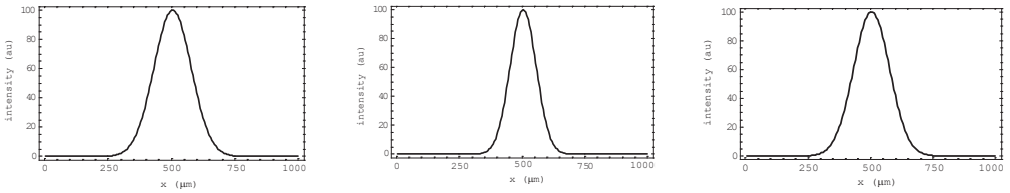

Figure 1.6: Front view profile at several location z in a confocal resonator: (a) and (c) at the mirrors;(b) in the middle ($z = 0$).

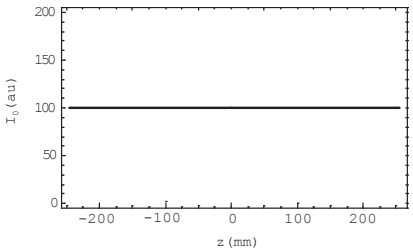

Figure 1.7: Maximum I_0 of the intensity I_{00} along z axis for TEM_{00} and TEM_{10}.

- **longitudinal/top view**: the radius, as defined above, changes with the position along the longitudinal axis. It depends on z according to equation (1.11) and it has a minimum located at the center of the confocal cavity ($z = 0$). Its value is defined as the *beam waist*:

$$w_0 = (\lambda R/2\pi)^{1/2} \tag{1.13}$$

  At the mirrors the radius is the largest within the cavity. Expressed in terms of the beam waist:

$$w(d/2) = \sqrt{2}w_0 \tag{1.14}$$

  In figure 1.5 w is plotted as a function of z.

- **longitudinal/side view**: finally we want to look at the front intensity shape at different positions in the cavity. As shown in figure 1.7 the maximum value of the intensity I_0 in the center $x = y = 0$ is constant along the z-axis, but it is more concentrated around that point in $z = 0$ than in $z = L$ or $z = -L$ where it has the same value (figure 1.6).

We can plot equation (1.12) in a three dimensional graph, showing the intensity profile inside the two mirror cavity, see figure 1.8 for plots of TEM_{00} and TEM_{10}.

These calculations allow one to choose the aperture diameter for the construction of an interferometer. As shown by Siegman [13, chapter 17] for a spot size of w, an aperture with diameter $d = 2w$ transmits approximately 86% and one of diameter $d = \pi w$ about 99%. In order to prevent a diffraction ripple effect an aperture of diameter $d \approx 4.6w$ has to be used. In practice, also considering higher order modes, it is convenient to use an aperture of 4.6 times the spot size for all modes up to $m + n = 3$. An idea of how the spot size changes for modes higher than the fundamental is given in the simulations reported in figure 1.9. Using these calculations I predicted a spot diameter of about 600 μm for the fundamental mode, 800 μm for TEM_{10} and 1000 μm for TEM_{20}. Taking the third one in consideration, the diameter of the FPI cavity mirrors has to be at least about 5 mm.

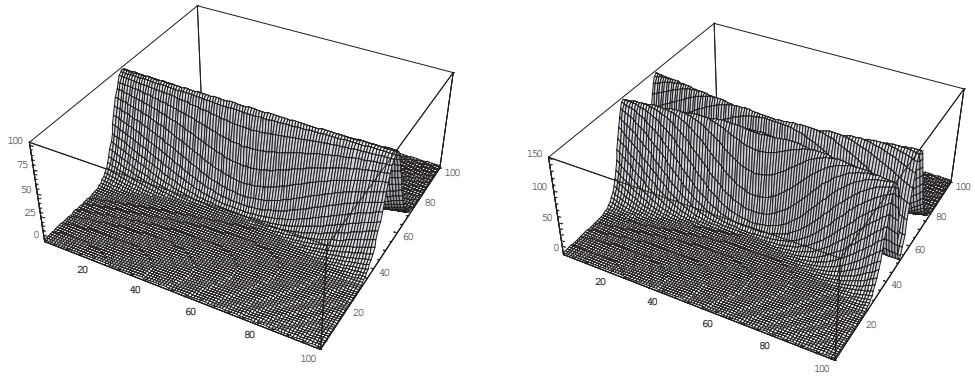

Figure 1.8: Intensity profile for TEM_{00} and TEM_{10}.

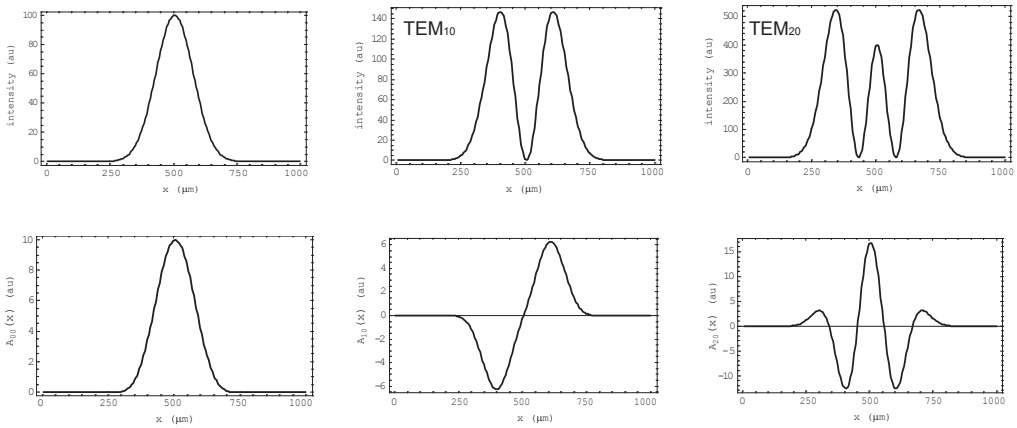

Figure 1.9: Intensity and amplitude profiles for different cavity modes; the x-axis' scale is in 10 μm. The predicted spot diameter is of about 600 μm for TEM_{00}, 800 μm for TEM_{10} and 1000 μm for TEM_{20}

1.1.3 Quasi-confocal interferometer

A still more general description is the quasi Fabry-Perot interferometer, where the cavity is symmetric but not confocal. Hence the radius of curvature of the two mirrors is the same ($R1 = R2 = R$), but the distance d in between is slightly different from that radius. The vertexes of both mirror lie along the axis of the system (see figures 1.10). It is possible to follow a single ray injected into the cavity, via a ray tracing calculation, for all of its subsequent reflections and to determine the position of the point at which the ray intercepts each mirror, the new direction of the ray after each reflection and the path travelled between every two reflections [9].

Figure 1.10 shows the plane containing the incident ray, where C_1 and C_2 are the centers of curvature of the two mirrors M_1, M_2; S_j are unit vectors defined by the single coordinate θ_j and they give the direction of the beam once arrived at a point (A, B, ...) placed on one mirror located by the single coordinate φ_j. ρ_j is the distance the beam travels, going from the point located at φ_j to that located at φ_{j+1}. The goal is to determine θ_p and φ_p in terms of d, R and the initial values θ_0 and φ_0.

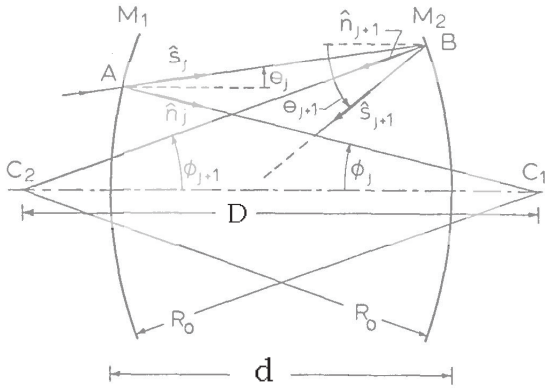

Figure 1.10: Geometry of a symmetric nonconfocal cavity (from reference[9])

From simple geometrical arguments and with the approximation $\tan\alpha \approx \alpha$ for small angles α, we obtain (1.15) and (1.16):

$$\varphi_{j+1} = \varphi_j \; + \; \theta_j \, (d/R) \tag{1.15}$$

$$\theta_{j+1} = \theta_j - \; 2\,\varphi_{j+1} \tag{1.16}$$

Solving (1.16) for θ_j and θ_{j+1} and substituting in (1.15), we have (1.17):

$$\theta_j = \frac{R}{d}(\varphi_{j+1} - \varphi_j) \qquad \theta_{j+1} = \frac{R}{d}(\varphi_{j+2} - \varphi_{j+1})$$

and

$$\varphi_{j+2} \; + \; 2\,u\,\varphi_{j+1} + \varphi_j \; = \; 0 \tag{1.17}$$

where $u = (d - R)/r$. [2]. If now $u = -\cos\psi$, solutions of (1.17) are of the form (1.18):

$$\varphi_p = [\,\varphi_0 + (1+u)\,\theta_0\,]\,\frac{\sin p\,\psi}{\sin\psi} - \; \varphi_0\,\frac{\sin(p-1)\,\psi}{\sin\psi} \tag{1.18}$$

$$\theta_p = -[\,(1+2u)\theta_0 + 2\varphi_0\,]\,\frac{\sin p\,\psi}{\sin\psi} - \; \theta_0\,\frac{\sin(p-1)\,\psi}{\sin\psi} \tag{1.19}$$

where φ_0 and θ_0 are the initial values of φ_j and θ_j. (1.18) and (1.19) are solutions of (1.17) only for $|u| < 1$, corresponding to:

$$0 < d < 2r$$

The expressions of φ_p and θ_p for the confocal case ($u = 0$ or $\psi = \pi/2$) are:

$$\varphi_p = (\,\varphi_0 + \theta_0\,)\sin(p\,\pi/2) - \varphi_0 \sin[\,(p-1)\pi/2\,] \tag{1.20}$$

$$\theta_p = -(\,\theta_0 + 2\varphi_0\,)\sin(p\,\pi/2) - \theta_0 \sin[\,(p-1)\pi/2\,] \tag{1.21}$$

where from the periodicity of those functions follows that:

$$\varphi_{p+4} = \varphi_p$$

[2] See [12, pages 194-197] for more details.

$$\theta_{p+4} = \theta_p$$

The trajectory closes itself and is repeated after four round-trip.

Similarly one obtains the expression for the four-transit path length L as a function of φ_p and θ_p [9]:

$$L = R\sum_{p=0}^{3}[1 + u - {\varphi_p}^2 - u(1+u){\theta_p}^2/2 - (1+u)\theta_p\,\varphi_p] \tag{1.22}$$

Substituting φ_p and θ_p by equations (1.18) and (1.19), the four-transit path length in terms of the initial values φ_0, θ_0 is

$$L = 4r + (4 + 2{\theta_0}^2 + 4\theta_0\,\varphi_0)(d - R) \tag{1.23}$$

This second important result shows that only in the precise confocal case, when $d = R$, the path L of the beam in the cavity is the same for different incidence angles φ_0 and θ_0. Thus it is obvious why the confocal FPI is so commonly used instead of the plane one: it is much easier to align.

As this configuration is interesting for our experiment some calculations have been carried out in order to understand what to expect when d is not exactly equal to R. From these calculations the accuracy needed for the construction of this cavity can be estimated (see section [2.2.1]).

1.1.4 Simulation of interference patterns

To simulate the interference pattern a Mathematica program was written, see appendix **??**. A typical Fabry-Perot interferometer interference pattern, as shown in figure 1.3, consists of peaks of transmitted light separated by the *free spectral range (FSR)* and with a *full width at half maximum (FWHM)* as defined in (1.8). The distance of two peaks depends on the optical path of the beam inside the cavity, the larger is the distance of the mirrors, the smaller the FSR. If the distance is fixed, the width depends only on the reflectivity of the mirrors: the higher the reflectivity, the narrower the peaks.

The eigenfrequencies of a symmetric resonator can be obtained from the phase function present in the stationary amplitude distribution formula in (1.10). The phase function $\phi(r, z)$ is:

$$\begin{aligned}\phi(r,z) &= \frac{2\pi}{\lambda}\left[\frac{R}{2}(1+\xi) + \frac{x^2+y^2}{R}\frac{\xi}{1+\xi^2}\right] \\ &\quad -(1+m+n)\left[\frac{\pi}{2} - \arctan\left(\frac{1-\xi}{1+\xi}\right)\right]\end{aligned} \tag{1.24}$$

where $\xi = 2z/R$. The exact resonance frequency of a given mode is determined by the resonance condition that the round-trip phase shift $2\Delta\phi$ in the cavity must be an integer multiple of 2π:

$$\Delta\phi = \phi(z = L/2) - \phi(z = -L/2) = q\pi \tag{1.25}$$

Evaluating this equation for the phase function (1.24) in the plane $x = y = 0$ for a symmetric (but not confocal, i.e. $R \neq L$) resonator with mirrors of the same radius $R_1 = R_2 = R$, the eigenfrequencies ν_{qmn} written below are found. It is important to remember a trigonometric transformation of the arctan:

$$\arctan(1/x) = -\arctan(x) + \frac{\pi sgn(x)}{2} \qquad x \neq 0 \tag{1.26}$$

The eigenfrequencies obtained are ($L < R$ or $L > R$) [3]:

$$\nu_{qmn} = \frac{c}{2L}\left\{q + \frac{1}{2}(1+m+n)\left[1 + \frac{4}{\pi}\arctan\left(\frac{L-R}{L+R}\right)\right]\right\} \tag{1.27}$$

where q is the eigenvalue of the axial modes and m, n those of the transverse modes. Two important situations of this formula are:

$$\nu_{qmn} \approx \frac{c}{2L}q \qquad for \quad \frac{L}{R} \to 0 \tag{1.28}$$

$$\nu_{qmn} \approx \frac{c}{2L}\left[q + \frac{1}{2}(1+m+n)\right] \quad for \quad \frac{L}{R} \to 1 \tag{1.29}$$

As expected for $L/R \to 0$ (near planar situation) we find the well known formulas for a plane FPI. In the near planar situation the transverse mode frequencies ν_{qmn} associated with a given axial mode q are all collected in one side of the frequency ν_{q00}. Consider fixing the length L of a plane cavity and decreasing the radius of curvature of the mirrors till the near confocal situation ($L \approx R$) is reached. The higher order transverse frequencies spread out until all even transverse modes are degenerated at the axial mode frequencies $q, q+1, ..$ and the odd modes are all degenerated exactly in between two successive axial modes (figure 1.14). This is the confocal situation described in equation 1.29). Going further in decreasing the radius, we reach the near concentric situation, with all the peaks accumulated in the other side of the axial mode frequencies, as shown in 1.11. It is now for that clear that if in a planar FPI the FSR is $c/2d$ (considering the index of refraction $n = 1$), for a confocal FPI with same d the distance between two axial mode frequencies $q, q+1, ..$ is the same, but the FSR of axial plus transverse mode frequencies is only half of that, i.e. $c/4d$.

In figure 1.11 the simulations for the three limit cases *near planar, confocal and near concentric* are shown. When R is approximately, but not exactly equal to L the peaks are broadened or some side-peaks appear. They will have an asymmetric shape larger in the left side if R is slightly bigger than L and in the right one if R is smaller. It is possible to check in this way if L is bigger or smaller than R by looking at the shape of the peaks. All simulations reported were calculated with Mathematica plotting the expression of the eigenfrequencies in (1.27) and assuming every peak has a gaussian shape of the form:

$$f(x,t,c) = \frac{1}{t\sqrt{2\pi}} \cdot \frac{1}{\exp(-\frac{1}{2}(\frac{x-c}{t})^2)} \tag{1.30}$$

The frequency spacing between peaks inside an individual group is calculated from (1.27):

$$\nu_{q\,m+1\,n} - \nu_{qmn} = \frac{c}{4L}\left[1 + \frac{4}{\pi}\arctan\left(\frac{L-R}{L+R}\right)\right] \tag{1.31}$$

In the simulation it is assumed that the intensity of the transverse mode peaks decreases by one tenth going from one order to the next, such that 10 peaks are considered in every group. Then all the groups are summed up to obtain the plots shown before (see as example figures 1.12 and 1.13).

[3] Equation (1.27) as obtained here is not valid for $L = R$ because of equation (1.26). However in this case, the exactly confocal, we obtain equation (1.29) directly substituting $L = R$ in (1.24).

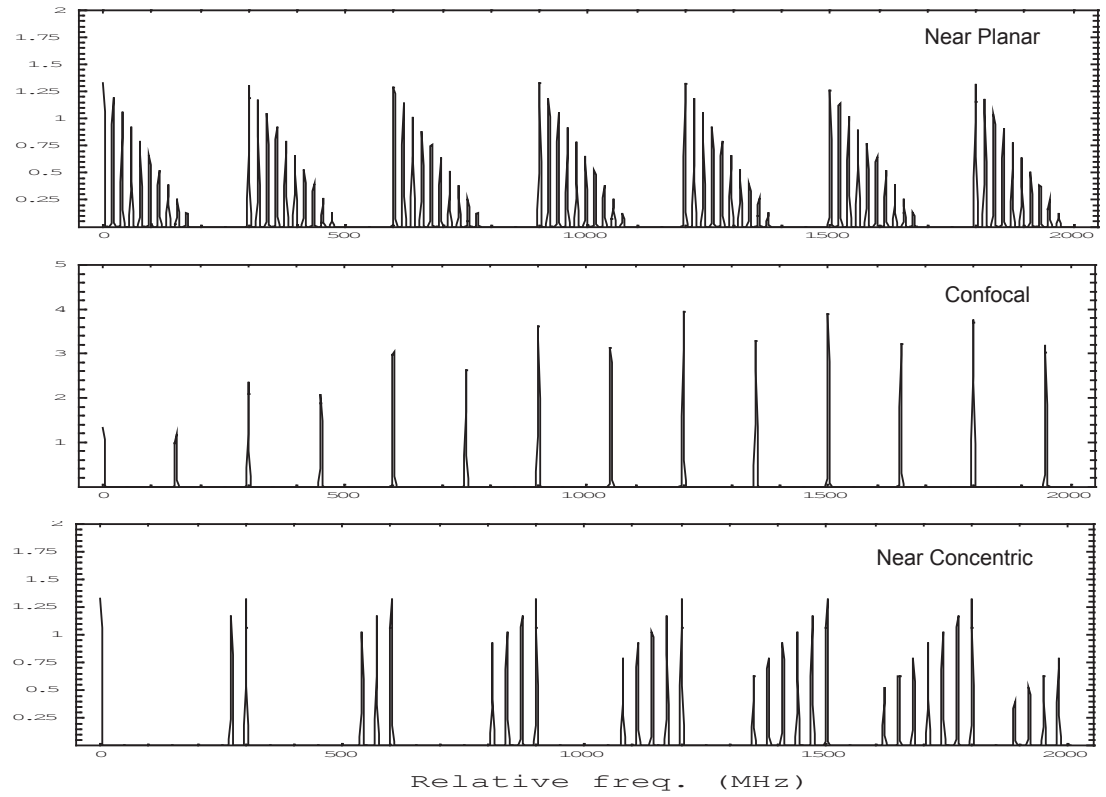

Figure 1.11: Simulation of axial and transverse mode frequencies for a near planar, confocal and a near concentric resonator. In the simulations of the confocal and near concentric situations there are some imperfections in the first groups, where less peaks are summed togheter.

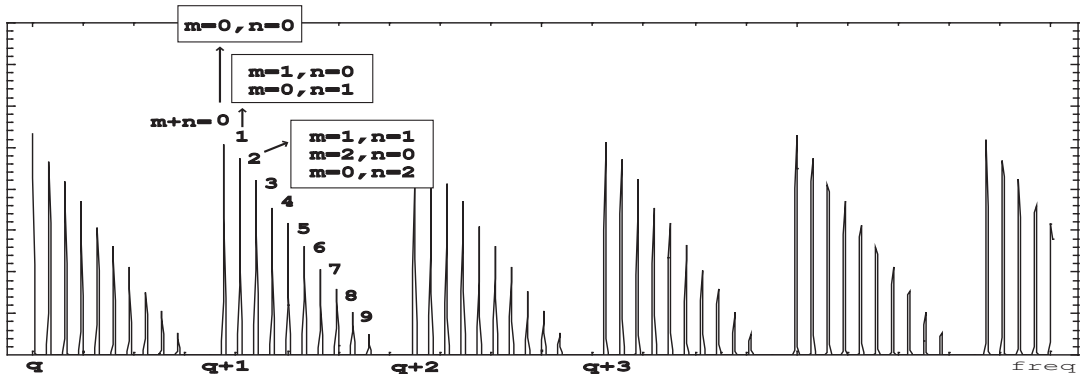

Figure 1.12: Distribution of axial and transverse modes (m,n) (the simulation has been performed with $L = 400\,\text{mm}$ and $R = 3000\,\text{mm}$)

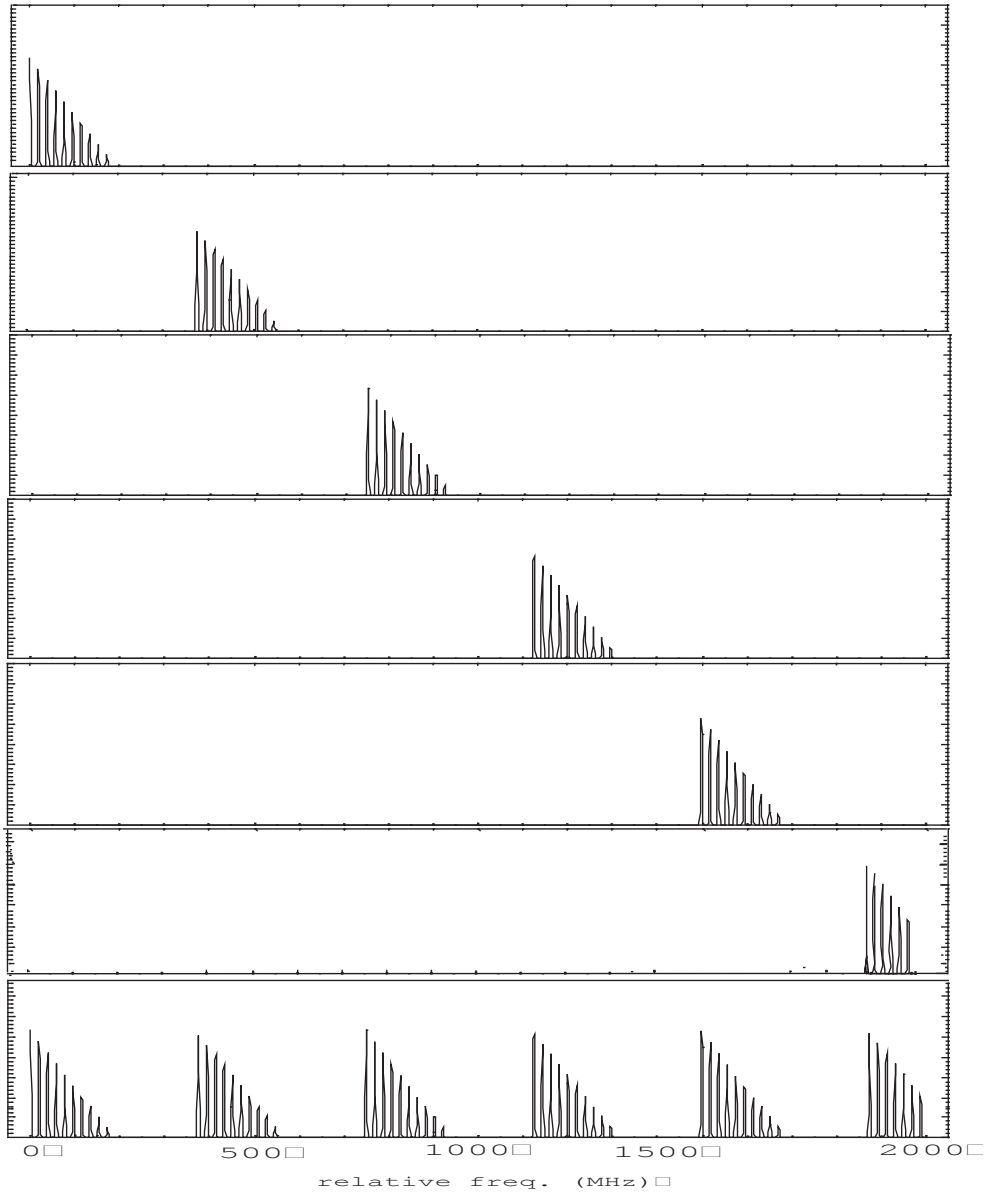

Figure 1.13: How the simulation program works: different series of high order transverse peaks, shifted to the right frequency distance, are plotted separately or summed up in the last graph (the simulation has done with $L = 400\,\text{mm}$ and $R = 3000\,\text{mm}$).

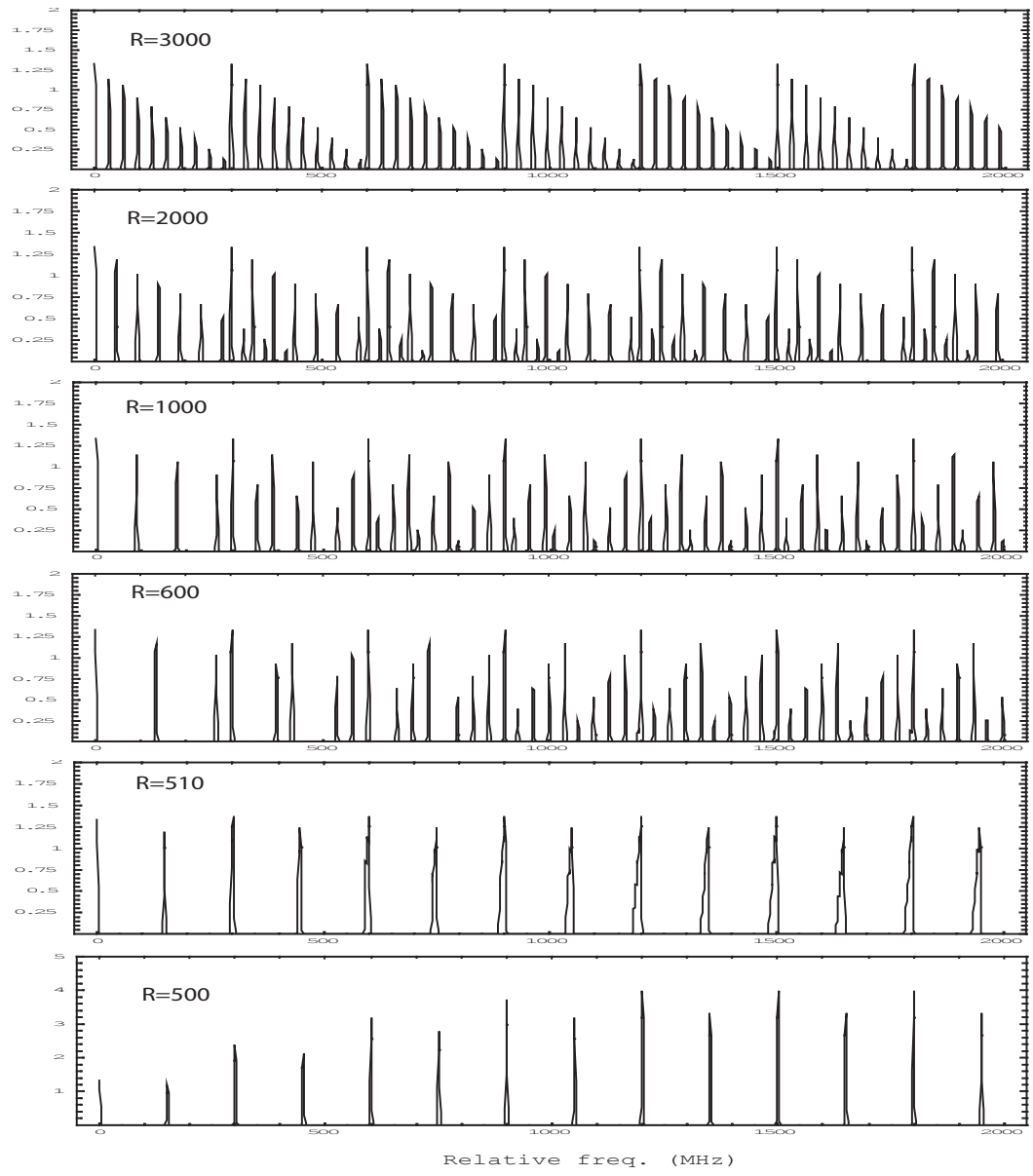

Figure 1.14: Simulation of the spreading of eigenfrequencies upon changing the radius of curvature of the mirrors from 3000 mm to 500 mm for a cavity of $L = 500$ mm. Every group corresponding to one axial mode q spreads out until the confocal degenerated situation shown in the last line at the bottom is reached.

1.2 Iodine absorption spectroscopy

Already in 1814 Joseph von Fraunhofer (1787-1826) discovered coincidentally a set of several hundred dark lines appearing against the bright background of the continuous solar spectrum. After a systematic study and careful measurement of their wavelengths, he mapped over 570 lines, called later Fraunhofer lines in his honor. The nine most prominent sets of series he labeled with capital letters A to K. At the time there was no explanation of the phenomenon. Some decades later it was understood that these dark spectral lines correspond to frequencies absorbed by the gases in the sun's atmosphere. A lot of work was done in the following years in order to measure the intensity values of the Fraunhofer lines and plot in this way the first atlases of the solar spectrum. From this letter delivered by M.G.F.Minnaert to George Darwin on 1947 [11] it is clear that an atlas of the solar spectrum and a first theoretical explanation of this were known in those years.

Exploiting the same phenomenon a glass cell containing gaseous iodine is used in our experiment to measure its absorption spectrum. As described in more details in the next section 2, a part of a single frequency laser beam is directed into an iodine cell and with a photodiode the transmitted intensity measured. In figure 1.15 it is reported as example the measured transmitted light in a 30 GHz scan of the laser, as a function of the laser frequency. Minima of the transmitted light (black lines) correspond to the frequencies absorbed by the gas.

Excited molecules emit isotopically, as shown schematically in figure 1.16 and this can

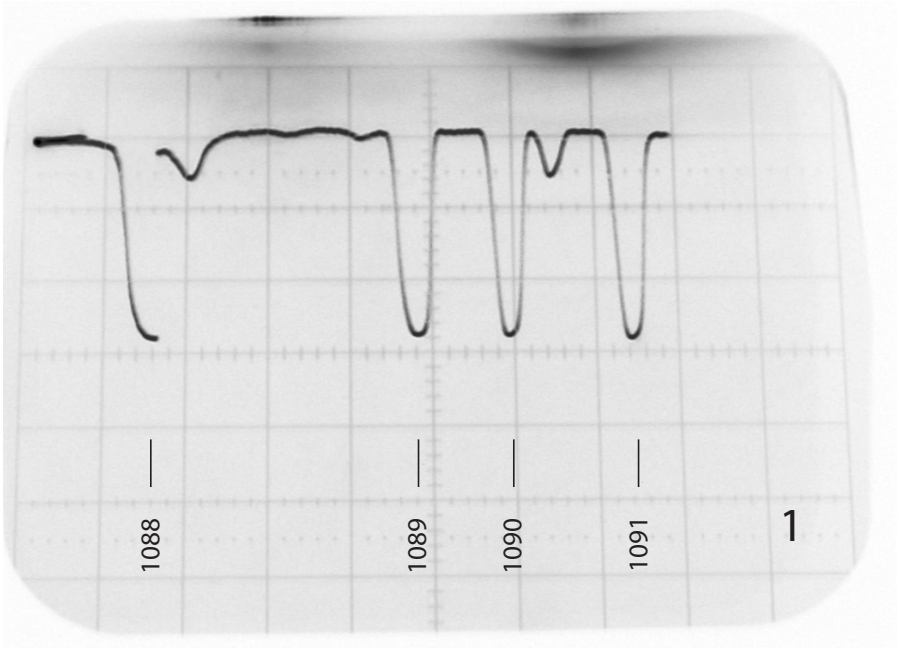

Figure 1.15: Some measured absorbed lines of iodine: the laser scan is 30 GHz wide and the absorbed intensity is measured via photodiode and visualized on a scope. In figure the numbers of the lines as reported in [8] are indicated.

be observed as a bright line along the iodine cell (if it's in the visible spectral range). Particularly one will observe fluorescence of the gas at those frequencies where the trans-

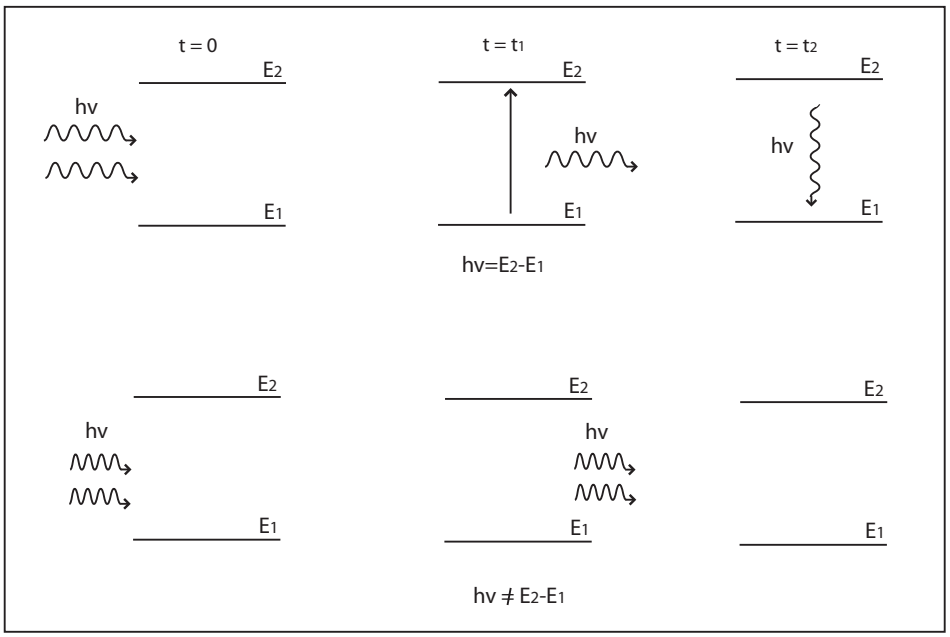

Figure 1.16: Schematics of absorbed and emitted light when there is resonance with one level of the molecular gas (first example) and when there isn't (second example). In the first case the absorbed light is emitted in all the directions after the life time t_2 of the level and some other goes through the cell. In the second case the light doesn't react with the gas and whole goes through the cell.

mitted intensity is minimal and viceversa. Using the tabulated frequencies of the iodine lines [8], it is possible to measure and calibrate the laser frequency with an accuracy of approximately 200 MHz.

As shown in the measured lines in picture 1.15, absorbtion peaks are not infinitely sharp lines but have finite widths. There is a *natural linewidth* due to the finite lifetime of the excited states according to the Heisenberg uncertainty principle, which asserts: if a system exists in a certain state for Δt seconds, then the energy of that state will be uncertain by ΔE according to:

$$\Delta E \Delta t \geq \hbar \tag{1.32}$$

This prevents us from knowing the energy difference precisely and broadens the peaks to a minimal natural width of approximately 0.2 MHz[5]. From figure 1.15 it is obvious that the linewidth in our measurements is about 1 GHz. In a low-pressure room-temperature gas the main source of broadening is the *Doppler effect* related to the thermal motion of the molecules in the gas.

Let us focus our attention on a particular transition between two levels E_1 and E_2 which gives as result a line at the energy:

$$h\nu_0 = E_2 - E_1 \tag{1.33}$$

When a laser beam propagates through a molecular gas cell, a molecule with velocity v in the direction of propagation of the light will absorb photons with frequency $\nu = \nu_0(1 + v/c)$. Whereas a molecule with velocity in the opposite direction absorbs photons of frequency $\nu = \nu_0(1 - v/c)$. Considering now the velocity distribution of molecules in a

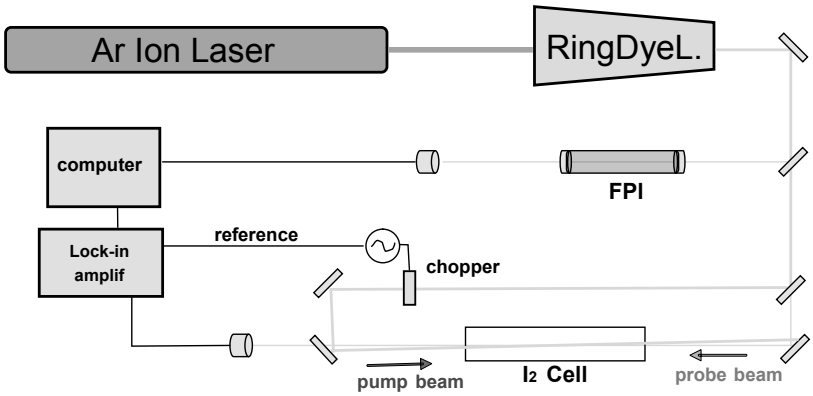

Figure 1.17: Experimental setup of a Doppler-free absorption spectroscopy.

gas at temperature T (one dim. *Maxwell-Boltzmann distribution*), we find the number of molecules moving with velocity v in a small velocity interval between v and $v + dv$ in the direction of propagation of the light, as:

$$n(v)dv = N\sqrt{\frac{m}{2\pi kT}}\,\exp\left(-\frac{mv^2}{2kT}\right)dv \tag{1.34}$$

where N is the total number of molecules and m their mass[4]. The intensity of the absorbed radiation as a function of the frequency is then given by:

$$I(\nu) = I_0 \exp\left[-\frac{mc^2(\nu-\nu_0)^2}{2kT\nu_0^2}\right] \tag{1.35}$$

where I_0 is the absorbed intensity for $\nu = \nu_0$. This profile has a Gaussian shape and the corresponding linewidth ($FWHM$) [Hz]

$$\delta\nu_D = 7.16 \cdot 10^{-7}\nu_0\sqrt{\frac{T}{M}} \tag{1.36}$$

where M the mass of a mole. The expected Doppler linewidth of iodine ($M = 106$) absorption peaks at $T = 300\,\mathrm{K}$ and $\nu = 531\,\mathrm{THz}$ (approx 564 nm) is 0.6 GHz, three orders of magnitude bigger than the natural linewidth.

A more elaborated technique called *Doppler-free saturated absorption spectroscopy* can be used to minimize the effects of the Doppler broadening and to measure narrower line shapes. The idea is to split the laser beam into two counter propagating parts: a weaker *probe beam* and a more intens *pump beam* (see figure 1.17). The pump intensity is used to saturate the transition and the probe beam, passing through the saturated medium, will experience an increasing transparency. Considering molecules in random thermal motion in the gas and remembering that pump and probe beams are directed in opposite

[4]In this distribution are already taken in consideration molecules with velocity in both the directions; it is valid for positive and negative velocities v. Moreover for molecules moving in all the other directions it is important to consider only the velocity component along the direction of propagation of the light.

directions, it is understandable that only molecules with velocity near to zero interact with both laser beams and only these molecules will experience an increased transparency. If then the pump beam is chopped by a mechanical chopper, the alternating transparency so produced in the probe beam passed through the cell can be detected with a photodiode by a lock-in amplifier referenced to the chopper. Being this modulated transmitted probe beam relative only to molecules with velocity close to zero, the Doppler linewidth of the signal observed by the lock-in detector is drastically reduced to a few MHz.

More details about this and a Doppler-free high resolution spectral atlas of iodine in the frequency range 15000 to 19000 cm^{-1} are reported in [10].

Chapter 2

Experimental Setup

The general scheme of the laser system set up is shown in figure 2.1. The system consists

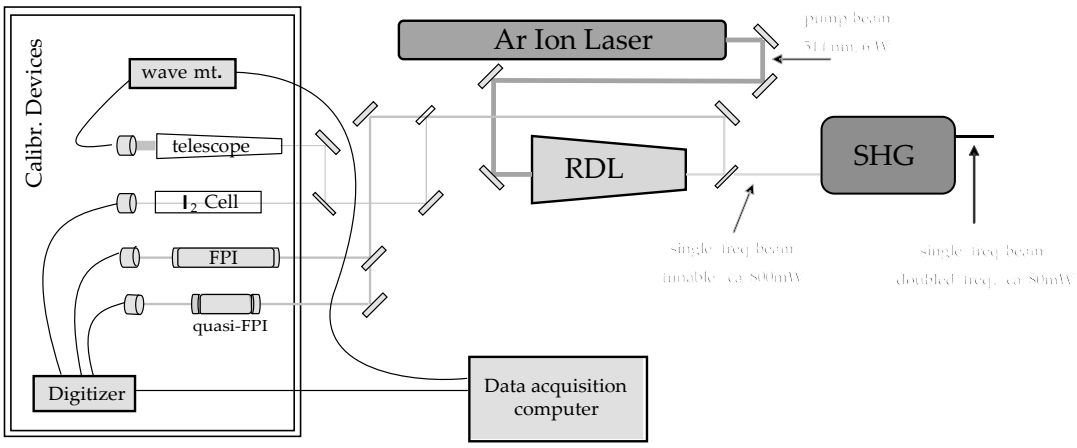

Figure 2.1: Schematic of the laser system: The Ar^+-ion laser is operated single-line to produce 6.5 W at 514 nm. This radiation pumps the ring-dye-laser operating on Rhodamine 560, typically generating 800 mW of continuous narrow-linewidth radiation around 550 nm tunable over a 50 nm range. Through the second harmonic generator the frequency is doubled and the power reduced to about 80 mW. Calibration devices allow to finely tune the frequency.

of an Ar^+-ion laser, a ring-dye-laser, a second harmonic generator and calibration devices, described in more detail below. The system generates continuous radiation in the visible and UV spectral range with a sub-MHz linewidth. The generated light is used for high resolution spectroscopy of large cold molecules.

2.1 Lasers and second harmonic generation

The Ar^+-ion laser (*Coherent Innova Sabre*) is operated single-line to produce 6.5 W at 514 nm. This radiation pumps the ring-dye-laser (*Coherent 899-21*), operating on Rhodamine 560, typically generating 800 mW of continuous narrow-linewidth radiation around 550 nm tunable over a 50 nm range.

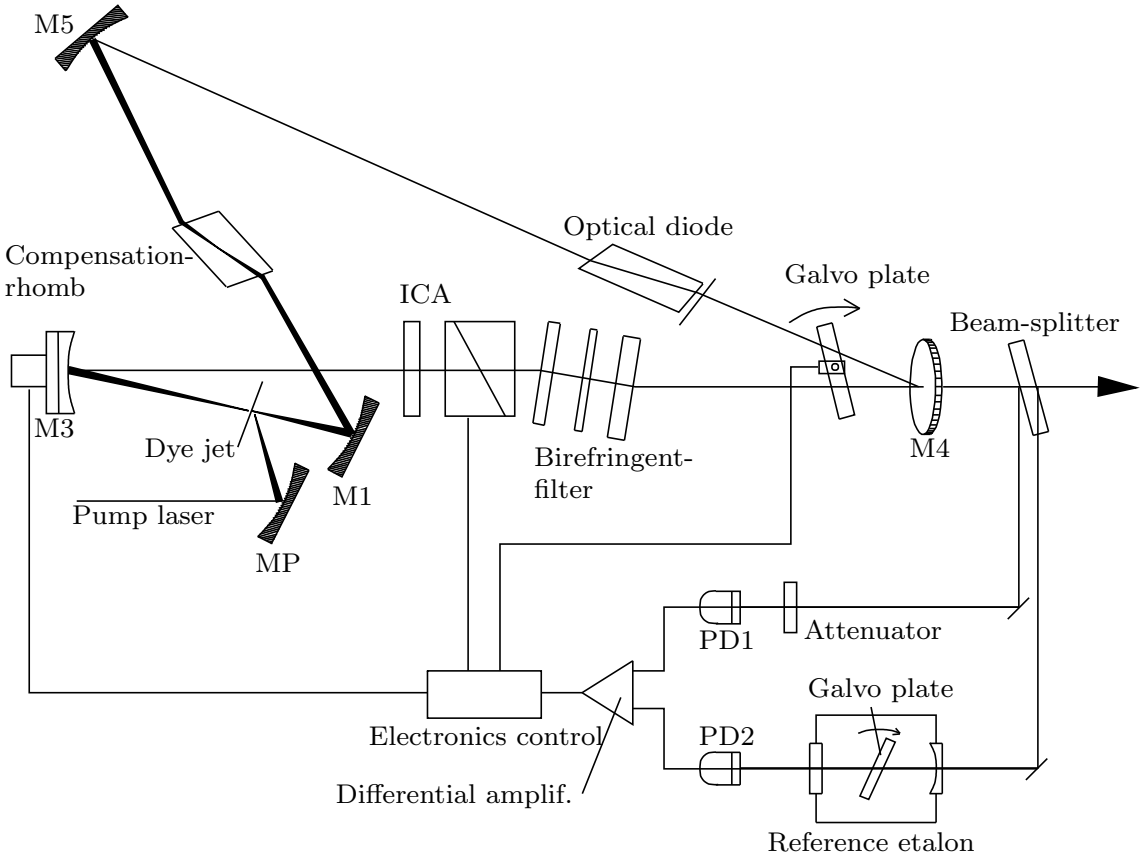

Figure 2.2: Schematic of the Ring Dye Laser cavity and active frequency controller

The resonator of the laser is a ring cavity composed of four mirrors ($M1, M3, M4, M5$) as shown in figure 2.2. There is a mode selection due to the cavity length L:

$$n\lambda = L \tag{2.1}$$

For the 1.5 m long ring cavity of the *899-21* the modes are spaced by approximately 200 MHz. A triple plate birefringent filter is used for coarse wavelength selection. An intracavity etalon assembly (ICA), which consists of a thick and a thin etalon, the operational bandwidth is narrowed to 75 MHz (see figures 2.3). Using an optical diode consisting of an optical rotator and a Faraday rotator unidirectional lasing is achieved in order to avoid competition for the gain between the two counter propagating waves and consequently loss of power.

A beamsplitter, placed outside the laser cavity behind the output coupler $M4$, splits the laser light into three beams (see figure 2.2). The biggest portion is transmitted and it corresponds to the output light of the ring dye laser. Others two parallel beams are reflected from the parallel surfaces of the beamsplitter and directed to a temperature stabilized linear interferometer (master cavity) and to an attenuator respectively. Two photodiodes, $PD2$ and $PD1$, measure the intensities of the transmitted light. The two voltage signals so generated are inputs of a differential amplifier which amplifies the differences from these two signals. Hence, when the laser frequency drifts from the lock point, a change in transmission through the master cavity is detected (the light through the attenuator remains the same) and an error signal is produced at the output of the differential amplifier. Setting a good lock point (not at the top of a master cavity transmission peak

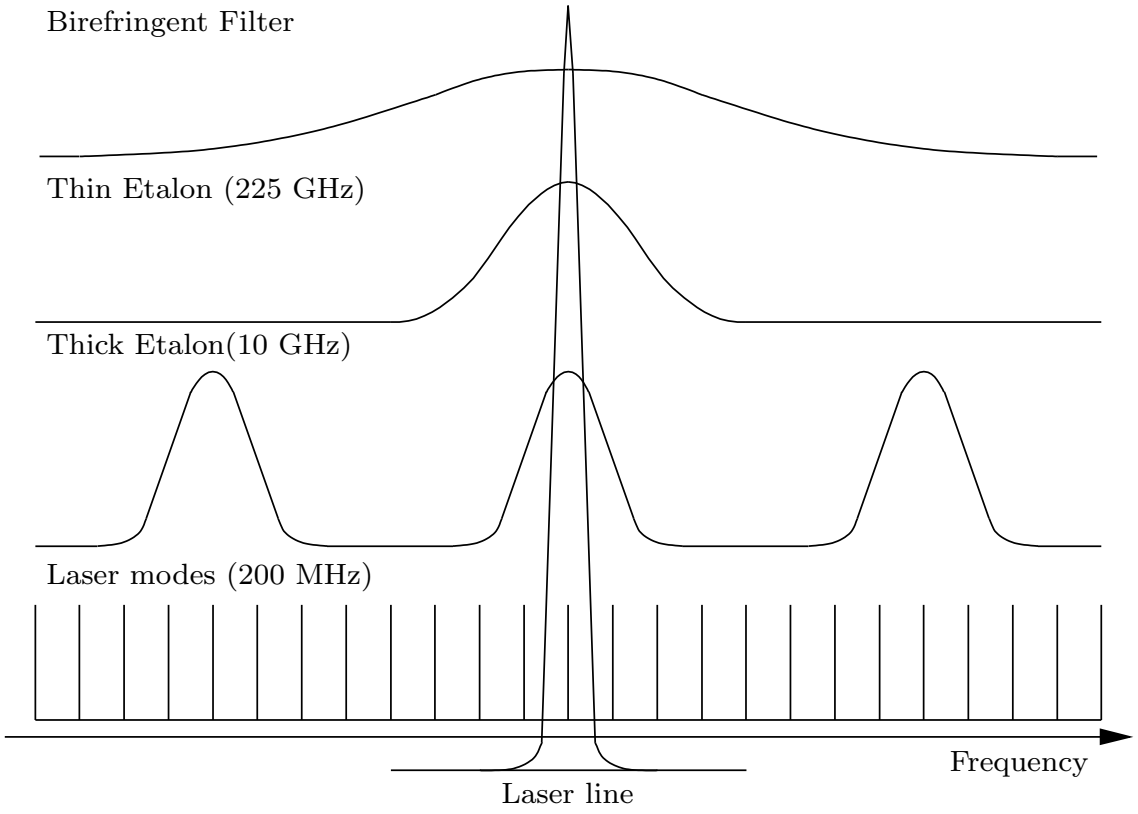

Figure 2.3: Selection of the laser mode through the different optical elements

but at a middle height), the direction of the change (higher or lower transmission values) gives information on whether the laser cavity must be shortened or lengthened in order to properly compensate. The derived error signal is applied to the piezo-driven mirror $M3$ (*tweeter*) and to the rotating Brewster plate in order to compensate for fast and slow cavity length variations, respectively.

Using this active frequency control the linewidth can be narrowed to circa 500 kHz. Varying the optical path length of the cavity by tilting the galvanometer motor driven Brewster plate, the laser frequency can be scanned up to 30 GHz single-mode operation, typically 800 mW at 546 nm in our experiments.

The single-frequency laser light generated is then directed into a second harmonic generator (*SHG*, *LAS Wave Train*). The exploited effect is the non-linear relationship between the strength of the electric field of the injected light wave and the polarization of the material. The ring cavity (see figure 2.4) is formed by two mirrors and a prism and translating the prism along its symmetry axis via a piezoelectric transducer, the cavity is tuned. The resonator stores the energy of many light round-trips. In this cavity design a prism instead of two mirrors is used due to the fact that the losses produced by Brewster surfaces are much smaller than the transmission losses of dielectric mirrors. Therefore the substitution of two dielectric mirrors by a brewster angle element result in a considerably reduction of the losses in the resonator. Two lenses are used to mode match the cavity to the laser beam. 135 mW of ultraviolet light have been produced at 273 nm in this way in the experiment described in section 3.3.

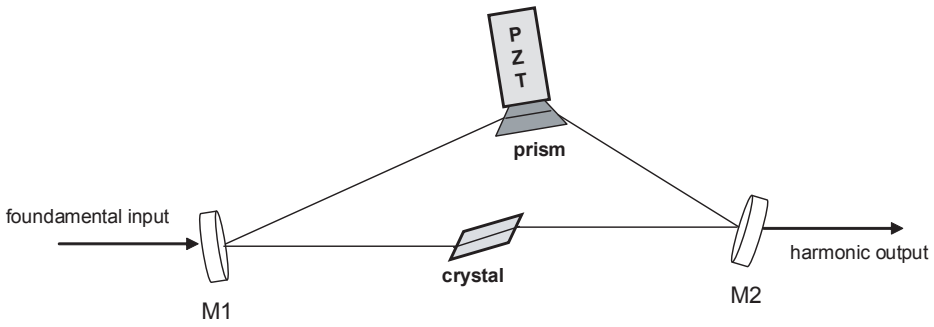

Figure 2.4: Second harmonic generator ring cavity

2.2 Calibration Devices

A small amount of light from the *RDL* is directed to the calibration devices, i.e. homebuild confocal Fabry-Perot interferometer (FPI), homebuild quasi-confocal Fabry-Perot interferometer, iodine cell and a wave meter, as shown in the laser system scheme in figure 2.1. These components are used to tune with high precision the frequency of the radiation generated in the ring dye laser and doubled in frequency in the second harmonic generator. The transmission signals of the two interferometers and of the iodine cell are simultaneously recorded via photodiodes and stored by a sampling data receiver system.

The wave meter's digital read-out gives an absolute value of the frequency of the light with an accuracy of 700 MHz (technical specifications: absolute accuracy 700 MHz, relative accuracy 10^{-6}, display resolution 0.0001 nm). The measured iodine spectrum allows to calibrate the laser frequency to 200 MHz by means of an offline comparison to the tabulated spectrum. The two interference patterns, of about 150 MHz and 50 MHz free spectral ranges, are high resolution frequency scales for relative measurement of the frequency.

2.2.1 Confocal Fabry-Perot interferometer

The most important requirements this interferometer has to satisfied are to produce well defined peaks, with really stable free spectral range, in the wavelength range $500-750\ nm$. A good value for the FSR has been thought to be 150 MHz.

The cavity is two identical concave mirrors separated by their common radius of curvature. In order to fix their distance they are mounted on a *Zerodure tube (SCHOTT, expansion class 1)*, with a central bore hole as shown in figure 2.5. The expansion coefficient of *Zerodure* is $0 \pm 0.05\ 10^{-6}K^{-1}$. With a such low thermal expansion material the distance between the mirrors remains almost constant in time and for temperature variations on the optical table, typically $< 1K$. Relative changes of the FSR smaller than $5\ 10^{-8}$ for temperature variations of 1 K are expected, i.e. variations of 7.5 Hz/K for a FSR of 150 MHz in our case. Taking into account that the interferometer is mounted on a thermally stabilized optical table (1 K according to the table specifications), the expected changes of the FSR are smaller than 7.5 Hz.

The mirrors are mounted on the tube through two homebuild cylindric caps of stainless steel, see figure 2.6. They are pushed against the faces of the tube using springs. The front surfaces of the mirrors remain at a fixed distance L, the length of the tube, because

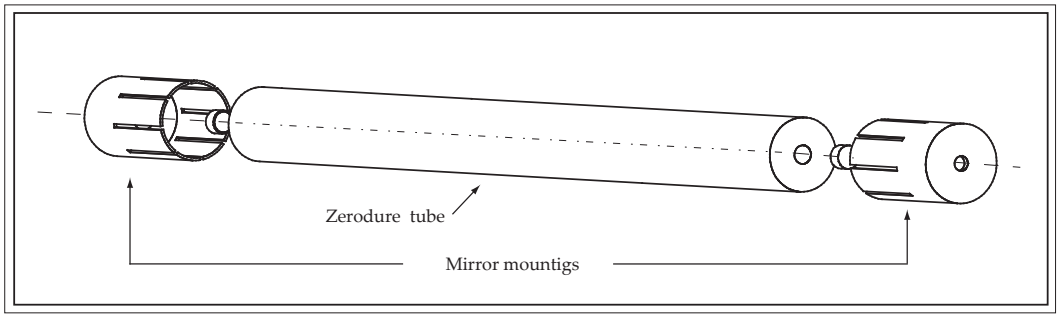

Figure 2.5: Explosion drawing of the confocal Fabry-Perot interferometer.

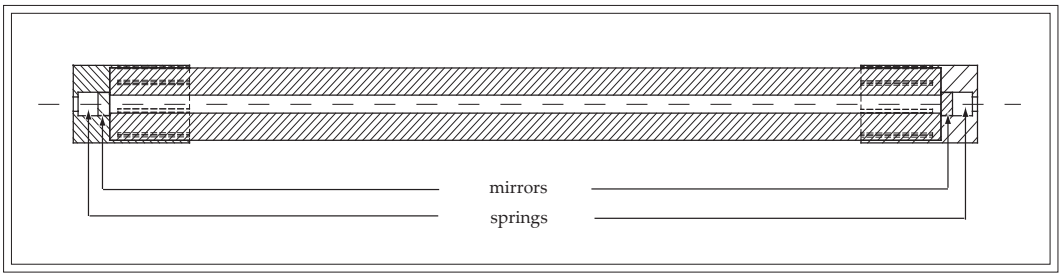

Figure 2.6: Technical drawing of the assembled confocal Fabry-Perot interferometer. The caps where the mirrors lye are of stainless steel. Two springs are used to push the mirrors against the faces of the tube in order to compensate possible stretches of the caps due to temperature variations.

the springs compensate possible stretches of the caps due to temperature variations.

It is important to accurately choose the dimensions of the tube, the reflectivity of the mirrors, and their radius of curvature. For a FSR of about 150 MHz the length of the tube has to be around 500 mm. For this reason the radius of curvature we chose is $R = 500\,\text{mm}$. The length is $L = 499.9\,\text{mm}$, in the way that the distance between the vertexes of the mirrors is exactly equal to R. The accuracy of the length and the parallelity of the two faces are also crucial, because the mirrors cannot be adjusted otherwise. The length is specified to $\pm 0.05\,\text{mm}$ and the accuracy on the angle is $\pm 0.07\,^\circ$. The inner diameter of the tube (8 mm) has been chosen based on the calculations of the beam waist inside the cavity (see figure 1.9) and the outer one (40 mm) based on mechanical stability considerations.

The mirrors (*Laser Optik Garbsen*) have a HR coating on the concave surface ($99.5 \pm 0.1\,\%$ in the wavelength range 500-750 nm) and an AR coating on the outer plane (reflectivity $0.5 \pm 0.3\,\%$ between 500-750 nm). This results in an expected finesse of about 600 and a linewidth $\Delta\nu$ of approximately 0.25 MHz. All cavity losses, such as diffraction, absorption and scattering, decrease the total finesse and for this reason a larger effective linewidth has to be expected.

Calculations have been performed in order to understand the effect of slight deviations of L from R on the FSR (see figure 2.7). The assumed temperature variations don't affect the FSR and we can neglect them. In the calculations the expected imperfections on the

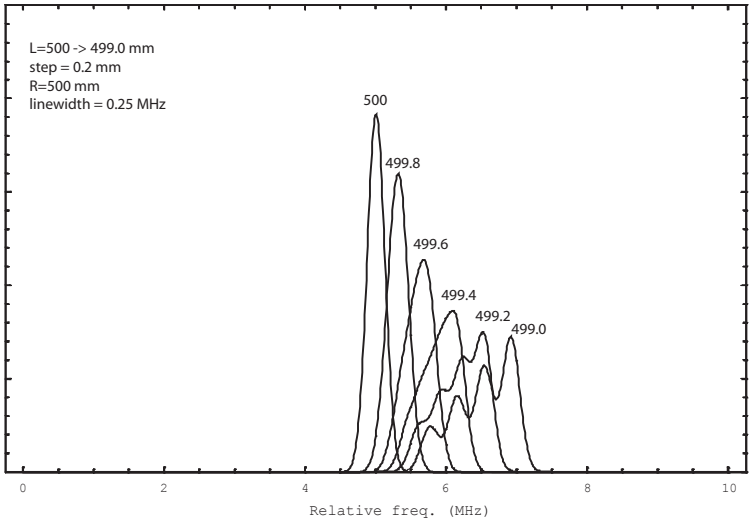

Figure 2.7: Peak shifts in the confocal interferometer interference pattern for different values of L/R.

constructions of L and R have been considered. In figure 2.7 six plots of the same spectral line are overlapped. For the different calculations R is fixed and L is changed with a step size of 0.2 mm. Two effects are observable: the FSR changes due to L and this appears as a shift of the peak; for values of L far from R (499.2 mm, 499.0 mm) visible higher order modes and considerable decrease in the intensity of the peaks have to be expected. In this respect a careful assembly of all the components will be crucial. In figure 2.8

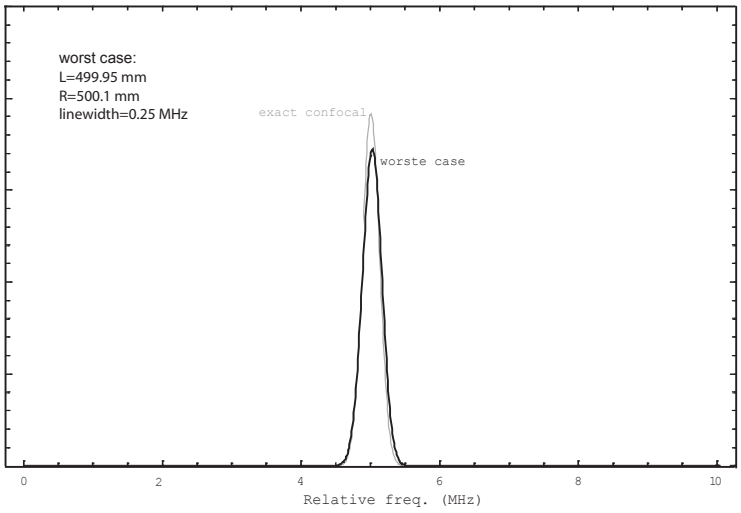

Figure 2.8: Comparison of the interference pattern obtained in exact confocal configuration (gray) and not exact confocal one (black) due to experimental imperfection.

the *worst case* assumption is considered: this is the case of the biggest expected value of R (500.1 mm) and the smallest expected value of L (499.95 mm) in relation with their specified accuracies. The plot is a comparison between the exact confocal case (gray line) and the worst case (black line) described above, zooming-in on a single peak. According to

the simulations we can conclude that even in the *worst case* the spreading out of the higher order modes is not observable. What is instead observable is a decrease of the intensity of the peaks of about one tenth respect to the confocal case. The linewidth widens a bit also but not considerably.

In order to prevent the system from humidity variations and consequent changes of the index of refraction n, the interferometer is put into an evacuated plexiglass housing (1 mbar).

Figure 2.9: Picture of the confocal interferometer.

2.2.2 Quasi-confocal Fabry-Perot interferometer

A second Fabry-Perot interferometer has been built in this work based on reference [6]. It exploits a superposition of higher order transverse modes different from that one of the confocal condition, which produces fringes separated by a smaller FSR using a smaller, compacter device. Adjusting the distance L between the mirrors of a symmetric quasi-Fabry-Perot interferometer to specific values different from $L = R$ corresponding to the confocal condition, it is possible to generate a pattern of fringes separated by ($n = 1$):

$$FSR = \frac{c}{2LN} \tag{2.2}$$

where $N > 1$ is an integer ($N = 2$ for a confocal interferometer). This means it is possible to obtain a FSR of about 50 MHz with an interferometer 10 cm long. In practice this is limited by the Finesse and the transmitted intensity of the peaks, which decrease with N.

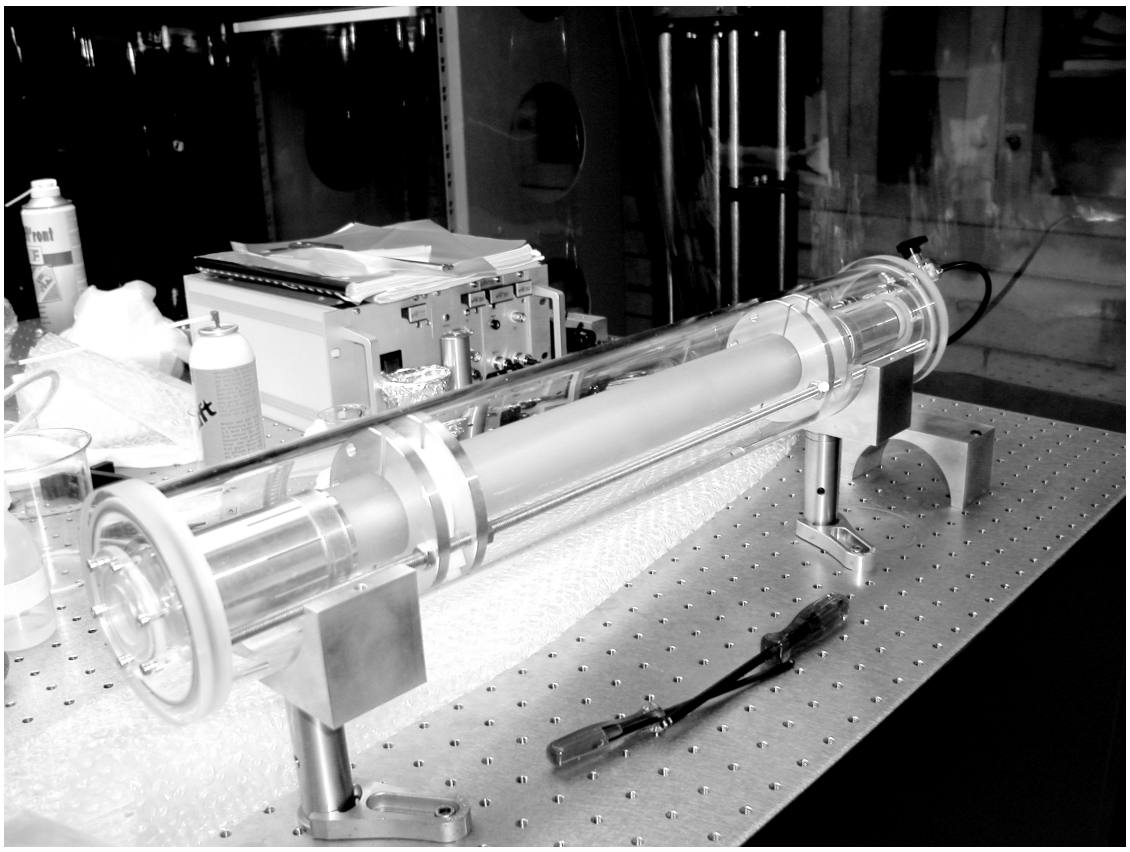

Figure 2.10: Picture of the confocal interferometer inside the plexiglass evacuated cover.

In figures 2.11 and 2.12 explosion drawing and technical drawing of this interferometer are shown. The structure is similar to the one described in section 2.2.1 except for

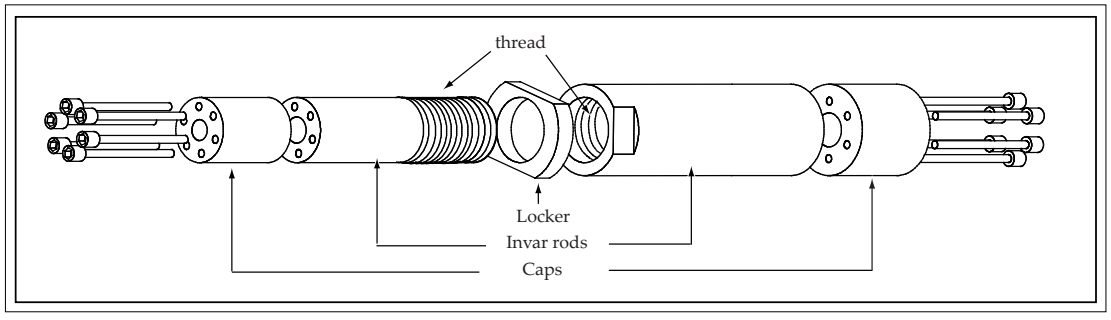

Figure 2.11: Explosion drawing of the higher order Fabry-Perot interferometer.

the tube consisting in this case of two rods screwed onto each other. The material used for these parts is *Invar 36*, a nickel-iron alloy with a low thermal expansion coefficient $(1.7 - 2.0\ 10^{-6}\,K^{-1})$. The caps in which the mirrors are mounted are made of stainless steel and also in this case two springs are used to push them against the tube. The mirrors (*Laser Optik Garbsen*), same specifications and same coating run of the other used for the confocal FPI, have radius of curvature of 100 mm. The distance L in between is adjusted looking for a good overlap of the modes different from the confocal one and

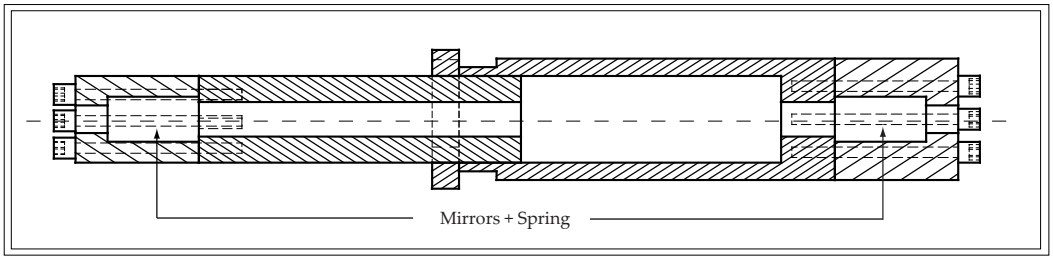

Figure 2.12: Technical drawing of the higher order Fabry-Perot interferometer.

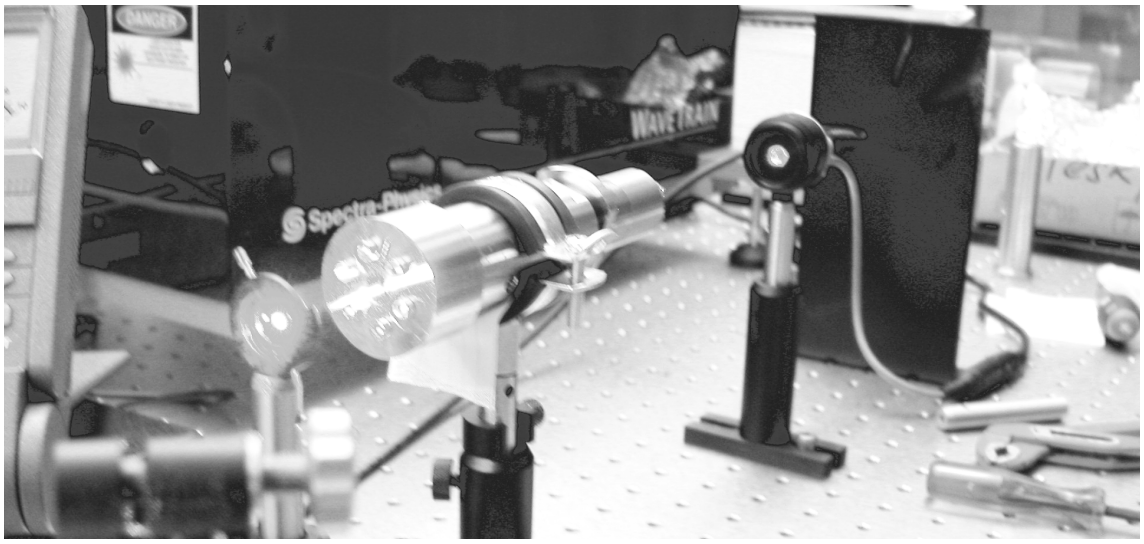

Figure 2.13: Picture of the quasi-confocal interferometer.

resulting in a FSR of about 50 MHz. Performing then a thread M22×0.75 on the Invar rods and assuming a sensibility of 2 ° in screwing them, a precision on the adjustments of L of approximately 5 μm is expected. A bolt (*locker*) is used to lock the relative position between the rods and fix the distance L.

The Mathematica code described in section 1.1.4 is used here again. The calculations are used to predict at which value of L a superposition of the higher modes resulting in a FSR approximately twenty times smaller than that one of the confocal situation is expected. A good overlap of the higher modes for $L = 105.56$ mm has been found corresponding to a FSR of about 50 MHz. The expected characteristics of the interferometer under these conditions are a finesse of 30 ($\pi\sqrt{R}/(1-R) \cdot 1/N$) and a linewidth of about 1.6 MHz. The fluctuations due to temperature variations on the FSR are in this case larger than those for the confocal interferometer, because of the larger thermal expansion coefficient of Invar. It is expected to be lower than 100 Hz/K.

Looking at the specifications of the two interferometers it is evident how one can perform an interference pattern of *higher quality* using the confocal interferometer than the quasi-confocal one. In fact in the first case the finesse is 20 times bigger and the expected fluctuations on the FSR are about 10 times smaller, than in the quasi-confocal

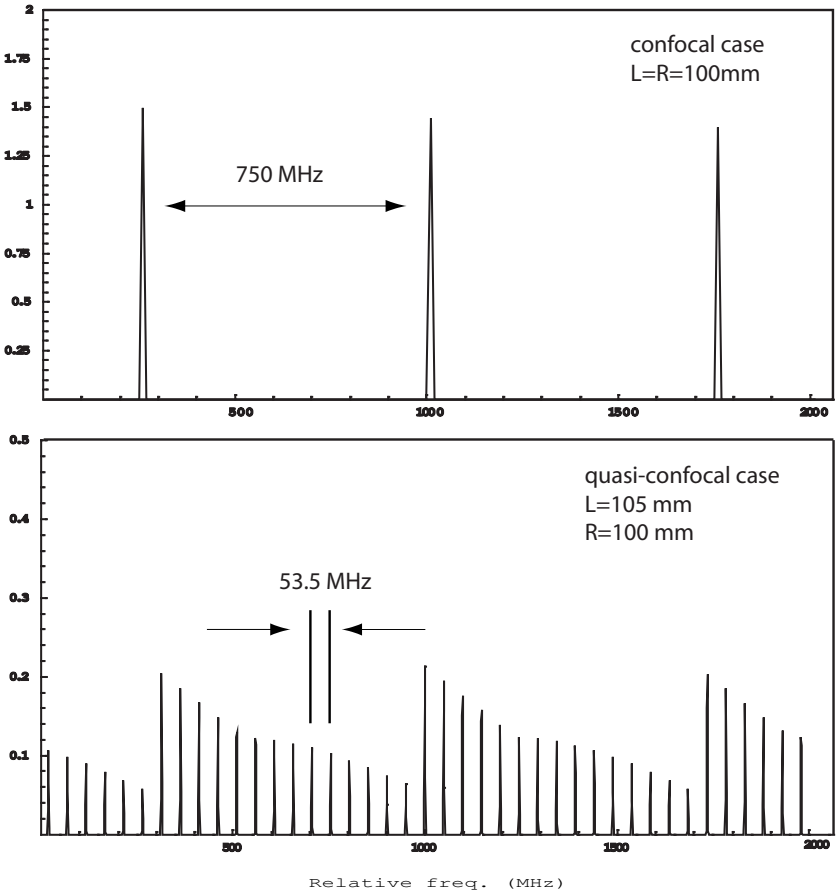

Figure 2.14: Simulation of an interference pattern for an interferometer with a 53 MHz FSR ($L = 105\,\text{mm}$). The transverse modes overlap here in a different way than in the confocal configuration resulting in a smaller FSR interference pattern.

one. On the other hand with the quasi-confocal interferometer one can obtain a well defined interference pattern with three times smaller FSR using a more compact and cheaper device.

2.2.3 Iodine cell

The iodine cell was build according to the specifications given in figure 2.15. The cell consists of a 500 mm long and 5 mm thick tube and with an outer diameter of 50 mm. The external windows, made of the same glass, are welded on the tube forming an angle of 34 ° as shown in the drawing reported in figure 2.15.

In this way a laser beam of the right polarization intersects the windows at *Brewster's angle* and reflections are minimized. A small tube connection is build up in order to put into the cell some iodine crystals, perform a pressure of approximately 0.4 mbar (vapor pressure of iodine at room temperature) and thus obtain a gas of iodine inside. The weld flange has been closed after insertion of iodine and subsequent evacuation of the cell using a turbo-pump stand.

The cell is tested measuring the absorption iodine spectrum for some peaks in the frequency range 17730-17732 cm^{-1} and the results are reported in section 3.2.

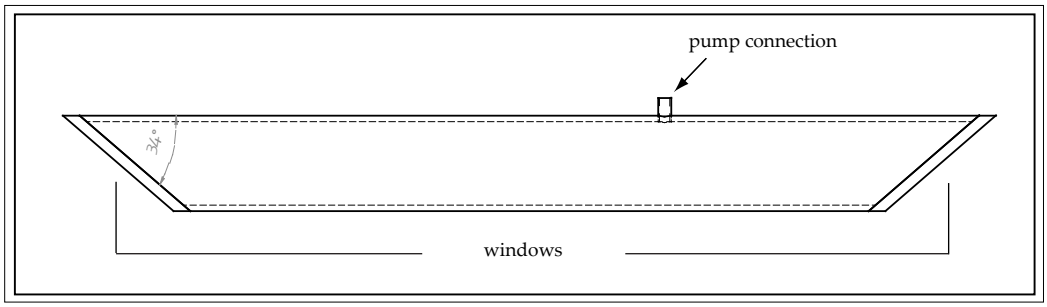

Figure 2.15: Technical drawing of the iodine cell.

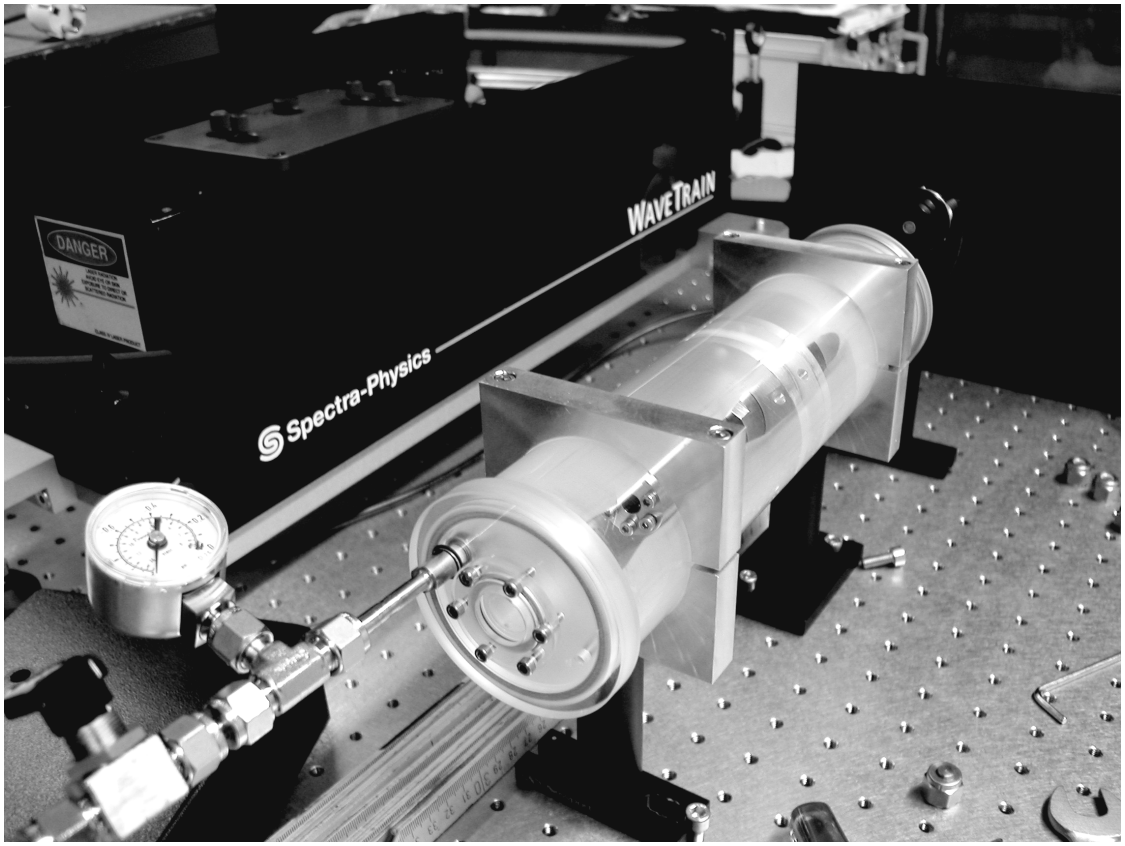

Figure 2.16: Picture of the quasi-confocal interferometer inside the plexiglass evacuated cover.

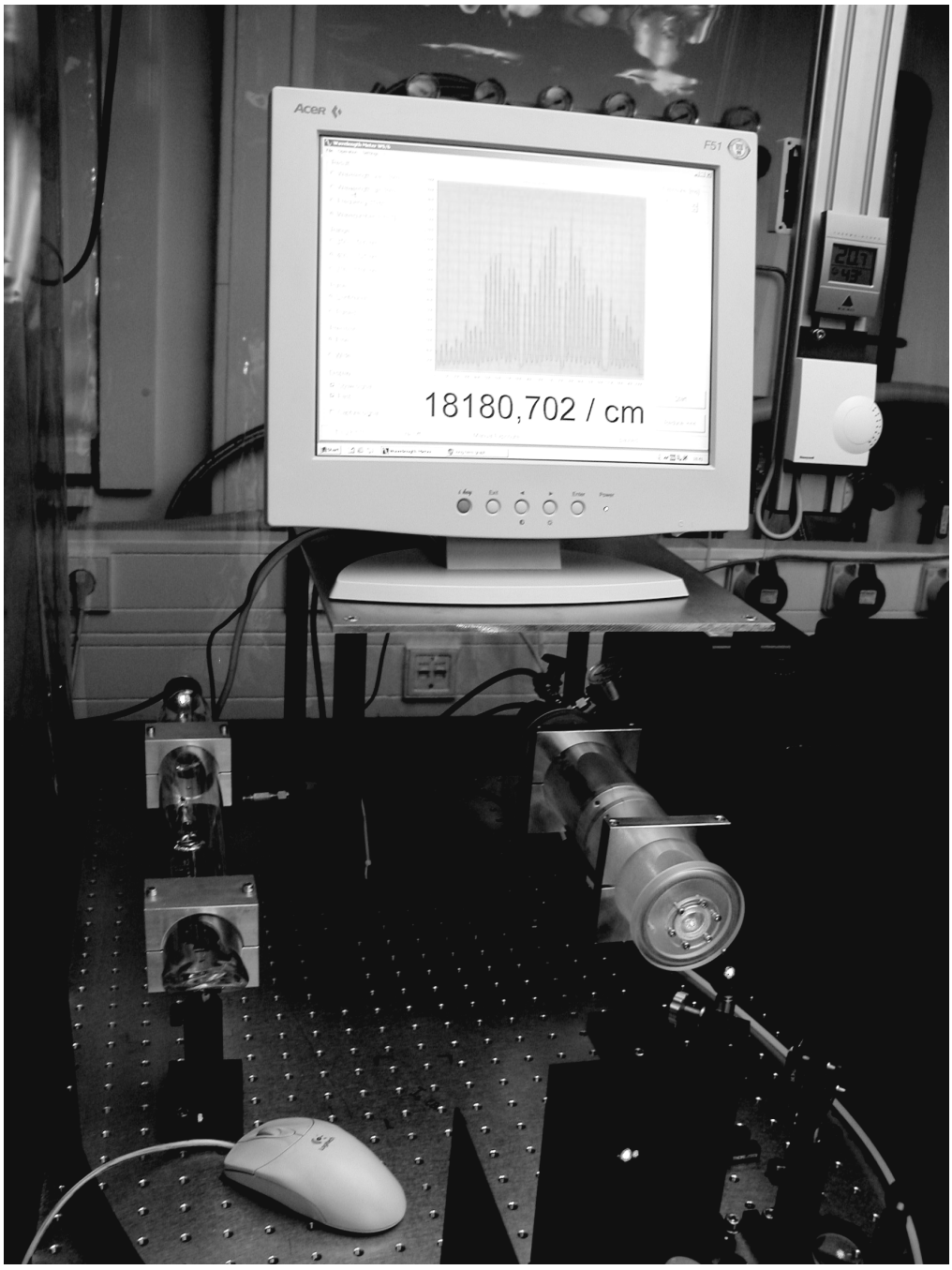

Figure 2.17: Picture of the calibration devices: iodine cell (left) and quasi-confocal interferometer. The free place in between is for the confocal interferometer.

Chapter 3

Results

3.1 Interferometers

Here the measurements performed in order to obtain the values of the FSR of the two interferometers are presented. The region in the frequency range 17883–18455 cm^{-1} is analyzed and 14 scans, each 1 cm^{-1} wide, are performed in that range. The experimental setup is shown and described in section 2) and consists of Ar^+-ion laser, ring dye laser and calibration devices (the two interferometers and the iodine cell). The laser power coming out from the ring dye laser was in the range 50–230 mW.

The generated radiation is directed to the two interferometers and to the iodine cell and standard photodiodes are used to measure their transmission signals. The laser power is recorded as well. A computer system samples simultaneously the voltages from the photodiodes and stores them in a data file. The sampling is performed at 100 Hz and the laser is scanned at $\sim$0.1 cm^{-1}/min. Files of four columns, each of them consisting of 60000 points, are created. Plotting them as a function of the point number, graphs like the one shown as example in figure 3.1 and 3.2 are obtained.

From the known iodine absorption lines, it is possible to calculate the free spectral range of both the interferometers dividing the frequency distance of the iodine lines by the number of interference peaks counted in between. Another approach is to assign at each iodine line a peak of the interference pattern (marker) and plot the frequency of the spectral lines as a function of the assigned number. The slope of the best fitting line with the plotted points, is the value of the FSR evaluated considering those points. An example of the calculations for the confocal interferometer, considering only one measurement (number 035) is explained in the following paragraph.

In figure 3.3 the points and the fitting line are plotted and the value of the FSR derived by linear regression is:

$$\mathrm{FSR} = 150.07 \pm 0.27\mathrm{MHz} \quad R = 0.999995, \tag{3.1}$$

where the 1σ standard deviation and Pearson's correlation coefficient R are given as error estimates.

In order to determine the FSRs for the two interferometers with high precision the number of points considered in the evaluation should be as large as possible. The standard deviation decreases in fact linearly increasing the considered number of points. To merge the points calculated from the data of two different measurements, one has to predict the exact number N of peaks between the two measurements. If this is done unambiguously, it is then possible to plot them in a single graph and to do a single common linear regression

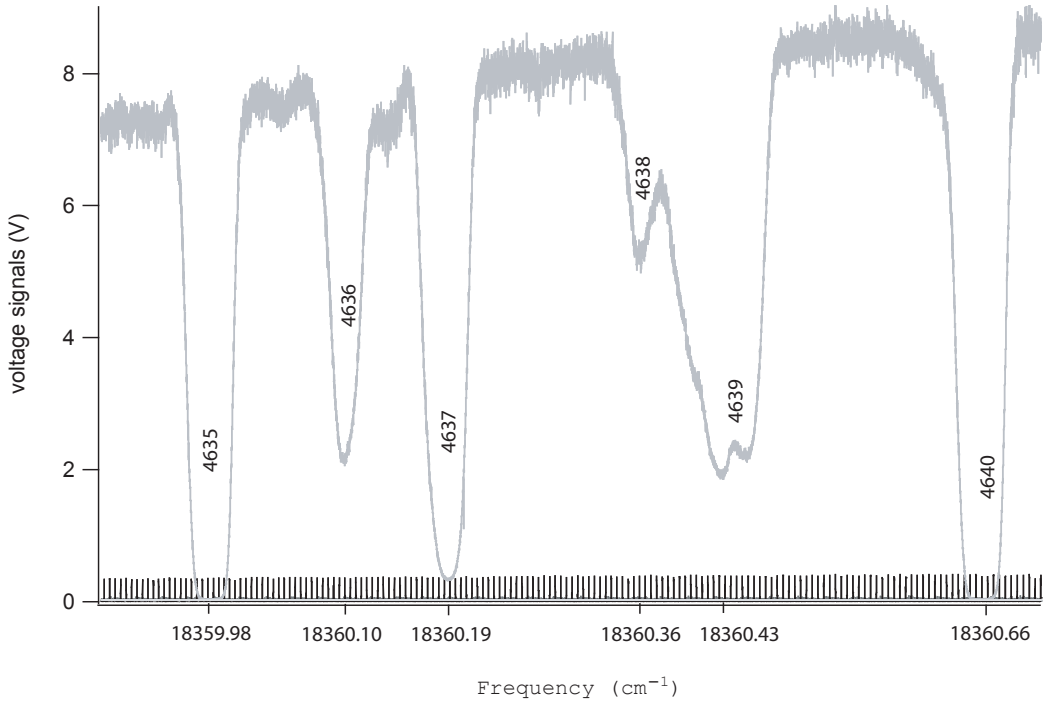

Figure 3.1: Example of the signals sampled by the data receiver system during a measurement of the interferometers characterization. The signals are respectively iodine cell transmitted intensity (big negative peaks in dark gray), confocal interferometer (positive peaks approx. 0.5 V high) and quasi-confocal interferometer (positive peaks less than 0.1 V high) interference patterns and laser power (almost constant signal of approx. 0.02 V). The numbers of the measured lines of the iodine spectrum and their relative frequencies are shown in the figure as written in [8].

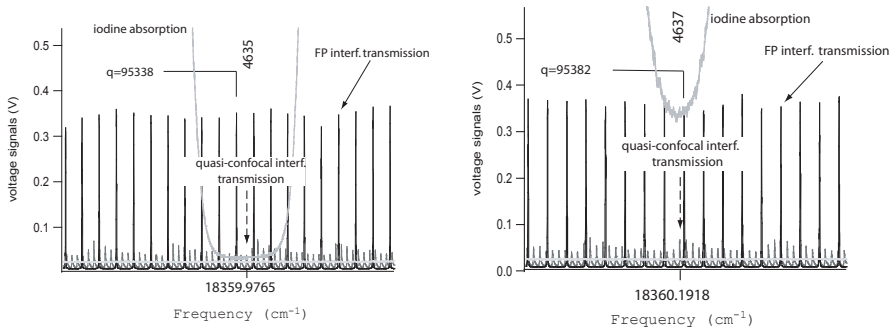

Figure 3.2: Zoom of figure 3.1 around two iodine lines: the numbers q of the peaks of the confocal interferometer interference pattern calculated starting from the iodine line 1848 are shown. The numbers q for all the data are reported in Appendix A.

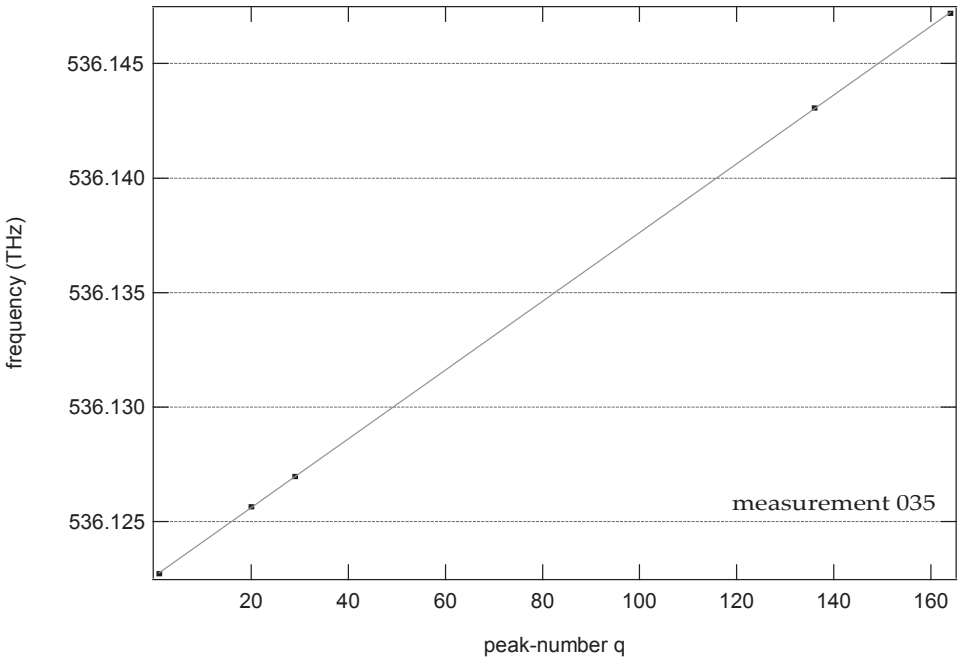

Figure 3.3: Plot of the peak-numbers q for the markers of iodine lines as a function of the frequency for a single measurement (number 035).

for both. The resulting standard deviation will be smaller and the value of the derived FSR known with higher precision. However, it is necessary to be sure that the predicted number N is unambiguously determined. This means that, in calculating N, one has to take into account the accuracy on the value of FSR calculated before. This limits the frequency range over which it is possible to predict N with certainty. An accuracy σ_{FSR_0} on the FSR_0 gives an uncertainty of at least

$$\sigma_N = N \cdot \sigma_{\mathrm{FSR}_0}/\mathrm{FSR}_0 \tag{3.2}$$

in predicting N peaks. Hence, with an accuracy of σ_{FSR_0}, one can make a good prediction, i.e. less than $\mathrm{FSR}_0/2\sigma_{\mathrm{FSR}_0}$ peaks approximately.

A *Python* program is used for these calculations. This procedure is applied to the data for both the interferometers. Details and results are presented in the next two sections.

3.1.1 Confocal interferometer results

The first two measurements put together (number 018 and 027) are separated by approximately $8\,\mathrm{cm}^{-1}$ (ca. 236 GHz). In order to make a prediction of N over this range, the FSR (around 150 MHz) must be known with an accuracy better than 0.05 MHz. First the FSR is calculated dividing the frequency difference from the first and last iodine lines for each measurement by the number of peaks calculated in between. The mean value of them, FSR(1) as shown in table 3.1, is known with an accuracy of 0.56 MHz. In step two a linear regression for the markers of all iodine lines in each measurement separately is performed using only integer numbers and fractional numbers. The mean values obtained, FSR(2) and FSR(3) in table 3.1, respectively have standard deviations of 0.12 MHz and 0.04 MHz. This allows to use the mean of FSR(3) to connect measurements 018 and 027,

meas. number	date	FSR(1)(MHz)	FSR(2)(MHz)	FSR(3)(MHz)
008	17/12/04	149.61	149.78 (62)	150.31 (31)
011	17/12/04	149.76	150.01 (38)	149.91 (11)
017	18/12/04	149.97	150.08 (57)	149.90 (13)
018	18/12/04	150.43	149.98 (70)	150.96 (38)
020	18/12/04	150.11	150.42 (69)	150.38 (7)
022	21/12/04	149.58	149.5 (62)	149.32 (34)
025	21/12/04	150.06	149.73 (134)	149.14 (41)
027	21/12/04	150.87	150.53 (126)	151.35 (93)
031	22/12/04	148.82	148.84 (42)	148.71 (10)
033	22/12/04	149.59	149.21 (48)	149.69 (25)
035	22/12/04	150.10	150.07 (27)	149.87 (9)
038	22/12/04	149.21	149.05 (47)	149.74 (28)
040	22/12/04	150.66	150.81 (32)	149.89 (11)
043	22/12/04	150.64	149.80 (50)	149.92 (28)
average		149.96 (56)	149.89 (12)	149.86 (4)

Table 3.1: Mean confocal interferometer FSR values calculated for each single measurement separately in three different ways. FSR(1) is calculated on the two most external lines, dividing the frequency separation by the number of peaks counted in between. FSR(2) and FSR(3) are calculated instead as the linear regression for the markers of the iodine lines in each measurement separately, taking in account only integer and fractional number respectively in numbering them. In the first two columns the measurement number as saved in the data archive of our department and the relative dates are reported.

resulting in $N = 1578$ peaks predicted in that range. Making a common linear regression of the markers of these two measurements, the precision on the known value of the FSR increases again. This allows to predict N over a larger range and to consider two other measurements together (number 022 and 025). Continuing this procedure, the points of all the measurements are plotted in a single graph 3.4.

The order of assignment is given in table 3.2 together with the various relative peak-numbers N. The number q (integer and fractional) of the 80 markers of the iodine lines considered in this evaluation in the frequency range 17883–18455 cm^{-1} are reported in Appendix A and plotted in figure 3.4. The value of the FSR of the confocal interferometer resulting from the final linear regressions of the assigned q (integer and fractional) are:

Linear regression for integer q:
$FSR = (149.946787 \pm 0.000235) MHz$
$R^2 = 0.999999999808$
Linear regression for fractional q:
$FSR = (149.948667 \pm 0.000218) MHz$
$R^2 = 0.999999999834$

An interesting test is performed finally (see table 3.3) in order to check the consistency of the N values calculated considering integer numbers reported in table 3.2. The same N are calculated here with the fractional numbers assigned to the markers. The obtained values are all consistent with the values of table 3.2 calculated before.

The best estimation to the value of the FSR of the confocal interferometer resulting from our measurements is 149.948667 ± 0.000218 MHz. This could be still improved by

measurements	N (integer))
n018 $<--->$ n027	1578
n022 $<--->$ n025	2726
n020 $<--->$ n027	3971
n017 $<--->$ n043	4383
n017 $<--->$ n040	5406
n020 $<--->$ n025	4247
n011 $<--->$ n031	8393
n008 $<--->$ n011	5591
n038 $<--->$ n040	8583
n031 $<--->$ n043	15735
n008 $<--->$ n018	8634
n022 $<--->$ n033	26024
n033 $<--->$ n035	17180

Table 3.2: Order of assignment and relative peak-numbers N calculated utilizing integer numbers.

performing an analysis on a larger frequency range but it is good enough to test the system in spectroscopy of cold molecules.

3.1.2 Quasi-confocal interferometer results

The same procedure is used to evaluate the value of the FSR for the quasi-confocal interferometer (around 50 MHz). The values reported in the third column of table 3.4 (FSR(3)) are calculated in this case utilizing the FSR of the confocal interferometer estimated before. Because of its small value, it results not so useful to use both integer and fractional numbers in the assignment of the relative peak-numbers q to the iodine lines. In each measurement the peaks of the two interference patterns which overlapped particulary well are considered and used, in place of the iodine lines, as relative frequency reference. The accuracy obtained in this way is 0.00867 MHz. Even if it looks like a good accuracy, it is still too big to predict unambiguously N also in the case of the two closest measurements, 018 and 027. This prevents us from evaluating the FSR of the quasi-confocal interferometer with better accuracy and from assigning to the peaks a number q, as done in the analysis of the confocal interferometer.

The best value obtainable from the analysis of our measurements is:

$$\mathrm{FSR} = (49.543 \pm 0.00867)\mathrm{MHz}$$

This could be improved by performing more measurements between those already obtained, if spaced closely enough that would allow to connect spectra from the different frequency ranges and successively improve the accuracy of the FSR-determination significantly.

It is noted that in calculating the averaged values in table 3.4, measurement 008 has not been considered since the FSR determined from 008 deviates strongly from all other measurements. The deviation cannot be explained but it has to be considered that measurement 008 was the first performed. We think that something wrong was probably in the alignment of the interferometer or in the vacuum.

N (integer)	N (fractional)
1578	$<--$ 1577.8
2726	$<--$ 2726.3
3971	$<--$ 3971.1
4383	$<--$ 4383.2
5406	$<--$ 5406.1
4247	$<--$ 4246.9
8393	$<--$ 8393.1
5591	$<--$ 5590.9
8583	$<--$ 8583.2
15735	$<--$ 15735.4
8634	$<--$ 8633.6
26024	$<--$ 24024.1
17180	$<--$17180.1

Table 3.3: Check of the predicted N values. In the first column the values calculated considering integer numbers are reported and in the second column the same N are calculated considering fractional ones

meas. number	date	FSR(1)(MHz)	FSR(2)(MHz)	FSR(3)(MHz)
008	17/12/04	40.15	40.17 (21)	39.95 (11)
011	17/12/04	49.91	50.16 (21)	50.27 (29)
017	18/12/04	49.13	49.16 (16)	49.19 (5)
018	18/12/04	48.82	48.75 (18)	49.74 (59)
020	18/12/04	49.17	49.18 (5)	48.97 (1)
022	21/12/04	49.09	48.99 (22)	49.20 (4)
025	21/12/04	48.82	48.88 (23)	48.83 (4)
027	21/12/04	49.59	49.44 (33)	49.00 (1)
031	22/12/04	48.86	48.87 (18)	49.11 (2)
033	22/12/04	49.03	48.95 (19)	48.98 (4)
035	22/12/04	49.33	49.44 (8)	49.61 (13)
038	22/12/04	48.84	48.70 (25)	49.06 (1)
040	22/12/04	49.29	49.23 (34)	49.03 (2)
043	22/12/04	48.49	49.10 (13)	49.21 (4)
average		48.28(260)	49.24 (6)	49.543 (9)

Table 3.4: Mean quasi-confocal interferometer FSR values calculated for each single measurement separately in three different ways. In the first two columns the measurement number as saved in the data archive of our department and the dates are reported.

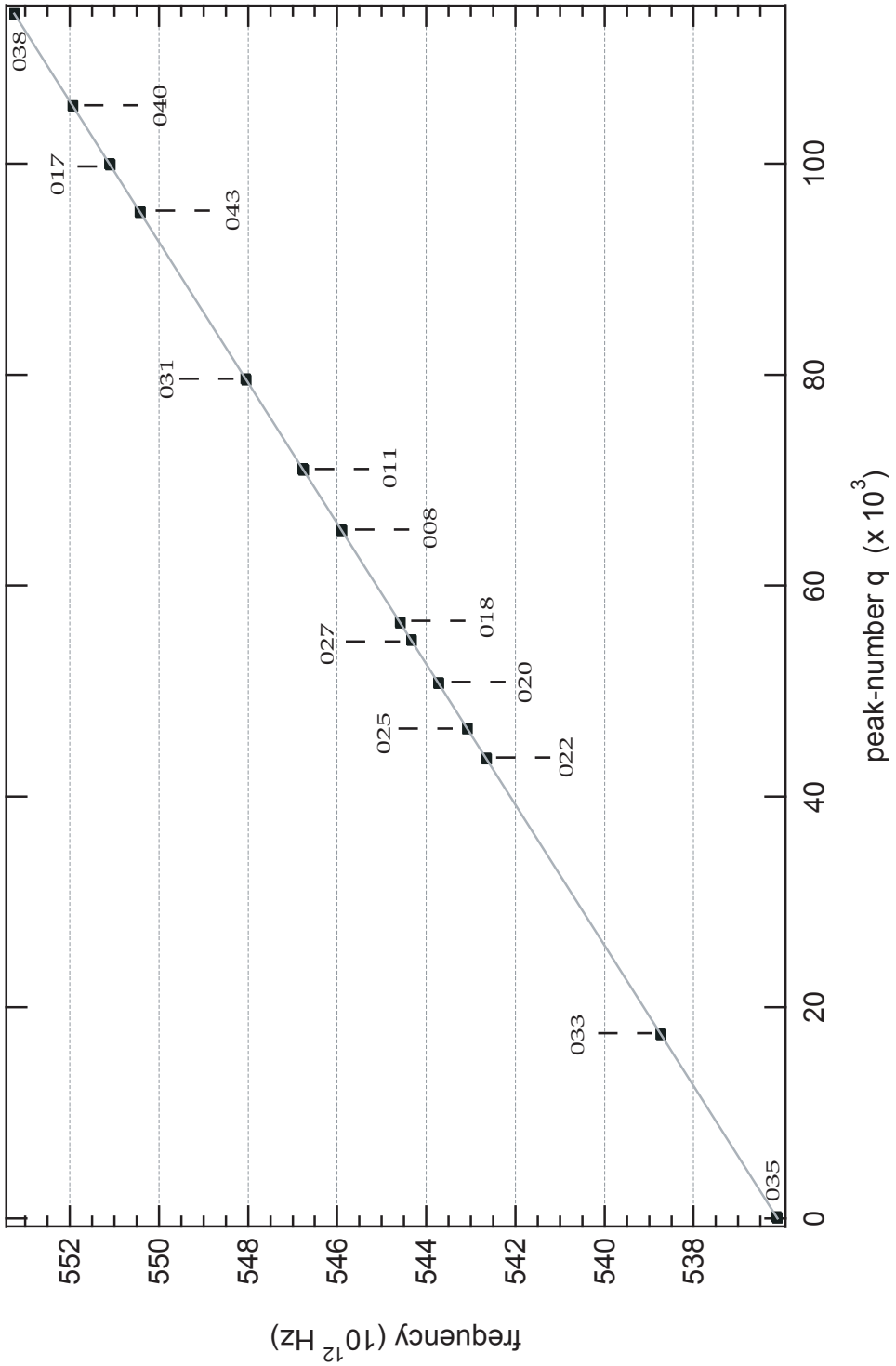

Figure 3.4: Plot of the peak-numbers q for the markers of the measured iodine lines reported in Appendix A as a function of the frequency.

3.2 Iodine absorption spectroscopy

In order to test the iodine cell some lines of the absorption spectrum of iodine (broadened by the Doppler effect) in the frequency range 17729-17732 cm^{-1} are measured. The single frequency laser scanned over a 30 GHz range (1 cm^{-1}) is at the same time directed into the wave meter and the iodine cell. Using a photodiode the transmitted intensity through the cell is measured and the signal is visualized on the scope as a function of the laser frequency. The region is then enlarged moving the frequency range of the laser scan and the pictures in figure 3.5 are obtained. Thanks to the wave meter (see 3.6) that gives

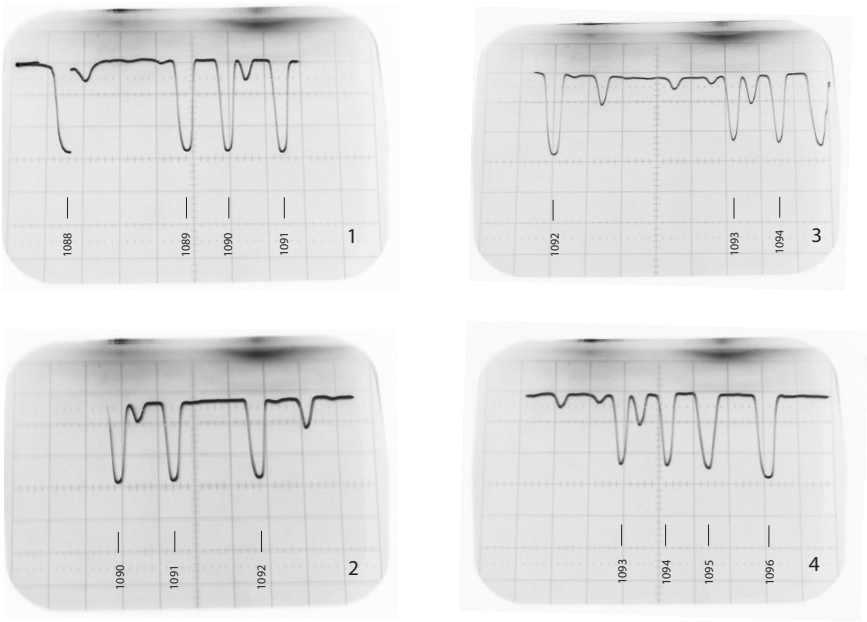

Figure 3.5: Measured iodine spectral lines (1088-1096) in the frequency range 17729-17732 cm^{-1} and their respective assignment from the iodine atlas [8].

a measurement of the frequency with an absolute accuracy of 700 MHz (approximately 0.024 cm^{-1}) it was quite easy to recognize the measured lines in the spectrum reported in the atlas [8]. The scanned region from the atlas is shown in figure 3.7.

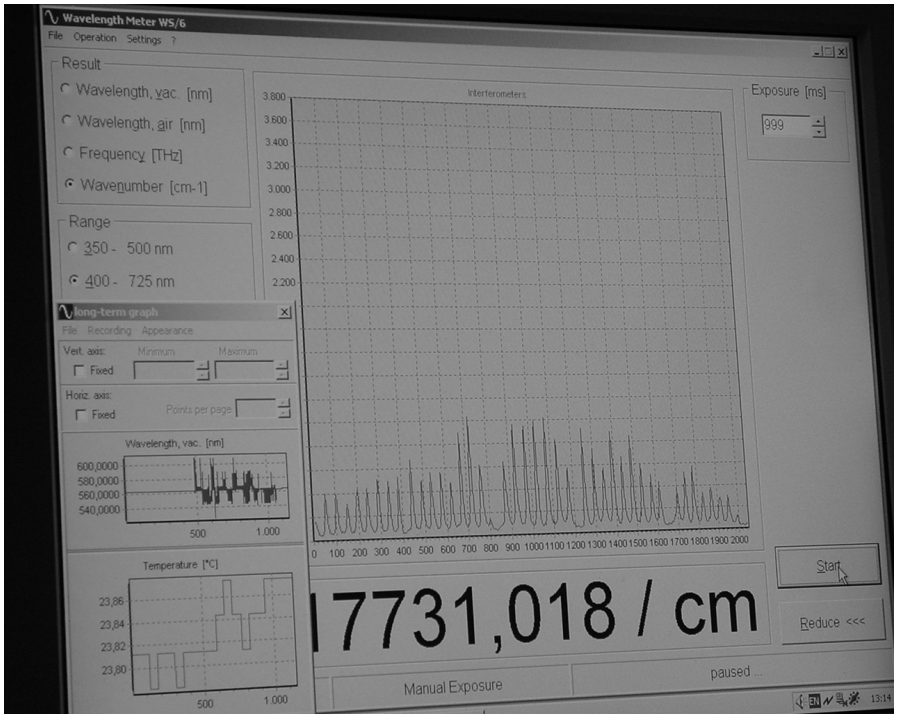

Figure 3.6: Display of the wavemeter: measurement of the laser frequency by the wavemeter.

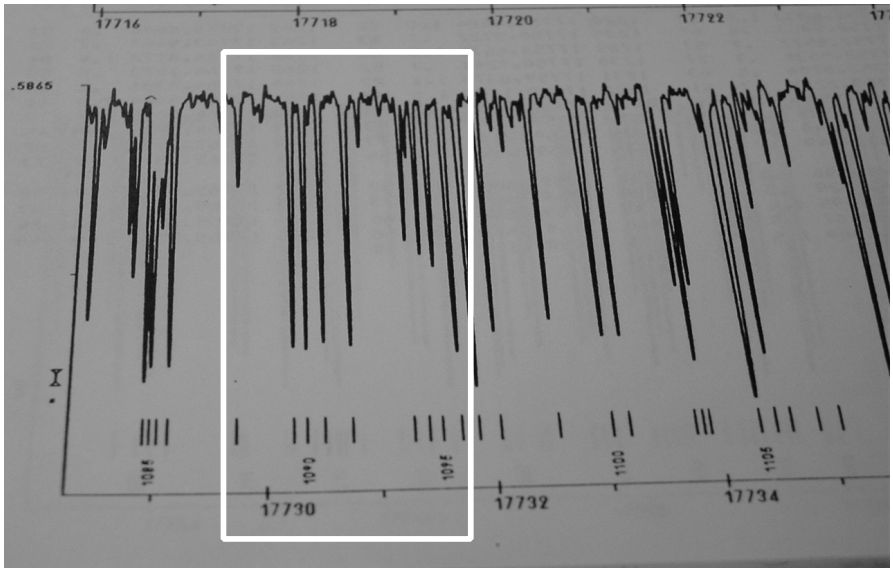

Figure 3.7: Atlas of molecular gas of iodine [8]. In the white square the frequency range scanned in the test of the iodine cell is shown.

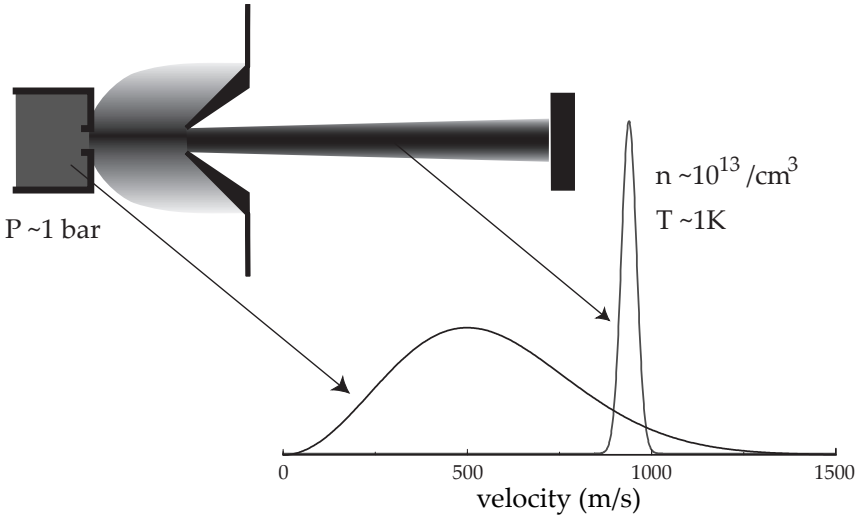

Figure 3.8: Schematic of a supersonic expansion.

3.3 OH molecular beam detection

The measurement of the *time of flight profile* (*TOF*) of OH radicals transported through a 1.31 m long stark decelerator is a first prototype experiment using the laser system described in section 2. The calibration devices were not available at that time and are not involved in this measurements. Using Rhodamine 6G and 6.5 W pump radiation (514 nm), approximately 80 mW of continuous ultraviolet light at 282 nm are obtained at the output of the *SHG*.

3.3.1 Deceleration of molecular beams

Stark deceleration of molecules exploits two fundamental phenomenons: the narrow velocity distribution of a supersonic expansion of a high-pressure gas into vacuum and the interaction between the dipole moment and an external electric field.

Supersonic expansion

A powerful and general method to cool a gas is by letting it expand through a nozzle into vacuum. Consider a container with a high pressure gas (typically 1-5 atm) with a small hole through which the molecules emerge into vacuum. The emerging beam of molecules is said to be effusive if the velocity distribution inside the container will not be disturbed by the presence of the hole and the velocity distribution in the beam is the same as it was in the container. This happens when the hole is much smaller than the mean free path of the gas (the mean distance that a molecule travels before it collides with another molecule). If, however, that hole is much larger than the mean free path something different happens: molecules close to the hole collide frequently but they experience in this case a net force pushing them towards the hole, because the collisions take place almost exclusively with molecules to the left of them. During the expansion the faster molecules collide with the slower molecules flying ahead and the average velocity in the beam is faster than the average velocity in an effusive beam. Moreover the velocity distribution for molecules in the beam is now narrower than for molecules in the container as shown in figure 3.8. Under

typical conditions, this corresponds to a translational temperature in the moving frame of the molecules in the beam of approximately 1 K. In order to obtain cold molecules in the laboratory frame, we need to transfer this narrow velocity distribution from the moving frame of the molecular beam to the laboratory frame.

Stark effect

The interaction of the dipole moment with an external electric field is also known as Stark effect. In figure 3.9 the relative potential energy of a molecule in an electric field is plotted as a function of the field strength for OH ($X^2\Pi_{3/2}, J = 3/2$) radicals. The states are classified according to their Stark-slope. In electric field of $100\,kV/cm$ the potential

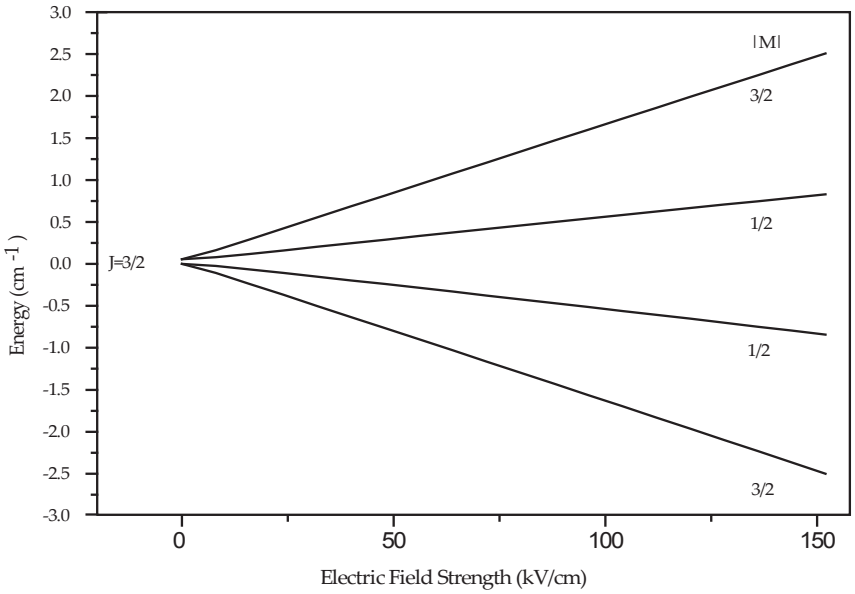

Figure 3.9: The Stark shift of OH ($X^2\Pi_{3/2}, J = 3/2$) radicals in an electric field up to $150\,kV/cm$. From [14].

energy of a molecule in a low-field-seeking state increases by approximately $1.5\,\mathrm{cm}^{-1}$ and consequently its kinetic energy and velocity decrease. Consider a molecule in a low field seeking state flying into an electric field generated by two parallel electrodes orientated perpendicular to the molecular beam axis with a voltage difference between them (see figure 3.10). The molecule will see a potential hill and will slow down (decelerate) while entering this field. In the same way it would accelerate while leaving the field due to the decrease of potential energy and it will regain the lost energy by increasing the kinetic energy. If, however, the electric field is abruptly switched off when the molecule is approximately at the top of the potential hill, its kinetic energy is ultimately reduced, and the molecules will keep their lower velocity.

Standard values of thermal kinetic energy of molecules at the room temperature are a few hundreds of wave numbers (Maxwell velocity distribution). Supposing now that electric fields on the order of 100-200 kV/cm are available, we cannot reduce the velocity of the molecules considerably by such a single step. Repeating this process letting the molecules pass through multiple pulsed electric fields, i.e. 100 stages (see figure 3.11), the velocity can be considerably reduced.

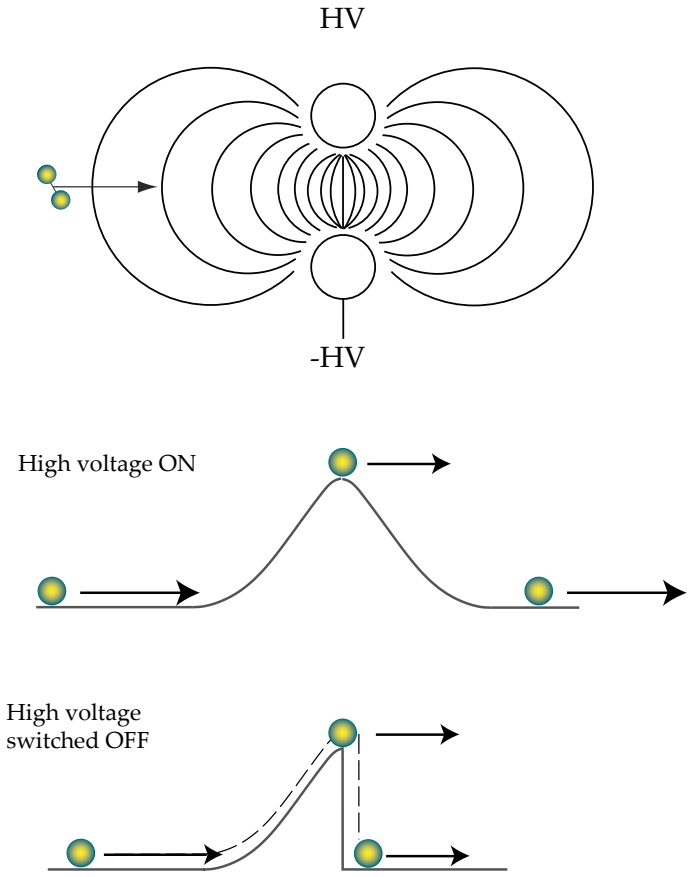

Figure 3.10: A polar molecule in an electric field.

The first successful decelerator for neutral molecules has been implemented by Bethlem *et al* in 1999 [2] and a beam of metastable CO molecules in low-field-seeking states was decelerated from 230 m/s to 98 m/s using 63 deceleration stages.

Many new experiments have been done in the last years using this technique: time varying electric fields have been used to change the longitudinal velocity of different polar molecules and static electric fields to focus and detect them [15]. Traps have been implemented to store decelerated molecules [1]. Metastable CO molecules in a high-field-seeking state have been focused and decelerated using electrodynamic dipole lenses in alternate gradient configuration [3]. An overview of this work and about its status can also be found in [4].

3.3.2 Experimental setup and results

The experimental setup used to measure the TOF of OH ($X^2\Pi_{3/2}, J = 3/2$) radicals is shown in figure 3.13. A pulsed beam of OH with a mean velocity of 460 m/s is produced via ArF-laser dissociation of HNO_3 seeded in Kr near the orifice of a pulsed valve. The production takes place at a well-defined time and position. Only OH radicals in low field seeking states are of relevance in this experiment. After passing through a 2 mm diameter skimmer, the molecular beam enters the deceleration chamber and is focused into the decelerator by a short hexapole. The decelerator used in this experiment consists of 108

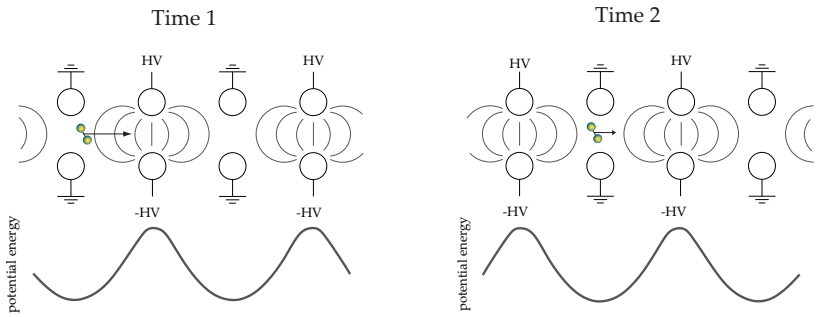

Figure 3.11: Switching of the electric field in a Stark decelerator.

stages and has a length of 1188 mm. The distance between the stages is 11 mm and the transverse acceptance area between two 6 mm diameter parallel electrodes, that make up one electric field stage, is $4{\times}4\,\mathrm{mm}^2$. The applied voltage difference of 40 kV is switched on and off in an electric field stage. For a detailed description see reference [14].

Behind the decelerator the molecular beam is crossed by the CW-laser beam and the integrated fluorescence of OH is detected by a photomultiplier tube (PMT).

The purpose of the experiment is to measure the intensity of the LIF signal of OH ($J = 3/2$) radicals as a function of the time for a non-decelerated and a decelerated molecular beam. When the decelerator is off the peak of the TOF-signal is expected at 2.8 ms. The LIF signal intensity has been then measured three times separately and each time it has been averaged 1064 times directly in the scope (the molecular beam machine runs at a 10 Hz repetition rate). The baseline is measured separately and subtract from the signal to obtain a plot of the first peak reported in figure 3.14, corresponding to non-decelerated molecules.

The same measurements are performed with the decelerator on: the expected velocity of the decelerated molecules leaving the decelerator is 170 m/s and the time of flight from nozzle to detector around 4.3 ms. This result is the second peak in figure 3.14, corresponding to decelerated molecules.

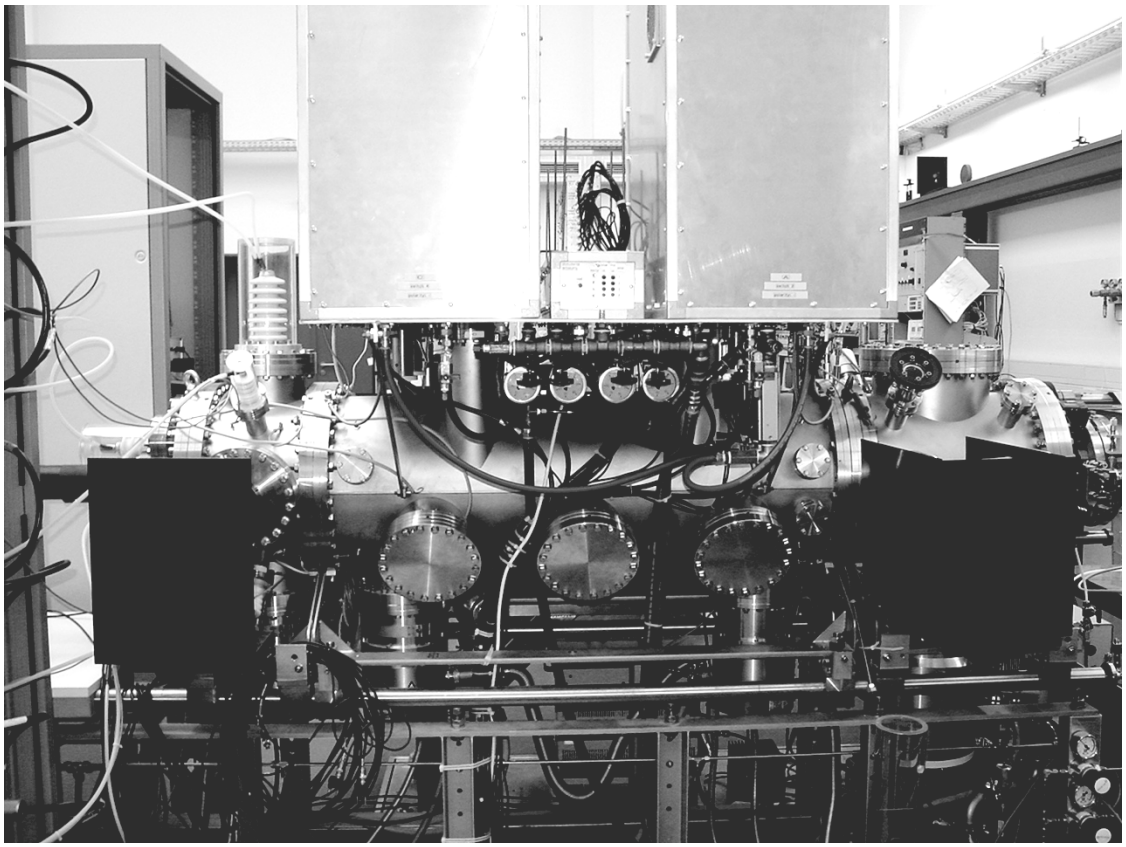

Figure 3.12: Picture of the machine used to produce and decelerate the OH-radicals

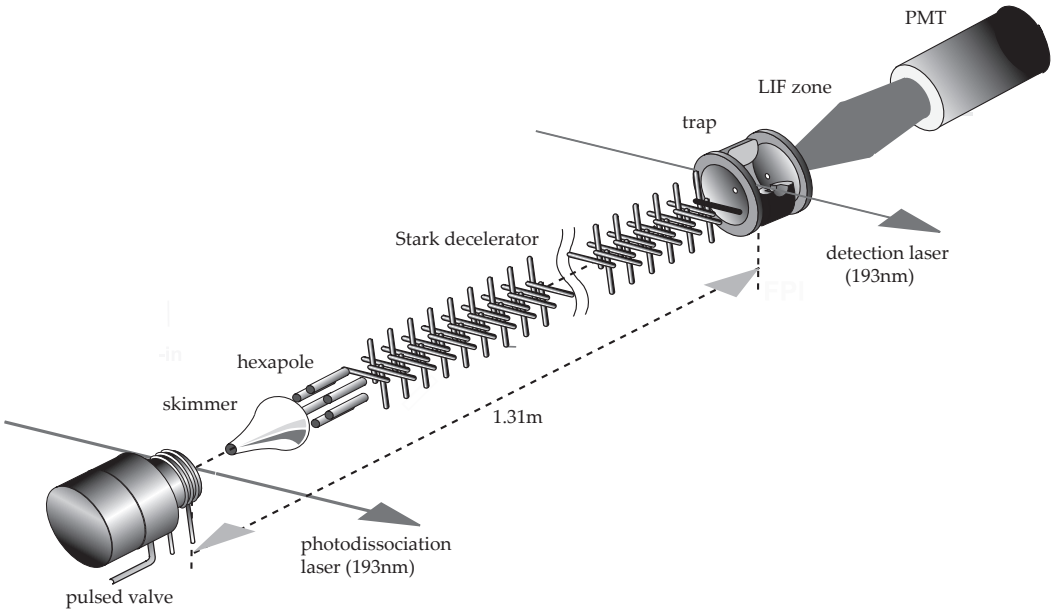

Figure 3.13: Schematic of the experimental setup in continuous wave time of flight measurements of OH-radicals.

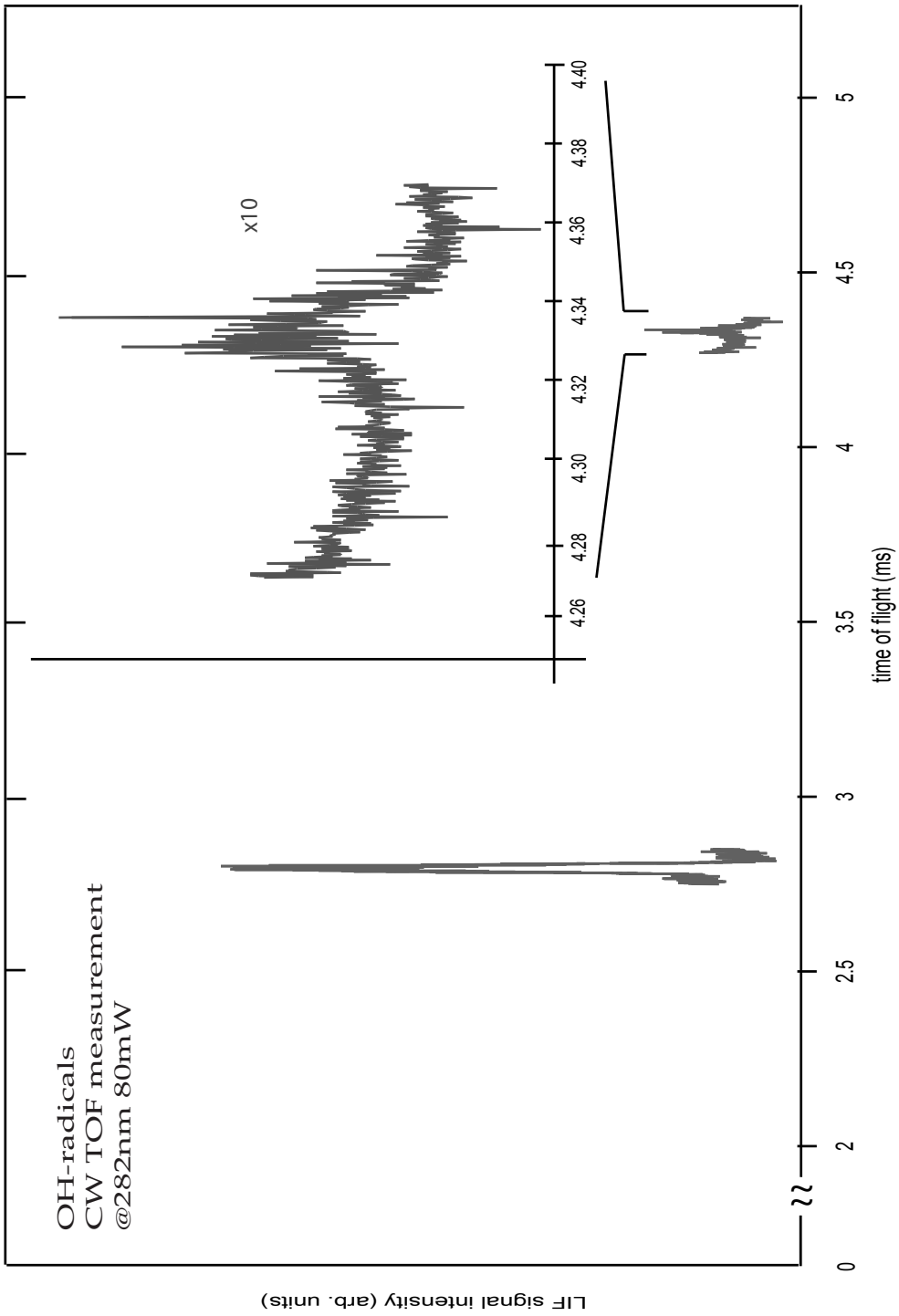

Figure 3.14: LIF intensity signal for continuous wave (cw) time of flight (TOF) measurements for fast and decelerated OH radicals.

Chapter 4

Sintesi in italiano

4.1 Introduzione

Negli ultimi decenni si è avuto un notevole progresso nel controllo del movimento delle particelle, cominciando dagli ioni per arrivare fino agli atomi e alle molecole. Questi studi sono stati promotori di importanti novità nella fisica atomica e molecolare, portando per esempio alla realizzazione di condensazioni Bose-Einstein e laser atomici. Allo stesso modo lo studio di molecole ultra-fredde, al quale collaborano di recente fisici e chimici, sembra promettere importanti passi in avanti nello studio della materia.

La spettroscopia ad alta risoluzione è una tecnica atta allo studio delle proprietà di molecole ultrafredde. Una tecnica comune per lo studio di molecole in stato gassoso è la spettroscopia LIF (laser-induced fluorescence). Le molecole vengono eccitate con radiazione visibile/ultravioletta e l'intensità della radiazione emessa viene misurata in funzione della frequenza di eccitazione. La quantità di informazione ottenibile in spettroscopia di livelli vibrazionali e rotazionali dipende dalla risoluzione disponibile.

Importanti innovazioni realizzate negli ultimi anni nella decelerazione e cattura di fasci molecolari [4] hanno permesso un aumento consistente della definizione negli spettri molecolari. Aumentando infatti il tempo di interazione tra i fasci molecolari e i dispositivi in cui avvengono le misure è aumentata la risoluzione ottenibile e di conseguenza la quantità di informazioni ricavabili.

Obbiettivo del lavoro di tesi qui presentato è la realizzazione di uno spettrometro laser ad alta risoluzione (1 MHz) da utilizzarsi in spettroscopia di molecole grandi e fredde. Particolare risalto è posto nella progettazione e implementazione dei dispositivi necessari per una calibrazione fine della frequenza. A questo sono destinati i due interferometri Fabry-Perot e la cella contenente gas iodico, costruiti e caratterizzati in questa tesi. Tali dispositivi devono lavorare sull'intervallo spettrale 500–750 nm su cui opera il sistema laser e garantire alta stabilità nel tempo e in temperatura. La misura accurata dei valori delle free spectral range per i due interferometri e il calcolo della precisione con cui questi valori sono stati misurati sono parti cruciali di questo lavoro, poichè da essi dipende l'accuratezza ottenibile in seguito nella calibrazione della frequenza in cui sono utilizzati.

4.2 Teoria: Interferometria e interferenza

Un interferometro è uno strumento basato sul concetto di interferenza tra onde luce coerenti che, a seconda della lunghezza del cammino ottico percorso, interferiscono in modalità diverse dando luogo a una figura di interferenza composta da picchi di intensità. La fase

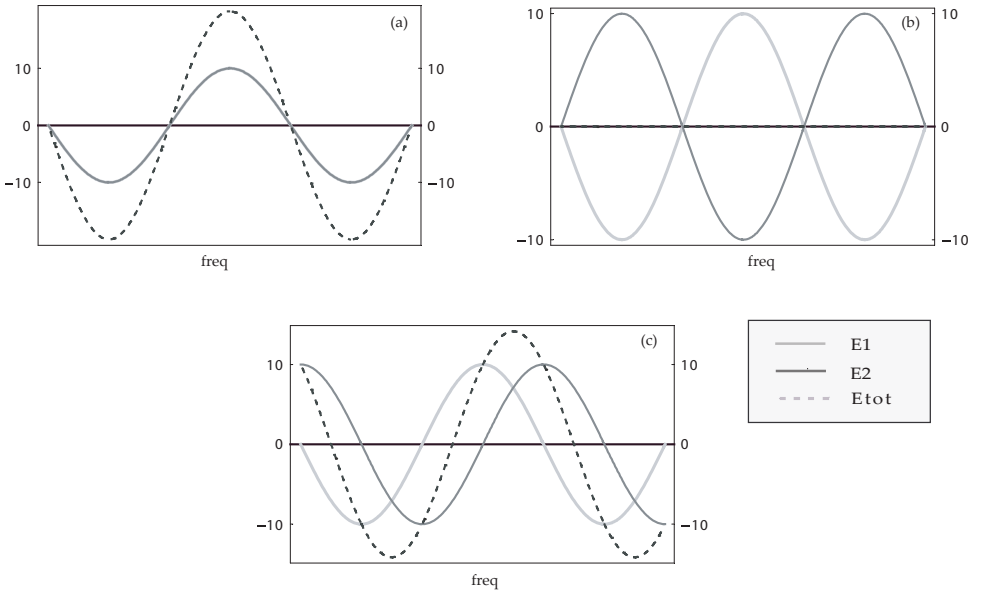

Figure 4.1: Interferenza di due onde coerenti (a)in fase, (b)fuori fase e (c) sfasate di $\frac{\pi}{2}$.

dell'onda dipende dal cammino ottico percorso, e le intensità si sommano in fase, dunque l'intensità dell'onda somma risultante dipende dalla loro differenza di fase. Di seguito e in figura 4.1 è mostrato l'esempio, semplice ma esemplificativo, di interferenza di due onde coerenti.

Un'onda piana può essere scritta come:

$$E(x,t) = E_0 \sin[\omega t - (kx + \varepsilon)] \qquad \alpha(x,\varepsilon) = -(kx + \varepsilon)$$
$$E(x,t) = E_0 \sin[\omega t + \alpha(x,\varepsilon)]$$

dove la dipendenza della fase α dal cammino ottico x è esplicitata. Due onde piane coerenti (emesse per esempio dalla stessa sorgente) che dopo aver percorso due diversi cammini x_1, x_2 raggiungono un rivelatore comune, hanno uguale frequenza ω ma diverse fasi α_1, α_2. La somma d'onda risultante avrá quindi uguale frequenza ω ma intensitá E_0 dipendente dalla differenza di fase al rivelatore $\alpha_2 - \alpha_1$:

$$E_1 = E_{01} \sin(\omega t + \alpha_1) \qquad E_2 = E_{02} \sin(\omega t + \alpha_2)$$
$$\Longrightarrow E_{tot} = E_1 + E_2 = E_0 \sin(\omega t + \alpha)$$

dove:

$$E_0^2 = E_{01}^2 + E_{02}^2 + 2E_{01}E_{02}\cos(\alpha_2 - \alpha_1)$$

$$\tan\alpha = \frac{\left(E_{01}\sin\alpha_1 + E_{02}\sin\alpha_2\right)}{\left(E_{01}\cos\alpha_1 + E_{02}\cos\alpha_2\right)}$$

Si rileverá quindi un massimo di intensitá quando le due onde arrivano in fase e un minimo quando arrivano fuori fase. L'alternarsi di massimi e minimi di intensità rilevato variando il cammino ottico di una delle due onde o variando la frequenza della luce sorgente, per esempio, è definito come la figura di interferenza prodotta al rivelatore da tali onde.

Questa semplice trattazione descrive bene il funzionamento di interferometri a doppia onda come l'interferometro di Michelson, ma deve essere opportunamente complicata per interferometri ad interferenza multipla come l'interferometro Fabry-Perot.

4.2.1 Interferometro Fabry-Perot

La struttura più semplice di un interferometro Fabry-Perot consiste in due superfici piane parallele altamente riflettenti. L'interferenza sfruttata è quella tra successive riflessioni di un raggio di luce all'interno della cavità (vedi figura 4.2). Sia ϕ lo sfasamento di un onda

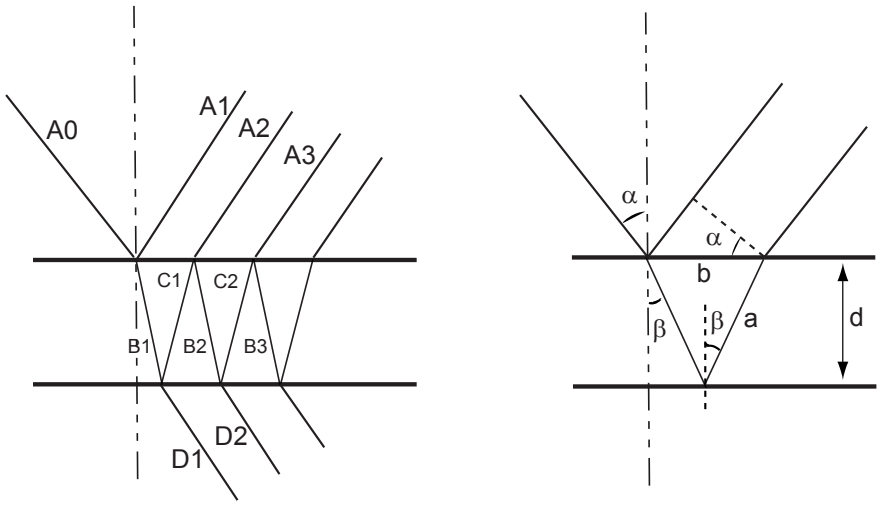

Figure 4.2: Interferenza di riflessioni tra superfici piane parallele ($\Delta s = 2na - b\sin\alpha$).

dopo aver attraversato due volte la cavità ed essere stata quindi riflessa una volta:

$$\phi = 2\pi\Delta s/\lambda + \Delta\Phi \tag{4.1}$$

dove $\Delta s = 2nd\cos\beta$, n l'indice di rifrazione, d la distanza tra le superfici e $\Delta\Phi = \pi$ il cambiamento di fase causato dalla riflessione. L'ampiezza totale A dell'onda riflessa dall'interferometro è la somma di tutte le ampiezze A_i considerati i loro sfasamenti [7, Chapter 4]:

$$\begin{aligned} A &= \sum_{m=1}^{p} A_m\, e^{i(m-1)\phi} = -\sqrt{R_{ef}}\, A_0 + \sqrt{R_{ef}}\, A_0\,(1-R_{ef})\, e^{i\phi} + \sum_{m=3}^{p} A_m\, e^{i(m-1)\phi} = \\ &= -\sqrt{R_{ef}} A_0 \left[1 - (1-R_{ef})\, e^{i\phi} \sum_{m=0}^{p-2} R_{ef}^m e^{im\phi}\right] \end{aligned} \tag{4.2}$$

dove R_{ef} è la riflettività delle superfici. Nel caso particolare di incidenza verticale ($\alpha = 0$) o di superfici infinitamente estese, il numero di riflessione è infinito e la serie geometrica in (4.2) diventa $(1 - R_{ef}e^{i\phi})^{-1}$. L'ampiezza A assume quindi la più semplice espressione:

$$A = -\sqrt{R_{ef}}\, A_0\, \frac{1 - e^{i\phi}}{1 - R_{ef}e^{i\phi}} \tag{4.3}$$

Il prodotto di A per il suo complesso coniugato A^* è l'intesnità dell'onda riflessa, funzione, in questo caso, dello sfasamento ϕ:

$$I_R = I_0 R_{ef} \frac{4\sin^2(\phi/2)}{(1-R_{ef})^2 + 4R_{ef}\sin^2(\phi/2)} \tag{4.4}$$

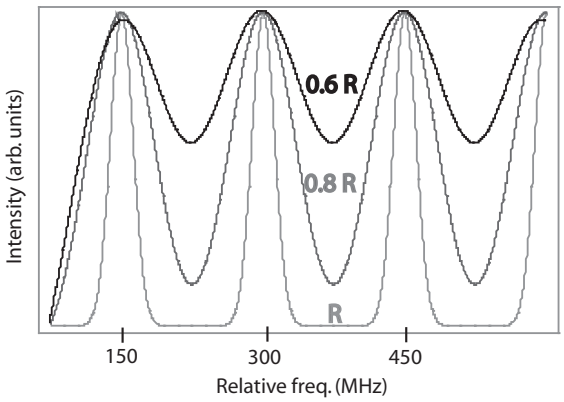

Figure 4.3: Figura di interferenza di un interferometro Fabry-Perot: intensità trasmessa in funzione della frequenza ν per diversi valori della riflettività degli specchi R_{ef}: R_{ef}, $0.6R_{ef}$, $0.8R_{ef}$. Simulazione con FSR=150 MHz e R=0.80)

Nello stesso modo si trova anche l'espressione dell'intensità dell'onda trasmessa:

$$I_T = I_0 \frac{(1-R_{ef})^2}{(1-R_{ef})^2 + 4R_{ef}\sin^2(\phi/2)} \tag{4.5}$$

Queste due espressioni, note come formule di Airy, rappresentano l'intensità (riflessa e trasmessa) in funzione della frequenza o della differenza di cammino ottico, in una figura di interferenza di un interferometro Fabry-Perot. In figura 4.3 ne è mostrato un esempio.

Definiamo i seguenti parametri caratteristici di una figura di interferenza:

$$\text{Finesse} \quad \rightarrow \quad F^* := \frac{\pi\sqrt{R_{ef}}}{1-R_{ef}} \tag{4.6}$$

$$\text{Free Spectral Range} \quad \rightarrow \quad FSR = \delta\nu := \frac{c}{\Delta s} \tag{4.7}$$

$$\text{Full Width at Half Maximum} \quad \rightarrow \quad FWHM = \Delta\nu := \delta\nu/F^* \tag{4.8}$$

FSR rappresenta la distanza in frequenza tra due massimi di intensità successivi e FWHM la larghezza in frequenza a media altezza di un singolo picco. Finesse è un indice della qualità dell'interferometro ed è direttamente dipendente dalla riflettività degli specchi. Ricordando che $\Delta s = 2nd\cos\beta$ e assumendo la luce incidente con angolo perfettamente verticale ($\alpha = 0$), possiamo ottenere la nota espressione della FSR per un interferometro Fabry-Perot (piano):

$$|\delta\nu|_{\alpha=0} = \frac{c}{2nd} \tag{4.9}$$

4.2.2 Interferometro Fabry-Perot a specchi concavi

Ancora più interessante risulta l'interferometro Fabry-Perot a specchi concavi, in particolare nella vantaggiosa configurazione confocale.

Due sono le trattazioni prese in considerazione in questo lavoro di tesi: in primo luogo una descrizione della distribuzione spaziale del campo elettromagnetico di un'onda all'interno di una cavità risonante a specchi concavi nella direzione perpendicolare a quella di propagazione dell'onda (*transverse electromagnetic modes*)[7, Chapter 4]. Successivamente calcoli di geometria e ottica (ray tracing calculations) permettono di seguire la

traccia di un raggio all'interno di una cavità simmetrica non confocale e di analizzare in dettaglio la confocalità vista come caso particolare [9].

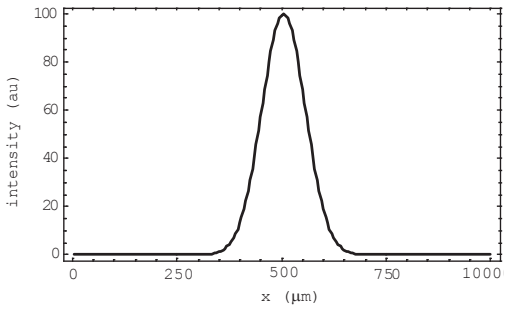

Figure 4.4: Distribuzione dell'intensità I_{00} del modo fondamentale TEM_{00} nelle direzioni (x,y) perpendicolari a quella di propagazione (simulazione $\lambda = 500\,\text{nm}$, $R = 500\,\text{mm}$ in z=0).

Partendo dalla complicata espressione di distribuzione spaziale di ampiezza di un'onda stazionaria all'interno di una cavità simmetrica confocale a specchi concavi

$$A_{mn}(x,y,z) = C^* H_m(x^*) H_n(y^*) \exp(-r^2/w^2) \exp[-i\phi(z,r,R)] \tag{4.10}$$

in cui sono esplicitati modi di ordine superiore m, n e dove C^* è una costante di normalizzazione, H_m il poliniomio di Hermite di ordine m-esimo e w una misura radiale dell'intensità

$$w^2(z) = \frac{\lambda d}{2\pi}[1 + (2z/d)^2] \tag{4.11}$$

è possibile ricavare la più semplice espressione della distribuzione spaziale dell'intensità all'interno della cavità per il modo fondamentale ($m = 0, n = 0$):

$$I_{00}(x,y,z) \propto A_{00} A_{00}^* = I_0 e^{-\frac{2(x^2+y^2)}{w^2}} \tag{4.12}$$

La distribuzione nelle direzioni perpendicolari a quella di propagazione z (vedi figura 4.4) ha una forma gaussiana. Definiamo quindi *raggio di un fascio d'onda* come la metà della larghezza di tale gaussiana all'altezza in cui l'intesnità è $1/e^2$ del suo valore massimo.

Interessante è anche il grafico di $w(z)$ lungo l'asse z di propagazione mostrato in figura 4.5. L'intensità del fascio risulta maggiormente concentrata attorno all'asse z nel centro della cavità ($z = 0$ nel nostro caso) misurando un raggio di $200\,\mu$m e più diffusa agli specchi dove il raggio risulta essere $300\,\mu$m. Entrambi questi valori sono stati calcolati per una cavità confocale con $L = R = 500\,\text{mm}$ e un fascio di luce coerente di $\lambda = 500\,\text{nm}$.

Considerando modi di ordine superiore al fondamentale, le distribuzioni dell'intensità all'interno della cavità si complicano e un esempio di quello che succede è mostrato in figura 4.6 dove sono riportati i grafici per TEM_{00} e TEM_{10} nelle tre coordinate (x, y, z). Si osserva subito che TEM_{10} ha un minimo di intensità al centro ($z = 0$) dove invece TEM_{00} aveva un massimo. Vedremo in seguito come e quando queste differenze nelle distribuzioni delle intensità alterino o meno le relative figure di interferenza trasmesse. Per ora ci limitiamo a osservare che il raggio di un fascio, come definito precedentemente,

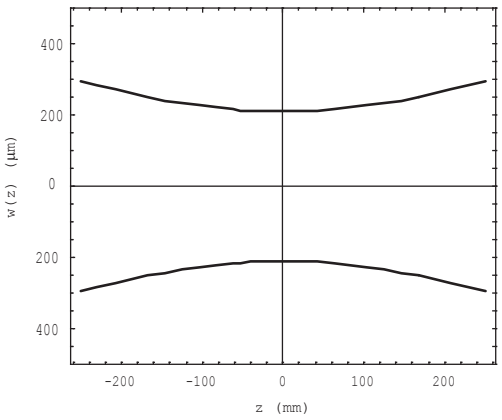

Figure 4.5: Grafico di w(z) lungo l'asse di propagazione z (simulazione $\lambda = 500\,\mathrm{nm}$, $R = 500\,\mathrm{mm}$). Il raggio del fascio misura $200\,\mu$m al centro della cavità e $300\,\mu$m agli specchi.

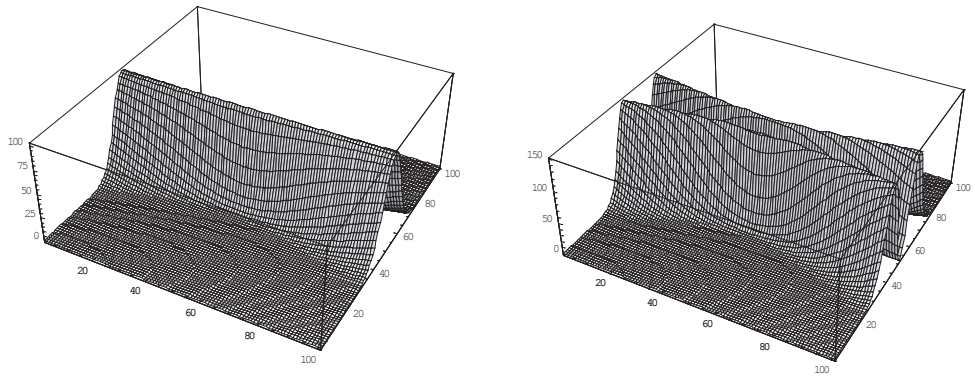

Figure 4.6: Distribuzione spaziale dell'intensità all'interno di una cavità risonante simmetrica confocale per TEM_{00} e TEM_{10}

si allarga considerando modi di ordine superiore.

Come accennato a inizio sezione, la seconda trattazione dell'interferometro Fabry-Perot a specchi concavi considerata in questo lavoro riguarda un calcolo geometrico/ottico che permette di seguire la traccia di un fascio a cui sono associati inizialmente gli angoli θ_0 e φ_0 (determinano l'angolo e il punto di incidenza) dopo successive riflessioni all'interno di una cavità simmetrica a specchi concavi non confocale [9] (vedi figura 4.7). Le espressioni che si trovano per φ_p e θ_p, coordinate del fascio dopo p riflessioni, in funzione di θ_0 e φ_0 già semplificate per il caso confocale $d = R$ sono:

$$\varphi_p = (\,\varphi_0 + \theta_0\,)\sin(p\,\pi/2) - \varphi_0 \sin[\,(p-1)\pi/2\,] \tag{4.13}$$

$$\theta_p = -(\,\theta_0 + 2\varphi_0\,)\sin(p\,\pi/2) - \theta_0 \sin[\,(p-1)\pi/2\,] \tag{4.14}$$

Da queste segue subito un primo importante risultato:

$$\varphi_{p+4} = \varphi_p$$

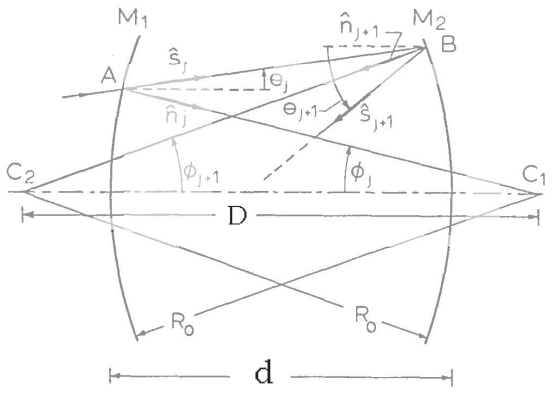

Figure 4.7: Geometria di una cavità simmetrica a specchi concavi non confocale (figura presa da [9])

$$\theta_{p+4} = \theta_p$$

cioè che indipendentemente da angolo e punto di incidenza, in una cavità *confocale* un fascio dopo quattro riflessioni torna esattamente allo stesso punto.

Nello stesso modo si ottiene l'espressione della lunghezza del cammino ottico del fascio dopo aver attraversato quattro volte la cavità:

$$L = 4r + (4 + 2{\theta_0}^2 + 4\theta_0\,\varphi_0)(d - R) \tag{4.15}$$

Ecco dunque un secondo importante risultato: solo nel caso confocale $d = R$ la lunghezza del cammino L non dipende dal punto e dall'angolo di incidenza del fascio. Questi due grandi vantaggi della configurazione confocale ne motivano il suo vasto utilizzo.

L'espressione della free spectra range (FSR) di un interferometro Fabry-Perot confocale con specchi concavi distanti d

$$\delta\nu = \frac{c}{4nd} \tag{4.16}$$

risulta ora chiara.

4.2.3 Simulazioni delle figure di interferenza

In questa sezione sono riportate le simulazioni delle figure di interferenza per l'interferometro confocale eseguite con Mathematica (programma di simulazione). Obbiettivo principale è mostrare un ulteriore vantaggio di tale configurazione risultante dalla particolare degenerazione dei modi superiori.

In figura 4.8 sono mostrati i picchi di interferenza trasmessi da un interferometro Fabry-Perot simmetrico, illuminato da radiazione coerente, nelle tre diverse configurazioni: quasi-piana (raggio di curvatura quasi infinito), confocale perfetta $L = R$, quasi-concentrica $L = 2R$. In tali simulazioni sono stati considerati anche i modi di ordine superiore (fino al decimo ordine, vedi figura 4.9). La particolare sovrapposizione altamente degenere del caso confocale risultante in picchi di intensità massima rispetto qualsiasi altra configurazione e avente FSR dimezzata rispetto al caso piano perfetto, è evidente in figura.

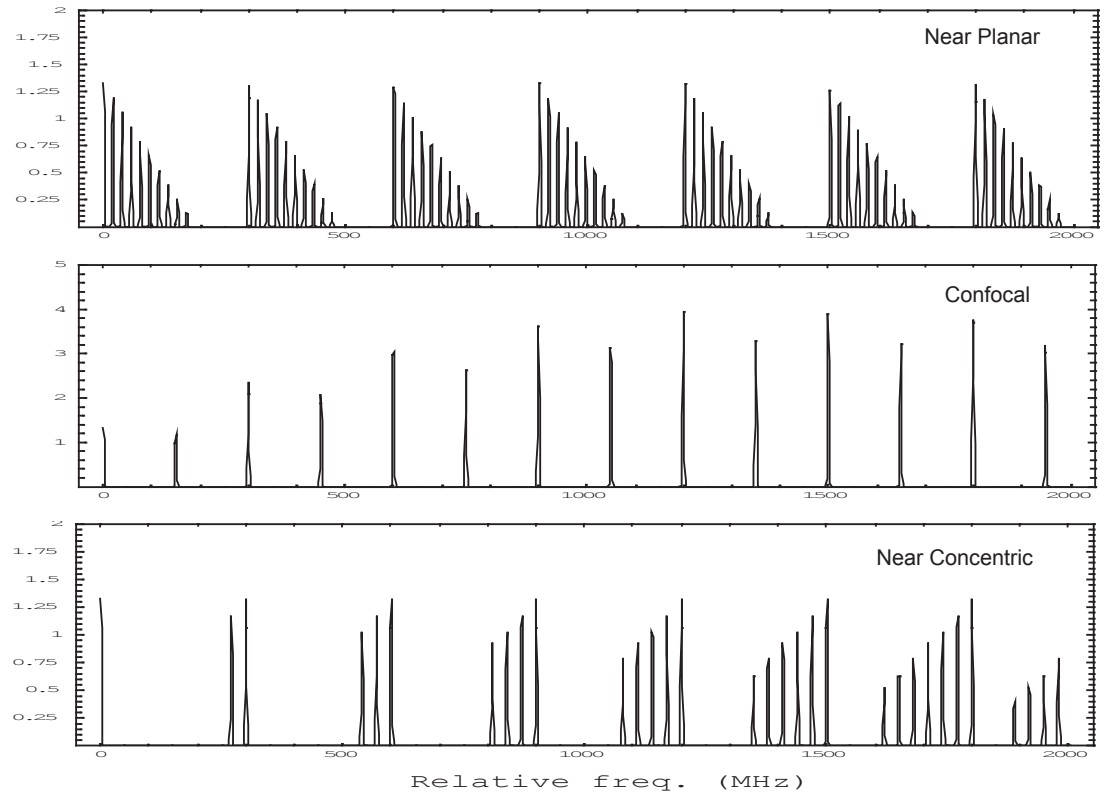

Figure 4.8: Simulazione dei picchi d'interfernza per un interferometro simmetrico piano, confocale e concentrico in cui sono considerati i modi trasversali superiori.

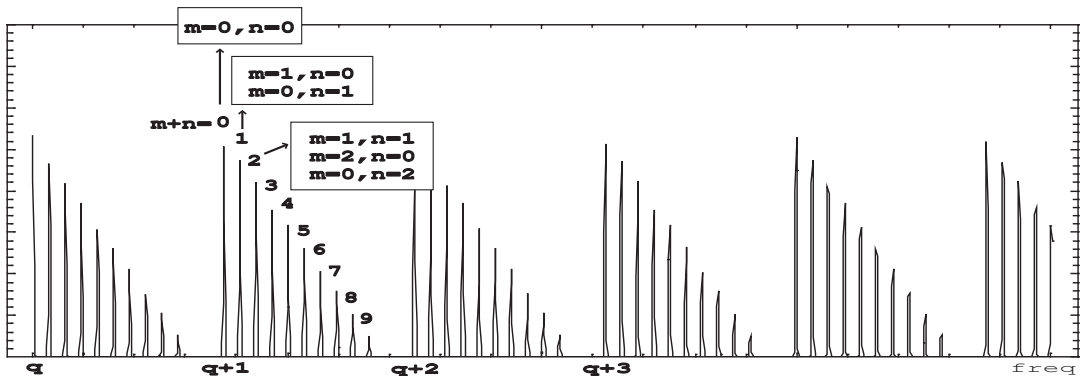

Figure 4.9: Distribuzione dei modi superiori (m,n) in una figura di interferenza (simulazione eseguita con $L = 400\,\text{mm}$ e $R = 3000\,\text{mm}$).

4.3 Apparato sperimentale

In figura 4.10 è mostrato lo schema del sistema laser implementato in questo lavoro di tesi. Il sistema consiste in un laser Ar^+-ion (*Coherent Innova Sabre*), un laser ring dye

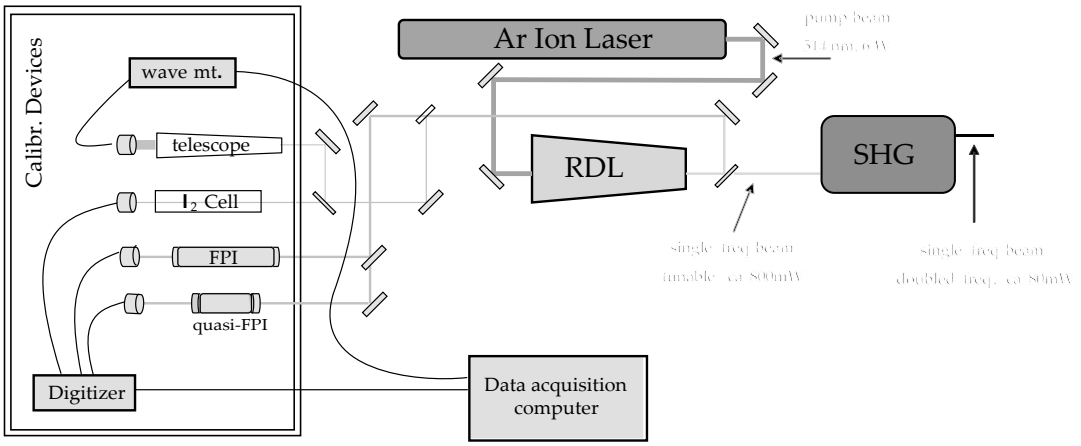

Figure 4.10: Schema del sistema laser

(*Coherent 899-21*), un generatore di seconda armonica (*LAS wave train*) e dei componenti ottici per la calibrazione.

4.3.1 Laser e generatore di seconda armonica

Circa 6.5 W di radiazione a 514 nm (laser Ar^+-ion) pompano la sostanza dye (Rhodamine 110) situata all'interno di una cavitá ring opportunamente accessoriata, generando in questo modo tipicamente 800 mW di radiazione attorno ai 550 nm con larghezza di riga inferiore al MHz. Una larghezza di riga cosí stretta rappresenta una caratteristica fondamentale di questo sistema laser considerato il fatto che dovrà essere utilizzato in spettroscopia ad alta risoluzione di molecole fredde ($\sim$mK) aventi righe spettrali particolarmente strette ($\sim$10 MHz).

La frequenza è attivamente stabilizzata tramite l'utilizzo di componenti ottico/elettronici i quali generano e gestiscono un segnale di feedback utilizzato per variare (di pochissimo e in continuazione) la lunghezza della cavità ogni qualvolta la frequenza si muova da un valore preso come riferimento. Variando la lunghezza del cammino ottico della cavità e mantenendo la frequenza del laser attivamente stabilizzata, sono possibili scansioni di 30 GHz a diverse velocitá di scansione (partendo da 30 GHz/s).

La luce laser a frequenza singola cosí generata viene poi diretta in un generatore di seconda armonica dove, per mezzo di un cristallo ottico non lineare inserito in una cavitá ring, se ne raddoppia la frequenza. Circa 135 mW di luce continua ultravioletta alla lunghezza d'onda di 273 nm sono stati cosí prodotti nei nostri esperimenti.

4.3.2 Componenti per la calibrazione

Ruolo fondamentale in questo lavoro hanno il progetto e la costruzione dei dispositivi per la calibrazione fine della frequenza. Essi consistono in un wave meter, una cella contenente gas iodico e due interferometri Fabry-Perot con specchi concavi verso i quali viene diretta

una piccola parte della luce uscente dal laser ring dye. L'intensità di luce trasmessa dai due interferometri e dalla cella iodica è misurata via fotodiodo simultaneamente per i tre componenti durante una scansione del laser e i segnali così generati vengono digitalizzati e registrati in un computer.

Il wave meter fornisce una lettura assoluta della frequenza della luce laser con un'accuratezza di 700 MHz. Riconoscendo le linee misurate dello spettro di assorbimento dello iodio su spettri tabulati è possibile risalire ad un valore della frequenza con una precisione di circa 200 MHz. I picchi delle figure di interferenza dei due interferometri, misurati anch'essi durante una scansione del laser, forniscono una misura relativa della frequenza tra due linee spettrali dello iodio. Interpolando più di 100 picchi distanziati 150 MHz circa l'uno dall'altro è possibile raggiungere un'accuratezza di circa 0.1 MHz nella calibrazione.

Uno dei due interferometri Fabry-Perot è utilizzato in configurazione confocale per produrre picchi aventi FSR di circa 150 MHz ed è stato progettato per lavorare nell'intervallo spettrale 500-750 nm. Altra caratteristica importante è la stabilità della FSR: il valore effettivo è stato misurato con precisione una volta montato e testato l'interferometro, ma fondamentale per una buona calibrazione della frequenza è che questo valore rimanga stabile nel tempo e per variazioni della temperatura dell'ordine del Kelvin (essendo la temperatura sul tavolo ottico attivamente stabilizzata con precisione 1 K). Struttura dell'interferometro è quindi un tubo di *Zerodure* (coefficiente di espansione termica $0\pm\ 0.05\ 10^{-6}K^{-1}$) lungo 499.95 ± 0.05 mm forato nel mezzo lungo tutta la lunghezza su cui sono montati due specchi di raggio di curvatura 500 mm. La lunghezza del tubo è stata scelta in modo tale che i vertici degli specchi fossero effettivamente distanti $L = R = 500mm$ (confocale).

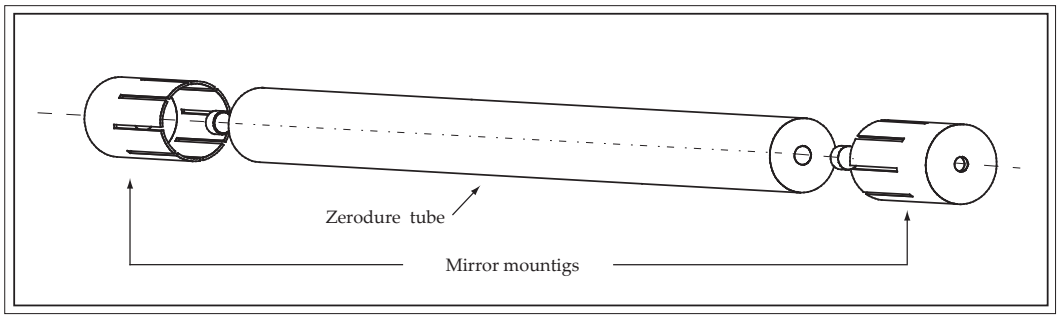

Figure 4.11: Schema dell'interferometro Fabry-Perot confocale

Gli specchi, montati sul tubo utilizzando due cappucci cilindrici d'acciaio inossidabile appositamente costruiti nel workshop interno (vedi figure 4.11 e 4.12), sono continuamente spinti contro le facce del tubo da due molle. Le molle sono state pensate per reagire alle possibili espansioni o riduzioni dei due cappucci dovute a variazioni della temperatura. Questo garantisce che la distanza L tra i due specchi vari non più di 25 nm/K e di conseguenza la FSR di 7.5 Hz/K. Gli specchi (*Laser Optik Garbsen*) hanno un rivestimento interno altamente riflessivo ($99.5\pm0.1\%$) garantito per l'intervallo di lunghezze d'onda 500-750 nm. Di coseguenza la Finesse dell'interferometro è attesa attorno a 600 e la larghezza a media altezza dei picchi $\Delta\nu$ circa 0.25 MHz. In realtà dispersioni della cavità dovute a diffrazione o assorbimento contribuiscono a diminuire l'effettiva Finesse, dunque ci si attende picchi più larghi di 0.25 MHz.

Alcuni calcoli sono stati eseguiti in Mathematica per simulare i picchi di interferenza

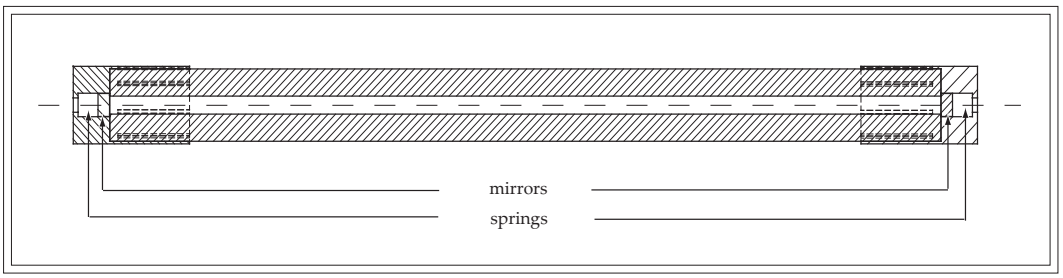

Figure 4.12: Disegno tecnico dell'interferometro Fabry-Perot confocale

nel caso confocale perfetto e nel "worste case". Il "worste case", o caso peggiore, è quello in cui si considerano i valori di L ed R con le loro tolleranze massime garantite dai costruttori (0.05 mm per L e 0.1 mm per R). Le simulazioni dei due casi, eseguite focalizzando

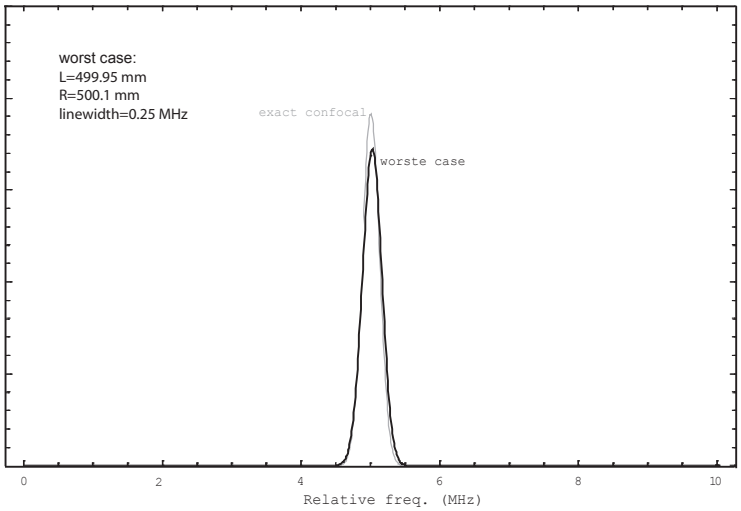

Figure 4.13: Comparazione tra figura di interferenza del caso confocale perfetto (grigio) e caso confocale considerate le tolleranze su L e R

l'attenzione su un solo picco, sono riportate nello stesso grafico in figura 4.13. Anche nel caso peggiore non si osservano modi di ordine superiore spaiati su uno dei due lati del picco ma l'intensità risulta ridotta del 10% circa. Le imprecisioni di costruzione non dovrebbero quindi influenzare sensibilmente la qualità della figura di interferenza.

L'altro interferometro Fabry-Perot progettato e costruito in questo lavoro viene utilizzato in configurazione quasi-confocale. L'idea è quella di utilizzare una sovrapposizione dei modi trasversali diversa da quella del caso confocale (in cui la degenerazione è massima e l'intensità dei picchi massimizzata) risultante in picchi d'interferenza ancora più ravvicinati rispetto al caso confocale [6]. Aggiustando infatti la distanza L fra gli specchi (cavità simmetrica) a valori prossimi a R ma non esattamente uguali, è possibile generare una figura d'interferenza con

$$FSR = \frac{c}{2LN} \tag{4.17}$$

dove N è un intero maggiore di 1 ($N = 2$ nel caso confocale). Questo significa che è possibile ottenere una FSR di circa 50 MHz con un interferometro lungo 10 cm. Ovviamente l'intesità di tali picchi è molto inferiore rispetto al caso confocale e decresce linearmente con N. Si è voluto quindi costruire questo secondo interferometro utilizzando una struttura del tutto simile a quella del confocale ma con la distanza L tra gli specchi calibrabile in fase di assemblaggio, in modo da poter scegliere la miglior sovrapposizione in termini di FSR e intensità dei picchi al tempo stesso.

Nelle figure 4.14 e 4.15 sono riportati lo schema e il disegno tecnico di questo interferometro che chiamiamo quasi-confocale.

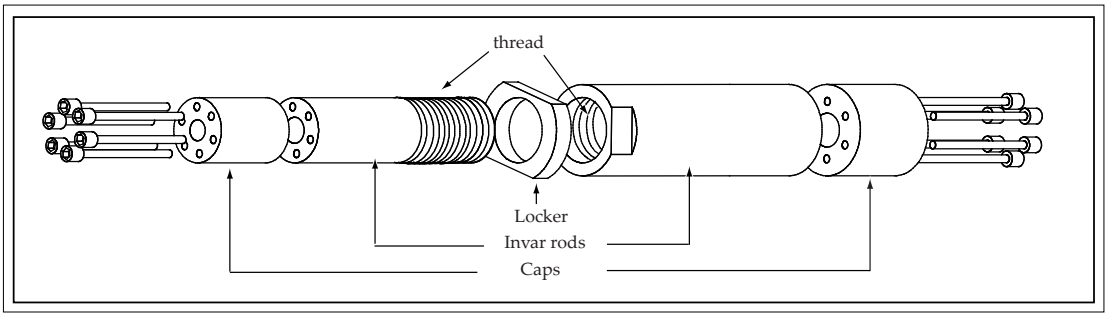

Figure 4.14: Schema dell'interferometro Fabry-Perot quasi-confocale.

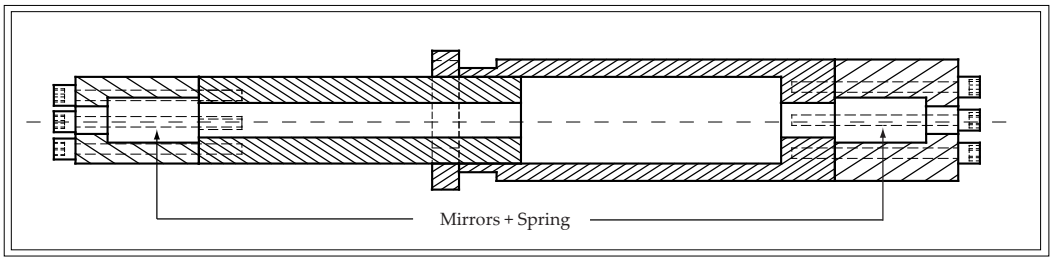

Figure 4.15: Disegno tecnico dell'interferometro Fabry-Perot quasi-confocale.

Il materiale utilizzato è *Invar 36* (coefficiente di espansione termico $1.7{-}2.0\ 10^{-6}\,K^{-1}$), una lega di nichel e ferro. I cappucci con cui vengono montati gli specchi sono sempre di acciaio inossidabile e due molle sono utilizzate anche in questo caso per mantenere gli specchi a contatto con la struttura principale. Volendo calibrare L a posteriori è stata scelta come struttura principale non un tubo unico ma due metà separate avvitate assieme. Avvitando o svitando le due metà una con l'altra (filetto M22x0.75) è possibile variare L con una precisione di circa 5 μm.

Gli specchi, raggio di curvatura 100 mm, hanno lo stesso rivestimento altamente riflettente di quelli dell'interferometro confocale. Tuttavia il valore atteso della Finesse è in questo caso circa 30 ($\pi\sqrt{R}/(1-R)\cdot 1/N$), ridotto di N volte rispetto al caso confocale. La minima larghezza a mezza altezza attesa dei picchi è 1.6 MHz. Considerato il materiale utilizzato, ci si aspetta una variazione della FSR con la temperatura inferiore ai 100 Hz/K.

Lo stesso programma sviluppato per simulare la figura di interferenza dell'interferometro confocale nello studio delle possibili deviazioni dal caso confocale perfetto, è stato utilizzato in questo caso per prevedere a che distanza L aspettarsi una buona sovrapposizione

dei picchi risultante in una FSR di circa 50 MHz. I risultati della simulazione sono riportati in figura 4.16 e il valore L trovato è di circa L=105.54 mm.

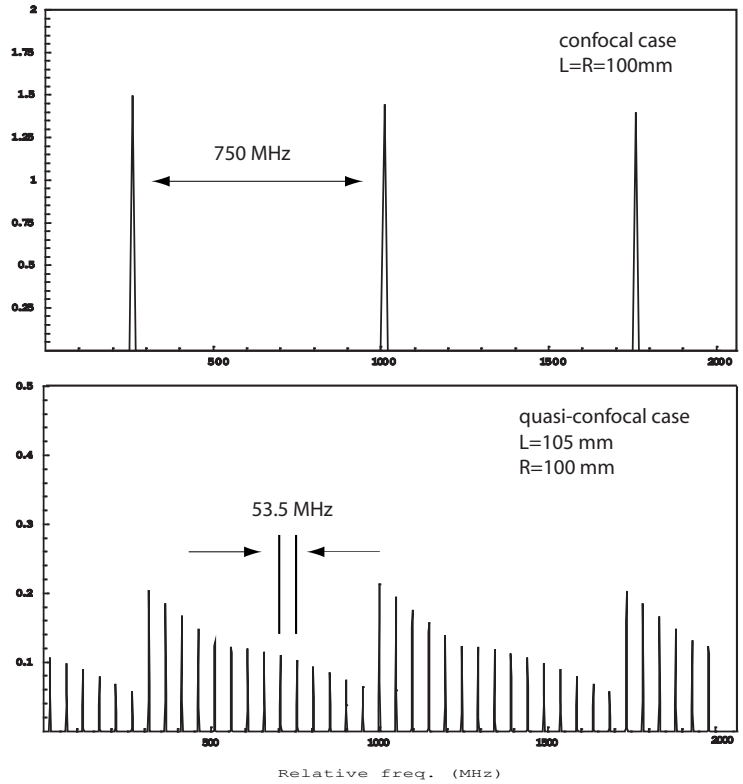

Figure 4.16: Simulazione della figura di interferenza dell'interferomtero quasi-confocale risultante in una FSR di circa 50 MHz. La sovrapposizione dei modi trasversali sfruttata in questo caso è diversa da quella confocale e risulta in una più stretta FSR

La cella contenente gas iodico è stata costruita secondo le specifiche riportate in figura 4.17. L'angolo di 34 ° (*angolo di Brewster*) tra tubo e finestre è stato scelto per minimizzare le riflessioni del raggio di luce incidente.

Iodio in stato gassoso dentro la cella è stato ottenuto inserendo alcuni cristalli di iodio e creando una depressione all'interno pari alla pressione di sublimazione dello iodio a temperatura ambiente ($\sim$0.4 mbar).

La cella è stata testata misurando le linee dello spettro di assorbimento dello iodio nell'intervallo spettrale 17730-17732 cm^{-1}.

4.4 Risultati

In questa sezione sono descritte le misure eseguite con lo scopo di ottenere i valori delle free spectral range dei due interferometri, confocale e quasi-confocale. La regione nell'intervallo spettrale 17883–18455 cm^{-1} è stata analizzata e 14 scanzioni, ognuna di circa 1 cm^{-1}, sono state eseguite in questa regione. Il sistema laser utilizzato, descritto in dettaglio nella sezione precedente, consiste in questo caso di laser Ar^+-ion, laser ring dye e dispositivi per la calibrazione. La potenza della radiazione utilizzata in queste misure è stata di

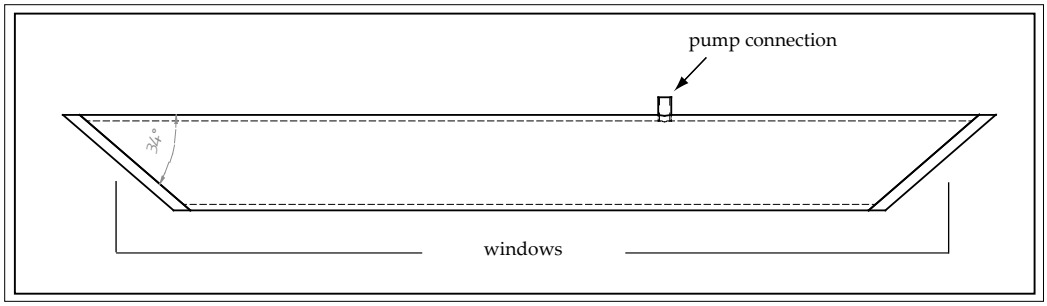

Figure 4.17: Disegno tecnico della cella iodica

50–230 mW.

La luce prodotta viene diretta verso i due interferometri e la cella iodica e, dopo accurato allineamento, l'intensità di luce trasmessa attraverso i tre dispositivi viene misurata via fotodiodo simultaneamente. I tre segnali voltaici provenienti dai fotodiodi (spettro di assorbimento dello iodio, intensità trasmessa attraverso i due interferometri) vengono digitalizzati da un sistema ricezione dati durante le scansioni del laser e salvati poi in un computer. La frequenza di sampling è di 100 Hz e le scansioni sono eseguite a $\sim$0.1 cm^{-1}/min.

Grafici simili a quello mostrato in figura 4.18 sono stati ottenuti graficando i segnali digitalizzati salvati sul computer. Nota la frequenza delle linee dello spettro di assorbimento dello iodio da spettri tabulati, è possibile risalire ad una prima stima del valore delle FSR per i due interferometri dividendo la distanza in frequenza tra due linee per il numero di picchi compresi tra esse. Un altro metodo consiste nell'assegnare a ciascuna linea dello iodio un corrispondente picco degli spettri di interferenza e graficare la frequenza delle linee in funzione del numero assegnato ai picchi partendo da uno scelto come riferimento. La pendenza della retta che interpola al meglio tali punti fornisce il valore della FSR valutata sui punti considerati.

Con lo scopo di migliorare l'accuratezza sul valore di FSR, tutte le misure sono state considerate insieme e un unico grafico riguardante l'intero intervallo spettrale analizzato è stato plottato, vedi figura 3.4. La deviazione standard risultante dall'interpolazione diminuisce infatti col numero dei punti considerati. Per fare questo si è dovuto prevedere il numero di picchi negli intervalli spettrali compresi tra due misurazioni. Dettagli sull'analisi dei dati ed esplicitazioni sull'accuratezza di tali previsioni si possono trovare nella sezione 3.1.

I valori delle FSR e le loro accuratezze risultanti dalle analisi delle misure sono:

Interferometro confocale:
FSR= $(149.948667 \pm 0.000218)$ MHz

Interferometro quasi-confocale:
FSR= (49.543 ± 0.00867) MHz

Il sistema nel suo complesso non è ancora stato applicato in spettroscopia, ma un esperimento in cui i componenti laser (senza dispositivi per la calibrazione) sono stati utilizzati per misurazioni di tempo di volo di radicali OH veloci e decelerati è stato eseguito e una completa descrizione la si può trovare nella sezione 3.3. In questa parte della tesi si

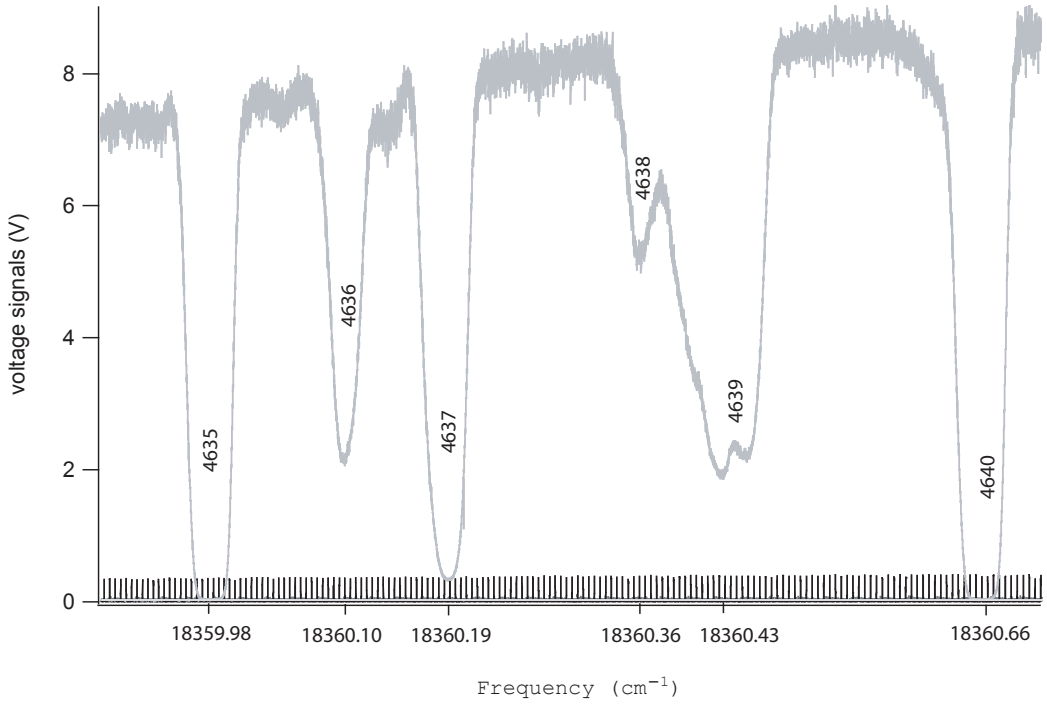

Figure 4.18: Tracce dei segnali misurati: linee di assorbimento dello iodio (picchi grandi negativi in grigio scuro), intensità trasmessa dall'interferometro confocale (picchi positivi di altezza circa 0.5 V) e da quello quasi-confocale (picchi positivi di altezza circa 0.1 V). I numeri delle linee spettrali dello iodio come riportati su [8] sono segnati.

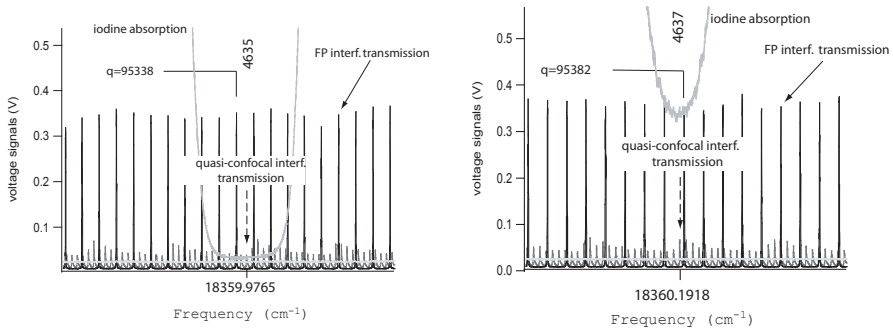

Figure 4.19: Ingrandimento di figura 4.18 attorno a due linee spettrali: il numero q assegnato ai picchi dell'interferometro confocale è indicato. I numeri q assegnati ai picchi di tutte le misurazioni da noi eseguite sono riportati in Appendice A.

trova anche una descrizione della tecnica sviluppata e utilizzata nei nostri laboratori per decelerare jet di espansioni molecolari per mezzo di campi elettrici varianti nel tempo.

4.5 Conclusioni

Il lavoro di ricerca descritto in questa tesi é stato svolto presso il dipartimento di Fisica Molecolare del Fritz-Haber-Institut der Max-Planck-Gesellschaft a Berlino durante l'anno solare 2004. Obbiettivo è la realizzazione di uno spettrometro laser ad alta risoluzione (1 MHz) da utilizzarsi in spettroscopia di molecole grandi e fredde.

Una moderna tecnica basata sull'effetto Stark, cui é soggetta una molecola in un campo elettrico, viene utilizzata in laboratorio per decelerare (raffreddare) e catturare fasci di espansioni molecolari supersoniche. Intensi campi elettrici varianti nel tempo lungo il cammino ne diminuiscono l'energia cinetica traslazionale a spese dell'energia potenziale interna. Fasci molecolari di radicali OH sono stati recentemente decelerati con questa tecnica da 428 m/s a 21 m/s e catturati (circa 10^5 molecole in un volume di 0.03 cm^3). La ragione principale cui si deve l'utilizzo di tale tecnica é il notevole incremento in risoluzione ottenibile negli spettri molecolari di molecole decelerate (fredde). Il nostro obiettivo é dunque quello di studiare molecole piú complesse, sempre piú in dettaglio.

In questo lavoro é stato progettato, implementato e testato un sistema laser generante luce continua a fine riga spettrale nell'intervallo visibile/ultravioletto e calibrabile in frequenza con alta precisione, da utilizzarsi in tale spettroscopia ad alta risoluzione. Il sistema consiste in un laser Ar^+-ion (*Coherent Innova Sabre*), un laser ring dye (*Coherent 899-21*), un generatore di seconda armonica (*LAS wave train*) e componenti ottici per la calibrazione. Circa 6.5 W di radiazione a 514 nm (laser Ar^+-ion) pompano la sostanza dye (Rhodamine 110) situata all'interno di una cavitá ring opportunamente accessoriata, generando in questo modo tipicamente 800 mW di radiazione attorno ai 550 nm con larghezza di riga inferiore al MHz. Tale lunghezza d'onda puó essere variata con continuitá in un intervallo di circa 50 nm attorno al valore di massimo, variando la lunghezza del cammino della luce all'interno della cavitá. La frequenza viene attivamente stabilizzata tramite l'utilizzo di componenti ottico/elettronici; scansioni di 30 GHz attorno al valore in cui si attiva tale controllo sono possibili a diverse velocitá di scansione (da 30 GHz/s a 3 GHz/min). La luce laser a frequenza singola cosí generata viene poi diretta in un generatore di seconda armonica dove, per mezzo di un cristallo ottico non lineare inserito in una cavitá ring, se ne raddoppia la frequenza. Circa 135 mW di luce continua ultravioletta alla lunghezza d'onda di 273 nm sono stati cosí prodotti nei nostri esperimenti.

Parte fondamentale in questo lavoro hanno avuto il progetto e la costruzione dei dispositivi per la calibrazione fine della frequenza. Essi consistono in una cella contenente gas iodico e due interferometri Fabry-Perot con specchi concavi verso i quali viene diretta una piccola parte della luce uscente dal laser ring dye. Le linee dello spettro di assorbimento dello iodio e i picchi di interferenza dei due interferometri misurati via fotodiodo durante una scansione del laser sono, rispettivamente, una misura assoluta e relativa della frequenza.

Nota la frequenza delle linee di assorbimento dello iodio da spettri tabulati, si risale ad un valore assoluto della frequenza. Analizzando poi regioni piú piccole comprese tra due linee spettrali, si possono misurare variazioni relative della frequenza grazie alle due scale ad alta risoluzione fornite dalle figure di interferenza dei due interferometri. Essi generano rispettivamente picchi con *free spectral range* (FSR) 149.944 MHz (interferometro Fabry-Perot confocale con specchi concavi distanziati da 500 mm) e 49.250 MHz (interfe-

rometro con specchi concavi di raggio di curvatura 100 mm distanziati da 105.56 mm, in configurazione quasi-confocale).

In fase di progettazione é stato sviluppato e utilizzato un codice in linguaggio *Mathematica* per la simulazione delle figure di interferenza dei due interferometri, atto a studiarne in particolare la qualitá e stabilitá in funzione delle loro caratteristiche fisiche: riflettivitá degli specchi e tolleranze nei raggi di curvatura e nella distanza L fra essi. Da tali simulazioni é risultato fondamentale l'utilizzo di tubi di materiali a coefficiente di espansione molto basso, forati nel mezzo lungo tutta la lunghezza, sui quali fissare gli specchi. Ció garantisce alta precisione nell'assemblaggio e stabilitá della distanza L nel tempo e al variare della temperatura, caratteristiche fondamentali per l'uso prefissato.

Sistema laser e dispositivi per la calibrazione della frequenza sono ora pronti per essere utilizzati insieme. Nei prossimi mesi tale sistema sarà applicato in spettroscopia LIF ultravioletta di molecole di Benzonitrile decelerate. La larghezza attesa delle righe spettrali è di circa 10 MHz. Nel determinare la frequenza di tali righe si dovrà interpolare tra i picchi di interferenza. Essendo la FSR dell'interferometro confocale nota con una precisione di 4 parti su un milione (considerando tre deviazioni standard) è possibile interpolare su più di 100 FSR ottenendo un'accuratezza di $\sim$0.1 MHz. Questo permette di determinare la frequenza delle linee spettrali con una precisione migliore di 1 MHz. Tale valore potrà essere ancora migliorato sfruttando la più stretta FSR dell'interferometro quasi-confocale. Per fare questo, però, è necessario conoscere con maggiore accuratezza, rispetto ad ora, il valore della FSR e ulteriori misurazioni dovranno essere eseguite nell'intervallo già analizzato.

Il valore di 1 MHz della larghezza di riga del sistema laser realizzato e descritto in questa tesi è molto buono ma risulta una caratteristica comune e necessaria nel mondo della spettroscopia UV ad alta risoluzione. Grande innovazione è rappresentata invece dai dispositivi messi a punto per la calibrazione della frequenza, che si distinguono per precisione nel valore della FSR e stabilità in temperatura, risultando molto interessanti e, speriamo, molto utili nello studio sempre più dettagliato e sofisticato delle proprietà molecolari.

Conclusion

In our group a modern technique exploiting the Stark effect a molecule feels in an electric field is applied to decelerate and trap molecular packages from a supersonic jet. Time-varying electric fields ($\geq$100 kV/cm) along the path of the beam decrease the translational kinetic energy of the molecules and with this technique, molecular beams of OH-radicals have been decelerated from 428 m/s to 21 m/s and trapped (about 10^5 molecules in a volume of 0.03 cm^3) [14]. The resolution of a measuring device is limited by the time Δt a molecule spends inside (Heisenberg principle $\Delta t \Delta \nu \geq \pi/2$). Increasing this time by decelerating and trapping molecules, one can increase the obtainable spectral resolution.

In this thesis a laser system generating continuous radiation over the ultraviolet/visible wavelength range with linewidth smaller than 1 MHz and finely tunable frequency, has been setup. The system consists of an Ar^+-ion laser (Coherent Innova Sabre), a ring dye laser (Coherent 899-21), a second harmonic generator (LAS Wave Train) and the calibration devices (two Fabry-Perot interferometers, a cell containing gaseous iodine and a wave-meter). 6.5 W of 514 nm radiation of the Ar^+-ion laser pump the dye solution (Rhodamine 110) inside the ring dye laser. 800 mW of continuous radiation around 550 nm with linewidth smaller than 1 MHz are generated. This wavelength can be tuned over a 50 nm range by changing the length of the optical path inside the cavity. Optical/electronical devices, described in details in section 2, allow for actively stabilization of the frequency. 30 GHz scans of the frequency can be performed at different scan speeds (from 30 GHz/s). The generated laser light is then directed to the second harmonic generator where a non-linear optical crystal inside a ring cavity is used for frequency doubling. 80 mW of continuous ultraviolet light at the wavelength 282 nm are produced and used in the continuous wave (cw) time-of-flight (TOF) measurements of fast and slow OH-radicals described in section 3.3.

Devices for the frequency calibration of the laser system are setup and characterized, i.e. two Fabry-Perot interferometers with concave mirrors and an iodine cell. A small part of the light coupled out of the ring dye laser is directed through them. The absorption spectrum of iodine and the transmission of the two interferometers are measured simultaneously by photodiodes during a wavelength scan. They are used for absolute and relative calibration of the frequency, respectively. From the known frequency of the iodine absorption lines one can estimate a first absolute value for the frequency by off-line comparison with tabulated spectra. A more accurate frequency can be estimated considering the interference peaks of the two interferometers. They generate interference patterns with free spectral ranges 149.9486 $\pm$ 0.0002 MHz (Fabry-Perot confocal interferometer with concave mirrors separated by 500 mm) and 49.543 $\pm$ 0.008 MHz (interferometer with concave mirrors of 100 mm radius of curvature separated by 105.56 mm). These two values, crucial for the frequency calibration of laser scans, are determined with high accuracy in the last part of this work, as described in section 3.1.

A program in *Mathematica* has been written to simulate the interference patterns of the two interferometers, in order to study their quality and stability as a function of their characteristics: reflectivity of the mirrors, tolerances on the radius of curvature and separation distance. From the simulation it turned out that it is of fundamental importance to use tubes of low thermal expansion coefficient materials to hold the mirrors. This guarantees a good long-term and temperature stability of the distance between the mirrors (expected: 25 nm/K) and consequently of the FSR (expected: 7.5 Hz/K, see section 2.2.1).

The laser system and calibration devices are now ready for use. In the next months it will be applied in UV LIF spectroscopy of decelerated Benzonitrile behind an alternate gradient (AG) decelerator. The expected linewidth of the spectral lines is about 10 MHz. In order to determine the frequency of the lines, one has to interpolate between the interference peaks. Knowing the FSR (of the confocal interferometer) with an absolute accuracy of about 4 parts per million (considering three standard deviations), it is possible to interpolate over more than 100 FSR with an accuracy of $\sim$0.1 MHz. This allows to determine the frequency of a 10 MHz linewidth line with higher precision than 1 MHz. This value can hopefully be still improved exploiting the narrower FSR interference pattern of the quasi-confocal interferometer. However the accuracy on this FSR is now too small and has to be increased by performing more calibration measurements.

Other groups involved in high resolution UV LIF spectroscopy of molecules (the Italian group of Professor Becucci at LENS in Florence, for example) use similar laser systems with linewidth around 1 MHz for dynamic and structural studies on aromatic molecules (see http://www.lens.unifi.it).

The accurate frequency calibration and the temperature stability of the FSR of 7.5 Hz/K this system set up, allow for high resolution spectroscopy in the visible/near-UV spectral range on large molecules and offer a significant contribution in the investigation of the molecular properties.

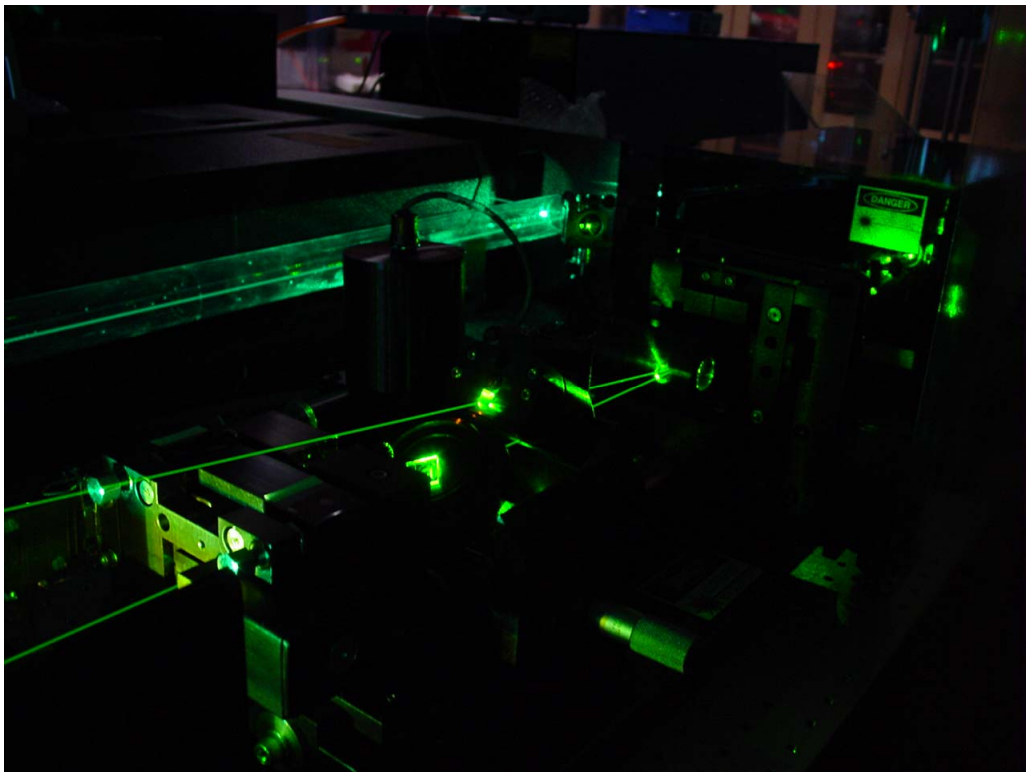
DANGER

.

Figures of page before: laser light in the ring cavity of the ring dye laser while lasing. Red light and green light are produced in these cases using the same dye solution (Rohdamine 6G).

"La natura ha migliaia e migliaia di colori, e noi ci siamo messi in testa di ridurne la scala a una ventina" (Hermann Hesse)

Appendix A

Confocal interferometer FSR measurement data

frequency (cm-1)	q_{int}	q_{frac}
17883.12930	1	0.7
17883.22680	20	20.4
17883.27080	29	29.1
17883.80750	136	136.5
17883.94540	164	164.0
17969.87610	17344	17344.0
17970.16670	17402	17402.0
17970.29270	17428	17427.1
17970.36240	17442	17441.5
17970.41780	17453	17452.5
17970.55970	17481	17480.8
18100.72570	43505	43504.8
18100.88880	43537	43536.8
18101.14330	43589	43588.3
18101.30770	43622	43621.3
18101.47410	43655	43655.0
18115.11050	46381	46381.0
18115.18860	46397	46396.8
18115.27260	46413	46413.6
18115.38080	46435	46435.4
18136.62250	50682	50682.4
18136.70000	50698	50697.8
18136.82950	50724	50723.6
18136.86980	50732	50731.6
18136.95270	50748	50748.2
18137.10320	50778	50778.2
18156.96580	54749	54749.2
18157.16210	54789	54788.4
18157.23260	54803	54802.6

18157.36340	54829	54828.6
18157.44390	54845	54844.3
18165.33590	56423	56422.3
18165.40320	56436	56436.0
18165.49730	56455	56454.5
18165.88850	56533	56532.1
18165.95310	56546	56544.9
18209.13620	65180	65178.9
18209.19760	65193	65191.2
18209.39520	65232	65230.4
18209.51150	65256	65254.1
18209.80990	65315	65313.2
18237.77410	70906	70904.2
18237.81250	70913	70912.1
18237.86770	70924	70922.9
18237.97560	70946	70944.8
18238.03270	70957	70956.0
18238.20870	70993	70991.1
18238.25840	71001	71001.1
18238.42430	71036	71034.6
18238.46580	71044	71042.6
18238.57200	71065	71063.8
18238.60370	71071	71070.0
18238.64150	71079	71077.9
18280.62190	79472	79470.9
18280.98090	79544	79543.2
18281.27220	79603	79602.0
18359.97650	95338	95337.0
18360.09760	95363	95361.0
18360.19180	95382	95380.2
18360.36490	95416	95414.3
18360.43410	95430	95428.5
18360.65910	95475	95473.5
18382.58270	99858	99856.5
18382.64720	99870	99869.3
18382.73700	99889	99887.3
18383.11760	99964	99963.2
18383.17570	99976	99975.1
18383.34310	100010	100008.6
18410.38290	105416	105414.6
18410.49180	105438	105436.5
18410.76430	105492	105490.9
18410.91560	105522	105521.2
18453.84640	114105	114104.2

18453.92440	114121	114120.2
18454.00290	114137	114136.2
18454.04200	114144	114143.5
18454.13610	114163	114162.5
18454.27610	114192	114190.7
18454.38700	114214	114212.7
18454.47850	114232	114230.9

Bibliography

[1] H. L. Bethlem, G. Berden, F. M. H. Crompvoets, R. T. Jongma, A. J. A. van Roij, and G. Meijer. Electrostatic trapping of ammonia molecules. *Nature*, 406:491–494, 2000.

[2] H. L. Bethlem, G. Berden, and G. Meijer. Decelerating neutral dipolar molecules. *Phys. Rev. Lett.*, 83:1558–1561, 1999.

[3] H. L. Bethlem, A. J. A. van Roij, R. T. Jongma, and G. Meijer. Alternate gradient focusing and deceleration of a molecular beam. *Phys. Rev. Lett.*, 88(13):133003, 2002.

[4] Hendrick L. Bethlem and Gerard Meijer. Production and application of translationally cold molecules. *Int. Rev. Phys. Chem.*, 22(1):73–128, 2003.

[5] Gene A. Capelle and H.P. Broida. Lifetimes and quenching cross sections of iodine. *J. Chem. Phys.*, 58:4212–4220, 1973.

[6] V.V.Yashchuk D.Budker, S.M.Rochester. Obtaining frequency markers of variable separation with a spherical mirror Fabry-Perot interferometer. *Rev. Sci. Instrum.*, 71(8):2984, 2000.

[7] Wolfgang Demtröder. *Laser Spectroscopy: Basic Concepts and Instrumentation*. Springer Verlag, Berlin, 2nd edition, 1998.

[8] S. Gerstenkorn and P. Luc. *Atlas du Spectre d'Absorption de la Molecule d'Iode entre*. CNRS, Paris, 1985.

[9] J. R. Johnson. A high resolution scanning confocal interferometer. *Appl. Opt.*, 7(6):1061, 1968.

[10] Hajime Katô et al. *Doppler-free high resolution spectral atlas of iodine molecule 15,000 to 19,000 cm-1*. Japan Society for the Promotion of Science, 2000.

[11] M.G.F. Minnaert. George Darwin Lecture. *Royal Astronomical Society*, 107:274–290, 1947.

[12] J.R. Pierce. *Theory and design of electron beams*. Van Nostrand, Toronto, 2nd edition, 1954.

[13] Anthopy E. Siegman. *Lasers*. University Science Books, Sausalito, CA, USA, 1986.

[14] Sebastiaan Y. T. van de Meerakker, Paul H.M. Smeets, N.Vanhaecke, Rienk T. Jongma, and Gerard Meijer. Deceleration and electrostatic trapping of OH radicals. *arXiv:physics*, page 0407116, 2004.

[15] Jacqueline van Veldhoven, Jochen Küpper, Hendrick L. Bethlem, Boris Sartakov, André J.A. van Roij, and Gerard Meijer. Decelerated molecular beams for high-resolution spectroscopy: The hyperfine structure of $^{15}ND_3$. *Eur. Phys. J. D*, 31(2):337–349, November 2004.

Grazie a

Vorrei ringraziare innanzitutto Jochen per l'energia e l'entusiasmo con cui mi ha seguito in questo lavoro sin dagli albori. I professori Paolo Milani, Salvatore Iannotta, Gerard Meijer per avermi supportato e seguito con disponibilità e professionalità. Kristin, Sophie, Massimo presenze fondamentali in istituto con i quali si è piacevolmente condiviso momenti caffè, sole, notizie del giorno. Le tante persone, a Berlino come a Milano, che mi hanno aiutato nei lavori più noiosi o in quelli più delicati. Grazie infine ai miei genitori che mi hanno dato la possibilità di fare anche questa bellissima esperienza berlinese!